
Experimental Studies on Multivalency

From DNA Origami Model Systems to Living Cells

Ricarda M. L. Berger



München 2020

Experimental Studies on Multivalency

From DNA Origami Model Systems to Living Cells

Dissertation
at the Department of Physics
at the Ludwig–Maximilians–University of Munich

handed in by
Ricarda M. L. Berger
born in Dachau

Munich, May 6, 2020

Experimentelle Studien zu Multivalenz

Von DNA-Origami Modellsystemen zu Lebenden Zellen

Dissertation

an der Fakultät für Physik

der Ludwig-Maximilians-Universität München

vorgelegt von

Ricarda M. L. Berger

geboren in Dachau

München, 06.Mai 2020

Erstgutachter: Prof. Dr. Joachim O. Rädler

Zweitgutachter: Prof. Dr. Ralf Jungmann

Tag der mündlichen Prüfung: 17.06.2020

Zusammenfassung

Als Multivalenz bezeichnet man in der Biochemie das Zusammenspiel mehrerer individueller Bindungsprozesse in einem Ligand-Rezeptor-System. Multivalenz spielt eine fundamentale Rolle in biologischen Erkennungsprozessen, wie zum Beispiel bei der Immunantwort auf Pathogene im menschlichen Körper. Die gleichzeitige Erkennung mehrerer Oberflächenproteine wird auch in der Entwicklung neuer Medikamente, vor allem in der Tumorthherapie mit bispezifischen Antikörpern, angewendet. Trotzdem wirft die Bindungsstärke multivalenter Bindungen noch eine Reihe offener Fragen auf. Die Avidität hängt dabei nicht nur von der Bindungsstärke der einzelnen Liganden ab, sondern auch von der räumlichen Anordnung und Flexibilität. Die DNA Nanotechnologie dient dabei als hervorragende Plattform, um multivalente Bindung mit Nanometer-auflösender Präzision zu charakterisieren und nachzubilden.

In dieser Dissertation entwickelte ich DNA-Origami Konstrukte, die mit sogenannten Fas Liganden (FasL) funktionalisiert waren, um die apoptotische Wirkung der Multivalenz an Zellen untersuchen zu können. Hierzu wurden die FasL in bestimmten Konstellationen sowie in unterschiedlicher Anzahl auf einem monolagigen rechteckigen DNA-Origami angeordnet und anschließend in Kontakt mit menschlichen Gebärmutterhalskrebszellen (HeLa) gebracht. Die Analyse der morphologischen Veränderungen von zehntausenden Zellen mittels Zeitraffermikroskopie ergab, dass der Abstand zwischen zwei FasL ausschlaggebend für das Sterbeverhalten der Zellen ist. Genauer konnte bestimmt werden, dass eine maximale Wirkung bei 10 nm FasL-FasL Abstand generiert wurde. Die den Zellen präsentierte Gesamtanzahl an FasL spielte hingegen eine untergeordnete Rolle. Diese Erkenntnis bekräftigt auch derzeitige Theorien zur Clusterbildung der inneren Domäne des Fas Rezeptors, an welchen der FasL bindet.

Um multivalente Bindungsstärken an lebenden Zellen charakterisieren zu können, wurde eine neue Methode zur Bestimmung von Bindungsaffinitäten basierend auf der Fluoreszenzkorrelationsspektroskopie (FCS) entwickelt. In einer neuen Herangehensweise wurde nicht, wie bei bisherigen Methoden, die Konzentration an gebundenen Liganden, sondern die verbleibenden ungebundenen Liganden bestimmt. Erste Versuche wurden mit

kommerziell erworbenen Antikörpern an menschlichen embryonalen Nierenzellen (HEK) durchgeführt.

Um theoretische Vorhersagen bezüglich multivalenter Bindung zu überprüfen, wurde ein künstliches multivalentes DNA Ligand-Konstrukt untersucht, das an DNA-Origamis als künstliches Rezeptorsystem bindet. Hierzu entwickelte ich eine multivalente Plattform, die ausschließlich auf DNA Hybridisierung beruht und somit definierte Bindungsaffinitäten sowie auch Nanometer-genaue Abstände zwischen Rezeptoren und Liganden ermöglicht. Mithilfe von FCS konnte eine Erhöhung der Bindungsaffinität im Vergleich zu monovalenten Kontrollen aufgrund von Multivalenzeffekten gemessen und theoretische Modelle weiterentwickelt werden.

Abschließend wurde die multivalente Bindung eines weiteren medizinisch relevanten Proteins, dem sogenannten von-Willebrand-Faktors (VWF), charakterisiert, welcher im menschlichen Blut vorkommt. Im Rahmen dieser Arbeit wurde die Interaktion von VWF mit DNA untersucht. Hierbei wurde der Effekt von Ionenstärke und Scherkraft auf die Bindungsaffinität analysiert. Die Anwendung verschiedener biophysikalischer Methoden, wie beispielsweise Thermophorese, Elektrophorese und FCS, erlaubte es einerseits, bestimmte Aminosäuren in einer Domäne des VWF zu identifizieren, welche maßgeblich an der Bindung mit DNA beteiligt sind. Andererseits konnte eine DNA Sequenzunabhängigkeit festgestellt werden. Diese Ergebnisse unterstützen die Annahme, dass VWF an der Eliminierung von Pathogenen durch Bindung an extrazelluläre DNA von neutrophilen Blutzellen beteiligt ist.

Zusammenfassend lässt sich feststellen, dass Multivalenz eine bedeutende Rolle bei biologischen Prozessen spielt. Außerdem konnte gezeigt werden, dass die DNA Nanotechnologie erlaubt, menschliche Zellen kontrolliert zu stimulieren. Sie trägt daher großes Potential für die Grundlagenforschung zur Untersuchung von Wechselwirkungen und Funktionsweisen von Makromolekülen im menschlichen Körper. Dieses Verständnis kann dabei helfen neue wirkungsvolle und intelligente Medikamente zur Bekämpfung beispielsweise von Viren oder Krebszellen zu entwickeln.

Abstract

Multivalency describes the synergy of multiple coupled individual binding processes of two entities, for example surface proteins of a virus with receptors on a host cell. It is fundamental to many different biological processes for instance in the immune response of the human body to foreign pathogens. Also, in the development of new medication multivalency plays a pivotal role including cancer therapy with bispecific antibodies. In recent years, DNA nanotechnology has evolved as an exceptional versatile platform for the characterization of multivalent binding at a nanometer scale.

In this dissertation, I developed a DNA origami tool which allows the study of cell apoptosis induced by so called Fas ligands (FasL). After arranging these ligands in certain patterns with distinct distances on one-layer DNA origami rectangular sheets, they were presented to human cervical cancer cells (HeLa). The analysis of more than ten thousand cells and their morphological responses to the FasL origamis by timelapse microscopy allowed to draw conclusions on their dying behavior. It was found that FasL arranged in a hexagonal pattern with an inter-protein-distance of ten nanometers most efficiently triggered apoptosis. Moreover, unlike expected, I was able to show that the distance between two FasL, rather than their number, was decisive in apoptosis triggering. These results allow conclusions to be drawn on intracellular processes initiated upon FasL binding to cells suggested by current theories.

Further, to determine multivalent binding effects of ligands to living cells, a method for the determination of binding affinities was developed. In our new approach, Fluorescence Correlation Spectroscopy (FCS) served to measure instead of the concentration of bound ligands - as usually done - the number of unbound ligands in solution. Initial experiments were carried out with a commercially available antibody binding to human embryonal kidney cells (HEK).

To evaluate theoretical assumptions for multivalent binding DNA nanotechnology was applied. Therefore, a multivalent DNA origami tool was created which is exclusively based on DNA hybridization. This approach allowed defining exact binding affinities as well as nanometer precise distances between ligand and receptor binding sites. FCS

allowed to characterize multivalency effects according to theoretical predictions.

Finally, a multivalent interaction in the human body was characterized, namely the binding of the blood protein von Willebrand factor (VWF) to DNA. In particular, the effect of ionic strength and shear force on the binding affinity was investigated. Applying various different biophysical methods enabled, on the one hand, to identify distinct aminoacids within a domain of VWF relevant for binding. On the other hand, it was found that the interaction between VWF and DNA was independent of DNA sequence. These findings support the accepted hypothesis that VWF is involved in eliminating foreign pathogens by binding to extracellular DNA of neutrophils.

To summarize, in this dissertation I was able to show that multivalency plays a crucial role in various different biological processes. Additionally, it was demonstrated that cells can be stimulated by an artificial DNA origami nanoagent in a controlled predefined manner. My dissertation provides comprehensive insights in multivalent phenomena which might aid novel, intelligent and versatile drug design in future therapeutic development.

Contents

Zusammenfassung	ix
Abstract	xi
1. Introduction	1
2. Multivalency	7
2.1. Monovalent Binding	8
2.2. Multivalent Binding	9
2.3. Multivalency in Living Organisms	12
2.3.1. Deoxyribonucleic Acid and Nanotechnology	13
2.3.2. Von Willebrand Factor	16
2.3.3. FasL Inducing Apoptosis	17
3. Characterization of Binding Interactions	21
3.1. Fluorescence Correlation Spectroscopy	21
3.2. Microscale Thermophoresis	25
3.3. Electrophoretic Mobility Shift Assay	27
4. Spatial FasL Arrangements Effect Apoptosis Induction	33
4.1. FasL DNA Origami Nanoagent Development	33
4.2. FasL DNA Origami Nanoagent is More Effective Than Single FasL Molecules	36
4.3. FasL Conformation Influences Apoptosis Rate	36
4.4. FasL DNA Origami Nanoagent Potency	38
4.5. Discussion	40
5. FCS as a Method to Study Ligand Interactions on Living Cells	45
5.1. Ligand Depletion Theory	46

5.2. Probe Characterization	47
5.2.1. Alexa 488 Antibody Binds to Cells	47
5.2.2. Diffusional Characteristics	48
5.3. Set-ups for the Separation of Cells from the FCS Measurement Volume	50
5.4. Cell Measurements with FCS	51
5.4.1. Membrane Insert Set-ups	51
5.4.2. Hydrogel Set-up	52
5.5. Discussion	54
6. A DNA Origami Platform to Study Multivalency	57
6.1. Characterization of the Model System	57
6.1.1. Bivalent Ligand	59
6.1.2. Tetravalent Ligand	59
6.2. Characterization of Monovalent vs Bivalent Binding	62
6.3. Discussion	64
7. VWF DNA Binding	71
7.1. Electrostatics Influence A1 Domain DNA Interaction	71
7.2. VWF DNA Binding is Conformation Dependent	73
7.3. Discussion	77
8. Conclusion and Outlook	83
A. Supplementary Information	91
B. Protocols	99
B.1. Proteins and DNA	99
B.2. DNA Origami Preparation	99
B.3. DNA Origami Surface Preparation	100
B.4. Cell Measurements	100
B.5. MST Experiments	101
B.6. FCS Experiments	101
B.7. EMSA Experiments	102
B.8. AFM	102
List of Publications and Manuscripts	103
List of Figures	105

List of Abbreviations	107
Bibliography	111
Acknowledgements	131

1 | Introduction

In December 2019 several people in Wuhan, China, showed symptoms of a novel severe acute respiratory syndrome (SARS). Less than four months later the disease emerged to a worldwide pandemic, forcing governments across the whole planet to shut down public life completely [1–3]. The pathogen infecting millions of people and causing hundreds of thousands of deaths is coronavirus SARS-CoV-2, a β -corona virus infecting cells in the respiratory tract [1, 4]. A virus is an infectious particle requiring a host cell to replicate and spread [5]. In order to enter a host cell and use its machinery to reproduce new virus particles, it needs to bind to the cell surface first (Fig.2.1 A). Generally, multiple unspecific binding events with structures on the cell membrane such as hepara sulfates and other carbohydrate structures aid the first attachment. Later interactions with specific receptors actively pave the way for the entry into the cell [5]. A virus therefore is a well-known example for multivalency [6–8]: The synergy of many weak binding events results in an overall tight binding. Here, the term multivalency originates from chemistry, where valence defines the number of interacting molecules and had been introduced in this terminus already in 1949 by H. Eisen and F. Karush [9]. Another 30 years had passed until first theories on multivalent binding were generally accepted [10, 11]. In this context, the binding strength of one single interaction is referred to as affinity. For a multivalent entity binding with multiple individual units the word avidity has been introduced to describe the overall binding strength. Therefore, a multivalent interaction with many individual affinities is overall defined by the avidity of the whole interaction. Another 20 years passed until G. Whitesides and coauthors published the most recognized review in this field summarizing multivalency in biological systems but also providing a general theory to estimate avidity effects [6]. New model systems and elaborate simulations are still being developed, which will be introduced in the next Chapter 2.

Notably now, apart from tighter binding, it has also been recognized that multivalency influences the selectivity of an interaction [12]: Only if these multiple interactions match - one can imagine a lock-key principle - only then will multiple weak interactions add up to an overall strong interaction. This phenomenon is not only observed for viruses, but

numerous different biological processes such as signaling, communication, information transduction, decision making and reproduction profit from multivalency (s. Chapter 2) [6].

Especially, in the development of novel treatments the specificity accompanying multivalency plays a pivotal role [12]. In particular, antibody-immunotherapy is based on multivalency. Antibodies are naturally produced by our immune system and through their y-shape structure they are able to target pathogens with two binding units simultaneously [13]. Research has adapted these antibodies in order to selectively target tumor cells but spare healthy tissue [12]. This can be achieved by choosing a receptor target which is more abundant on tumor cells than on healthy cells. The antibodies with low individual affinity will only bind tightly to those cells where they can bind simultaneously with both arms resulting in an overall high avidity [14]. If expression levels on normal cells are low, antibodies will only be able to bind with one arm and thereby unbind quickly. In the group of Kiessling et al. they for example successfully employed an antibody to distinguish tumor cells from healthy cells [14]. Additionally, recent improvements generated an even higher selectivity by producing so called bispecific antibodies, which bind to two different tumor markers instead of the same [15]. Only when both receptors are present on a cell a multivalency enhancement is obtainable, because both binding sites will be able to interact with the tumor cell. Consequently, these antibodies benefit from a high specificity towards tumor cells in comparison to healthy tissue and hence less off-target side effects [12].

Even higher specificity and selectivity, however, might be achievable when linking multiple antibodies to an artificial carrier. A promising candidate to create such an artificial carrier is DNA nanotechnology, which convinces with its modularity and adaptability (Chapter 2.3.1) [16, 17]. Using DNA as template material with its intrinsic molecular recognition allows self-assembly of virtually any pre-programmed structure. Additionally, nanometer precise positioning of any desired antibody or protein in basically any required conformation is feasible. This technology, however, has not only gained interest for medication development, but also found its application for the study of all sorts of biological processes and mechanisms such as molecular cell recognition or B-cell activation to name most recent achievements [18, 19].

In terms of this thesis, DNA nanotechnology was used to provide a platform to study multivalency in vitro but also on living cells.

In Chapter 6 I will introduce a multivalency DNA origami model system allowing to probe both selectivity and avidity. Although, multivalency has been extensively studied since more than 20 years, new theories are still evolving challenging old assumptions. As

our DNA model system allows precise definition of receptor and ligand spacing as well as versatile affinity control we aim to probe and adapt existing multivalency theories.

Additionally, DNA nanotechnology was employed to study the multivalency effects on cell death induction (apoptosis). Here, DNA served as a scaffold to spatially arrange ligands associated with apoptosis signaling, so called FasL, with distinct patterns and distances. FasL is a ligand binding to the cell surface receptor FasR, which acts as a molecular switch. Both, apoptosis but also proliferation had been observed upon FasL-FasR interaction [20, 21]. Up to now, it remains an open question, how FasL arrangement effects different signaling pathways. In Chapter 4 results are provided showing that FasL organization in hexagonal arrangements distinctively controls apoptosis triggering. Especially, FasL spacing on the DNA origami substantially changed cell death times, while valency of FasL influenced apoptosis induction less pronounced.

Moreover, DNA on its own is a beautiful example of a multivalent molecule. In Chapter 7 its interaction towards the blood protein VWF will be studied, as it is presumed to aid the pathogen capture in the blood stream [22, 23]. Here, it was found that physical influences such as shear force and electrostatics play a crucial role.

In Chapter 5 the development of a new technique based on FCS will be presented aiming to characterize multivalent binding interactions on living cells. We here employ a new approach of determining the depletion of free ligands in solution to obtain ligand affinities in real-time with low sample consumption.

Finally, in Chapter 8 key results will be summarized and open questions will be discussed with future experimental suggestions. Supplementary results are provided in Appendix A and experimental details can be found in Appendix B.

Fundamental Concepts and Methods

2 | Multivalency

Durchaus studiert, mit heißem Bemühn.
[...]Dass ich erkenne, was die Welt
im Innersten zusammenhält[...]

Johann Wolfgang von Goethe

On a biological scale- what keeps us together? As mammals, we consist of more than a trillion cells, which interact with each other and form the human body [24]. These cellular building blocks are compartments created by small macromolecules such as lipids, carbohydrates, proteins and DNA, which in return consist of molecules and atoms sharing electrons [25]. One can proceed further down this path to reach Quarks and Bosons, but this is not of particular interest for this thesis. Instead, the focus of this chapter is to explain biomolecular interactions, which are reversible and so called non-covalent. These temporary binding events are fundamental in many different aspects of life, where dynamical processes play a role. For signaling, communication, information transduction, decision making and reproduction on the molecular scale, two biological entities have to interact with each other - they need to form reversible bonds. Here, the number (valency) of bonds are crucial in determining the selectivity and strength of an interaction [6]. One single binding event may be weak on its own, but when multiple binding sites form bonds between two macromolecules or cells, a tight binding can be observable [26]. This enhancement effect is often referred to as avidity with multivalency being the underlying mechanism that is studied in this thesis. Therefore, first the theoretical framework for multivalent binding will be presented, followed by examples for multivalent macromolecules. Finally, an introduction to biophysical methods allowing to study binding interactions will be depicted.

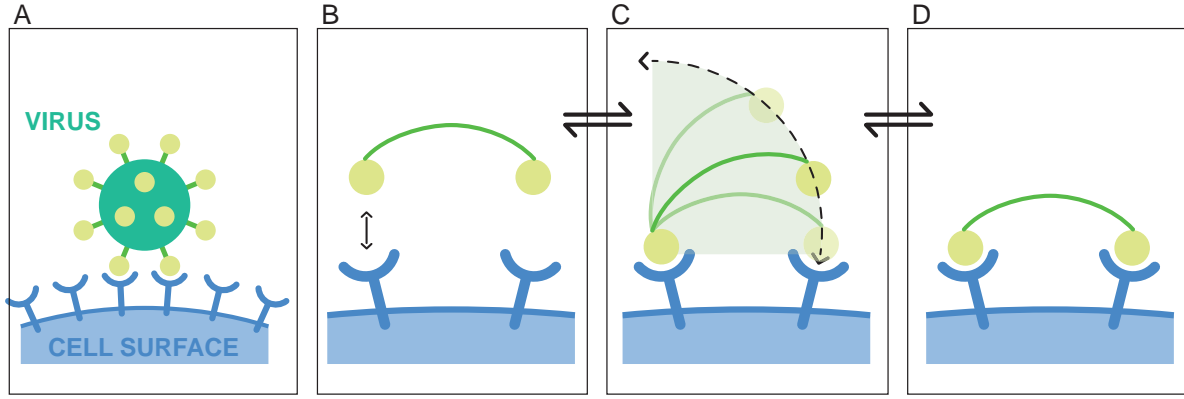


Fig. 2.1.: Schematic illustration of a multivalent interaction. (A) Exemplary representation of a multivalent virus-cell interaction. (B) - (C) Binding process of a bivalent interaction. (B) First, the interaction is initiated with one binding site. (C) Second, scanning of the second binding site within a volume determined by length and flexibility of linker eventually results in both sites binding (D). To unbind, now both binding sites have to detach.

In chemistry, the term *valence* describes the number of binding sites of a molecule. A molecule, protein or cell with *multiple* binding sites is called a multivalent entity or ligand. The interaction between multiple binding sites on two different entities, e.g. two cells, is referred to as a multivalent binding [6, 26–28]. These individual interactions are by definition transient and involve hydrogen bonds, ionic bonds, van der Waals interactions and hydrophobic bonds [29]. To introduce the general theory of binding, first, the one-to-one interaction will be described, followed by different multivalency theories.

2.1 | Monovalent Binding

A non-covalent interaction of two macromolecules forming a complex is described by a forward and a reverse reaction, resulting in a chemical equilibrium



where one macromolecule is referred to as ligand (L) and the other as receptor (R). The change in concentration of the uncomplexed [L] and the complexed form [LR] depends on the on- and off-rate (k_{on} , k_{off}):

$$\frac{d[L]}{dt} = k_{off}[LR] - k_{on}[L][R]. \quad (2.2)$$

This equation is known as the law of mass action. Once the reaction has reached its equilibrium, Eq. 2.2 equals zero and one can define the equilibrium constants for dissociation (K_D [M]) and association (K_A [M^{-1}]):

$$\frac{[LR]}{[L][R]} = \frac{k_{on}}{k_{off}} = K_A = \frac{1}{K_D}. \quad (2.3)$$

In terms of energy, the binding reaction depends on the change in free enthalpy at equilibrium

$$\Delta G^0 = -k_B T \cdot \ln\left(\frac{[LR]}{[L][R]}\right) \quad (2.4)$$

where k_B and T denote the Boltzmann constant and the temperature, respectively. With Eq. 2.3 we can rewrite the formula to:

$$K_D^{-1} = \exp\left(\frac{-\Delta G}{k_B T}\right) = \frac{[LR]}{[L][R]}. \quad (2.5)$$

Experimentally, it is often not possible to determine the free ligand $[L]$ and receptor concentration $[R]$. Instead, parameters which are accessible, are the total ligand $[L_{tot}]$ and receptor concentration $[R_{tot}]$:

$$[L] = [L_{tot}] - [LR] \quad (2.6)$$

and

$$[R] = [R_{tot}] - [LR]. \quad (2.7)$$

Inserting Eq. 2.5 in Eq. 2.7 results in the quadratic solvable equation

$$[R] = [LR] + \frac{[LR]}{K_D([L_{tot}] - [LR])} \quad (2.8)$$

with the solution referred to as the general binding isotherm:

$$y = 0.5(K_D + [R_{tot}] + [L_{tot}] - \sqrt{(K_D + [R_{tot}] + [L_{tot}])^2 - 4[R_{tot}][L_{tot}]})/[R_{tot}] \quad (2.9)$$

2.2 | Multivalent Binding

When facing ligands and receptors consisting of multiple subunits which synergize in binding, this formalism needs to be adapted. In detail, a number (valency) of ligands can be interlinked by a scaffold and allow a simultaneous interaction with multiple receptors

(s. Fig. 2.1). As multiple interactions happen simultaneously, the binding strength of a multivalent ligand towards a target is enhanced, which is often referred to as avidity [6, 26–28]. In the following, an overview of the different models describing the avidity effect introduced by literature will be discussed. Different theoretical models have been proposed to estimate the effect on the total binding strength, when multiple ligand entities can bind at the same time.

The simplest case of multivalency is a bivalent (also called divalent) interaction: One ligand has two binding sites with which it can interact with two receptors on a macromolecule or cell. Throughout literature, the most accepted theory originates from the Jacobson-Stockmayer Model for polycondensations, which has been modified over the years and lead to the general assumption that avidity is based on a concentration enhancement [26, 30–36]. Here, it is hypothesized that once one site of the bivalent ligand has bound to the target, the other binding site is confined to a hemispherical area around the first binding site (s. Fig 2.1 (C)). The radius r of the hemisphere depends on the linker length which is the distance between the binding sites of the ligand. Therefore, the probability that the second binding site binds as well is enhanced if a second receptor is accessible within this hemispherical region. Therefore, the scanning concentration can be described by the following formular [26, 30–33]:

$$[S] = \frac{1}{\frac{2}{3}\pi r^3}. \quad (2.10)$$

The law of mass action (Eq. 2.2) now results in a set of differential equations (App. A.1) accounting for the different sequences of binding events, which in return allow to deduce two main equilibrium constants:

$$K_1 = \frac{k_1}{k_{-1}} = \frac{[lRR]}{[ll][RR]} = \frac{1}{K_{D1}} \quad (2.11)$$

$$K_2 = \frac{\frac{k_2}{f}}{k_{-2}} = \frac{[lRRl]}{[S][lRR]} = \frac{1}{K_{D2}} \quad (2.12)$$

where $[ll]$ and $[RR]$ refer to the total ligand and receptor concentration, respectively. While $[lRR]$ describes the concentrations of ligands bound with one binding site, $[lRRl]$ accounts for the concentrations of ligands bound with both binding sites. Additionally, a penalty factor f is introduced to account for e.g. limited rotational freedom [26]. For the limit $[ll] \ll [RR]$ the fraction bound is defined by:

$$Y = \frac{2[lRR] + [lRRl]}{[RR] + 2[lRR] + [lRRl]} \quad (2.13)$$

By introducing the equilibrium constants from above one obtains

$$Y = \frac{2[l] + \frac{[S][l]}{K_{D2}} + [l]^2 K_{D1}}{K_{D1} + 2[l] + \frac{[S][l]}{K_{D2}} + [l]^2 K_{D1}}. \quad (2.14)$$

In the publications of Diestler et al., Liese et al. and Bandlow et al., a more elaborate model is presented, where the linker between the two binding sites of length r is approximated by a harmonic spring with a flexibility Δr resulting in the effective concentration [34–36]:

$$c_{eff} = \frac{1}{2(2\pi^{3/2})} \frac{\exp(-\frac{1}{2} \frac{(\Delta r - r)^2}{\Delta r^2})}{\Delta r r^2}. \quad (2.15)$$

Here, the bivalent dissociation constant can be estimated by

$$K_{D,bv} = \frac{K_{mono}^2}{\exp(\frac{\Delta G}{k_b T}) 2\pi c_{eff}}, \quad (2.16)$$

with an individual dissociation constant K_{mono} and an energetical term $\exp(\frac{\Delta G}{k_b T})$, accounting for steric hindrance or electrostatic repulsion [36].

For multivalent binding, model systems become more complex and often not analytically solvable. Whitesides et al. suggest a simplistic framework, where they define the relation between K^{mono} and multivalent dissociation K_N^{poly} constant as [6]

$$K_N^{poly} = (K^{mono})^{aN}, \quad (2.17)$$

with N being the number of binding sites and a the magnitude of cooperativity. This relation, however, has been critically discussed in literature [37]. Instead, Kitov et al. have developed an extensive thermodynamic model with the free energy consisting of three main terms [28]:

$$\Delta G_{avidity} = \Delta G_{mono} + \Delta G_{intra} \sum_{i=1}^N w_i (i-1) + RT \sum_{i=1}^N w_i \ln\left(\frac{w_i}{\Omega_i}\right). \quad (2.18)$$

Here, ΔG_{mono} refers to the monovalent complexation and w_i being the probability of an individual i th bound level $w_i = \frac{\exp(-\Delta G_i/RT)}{\sum_{i=1}^N \exp(-\Delta G_i/RT)}$. The last two terms define the

multivalency effect: ΔG_{intra} is the free energy of all subsequent interactions of additional binding sites. The last term is a statistical factor determined by the degeneracy of the whole interaction, where the degeneracy factor Ω depends on the topology of the multivalent interaction (e.g. linear, circular arrangement) and needs to be determined individually for each system [28]. Additional theories try to solve the multivalency effect analytically or numerically, for example the work by Martinez-Verachoechea et al. and Sulzer et al. [27, 38]. Especially, the group of Frenkel emphasize the effect of selectivity concerning multivalent ligands [39]. Therefore, they introduce the term super-selectivity [38, 39], which bases on the fact that the probability for an unbinding event $p_t(unbound)$ scales with the number of individual interactions i with which the multivalent binding is established ($p_i(unbound)$):

$$p_t(unbound) \propto (p_i(unbound))^i \quad (2.19)$$

They hence suggest that the ratio between the probabilities between binding and unbinding similarly to the Hill equation:

$$\frac{p_t(unbound)}{p_t(bound)} \propto \frac{(p_i(unbound))^i}{1 - (p_i(unbound))^i}, \quad (2.20)$$

where the probability for unbinding depends on the individual binding strength, temperature, pH and also the number of possible binding events. All these factors add up to the selectivity of a multivalent interaction [39]. In this dissertation, the aim is to characterize these effects thoroughly to allow a rational design for future multivalent nanoagents.

2.3 | Multivalency in Living Organisms

Having introduced the concept of multivalency in the previous sections, next biological examples will be presented where avidity plays a crucial role. In the insightful review of Whitesides et al. an extensive summary of multivalent interactions in biological systems is given [6]. The range of multivalent binding spans from small molecules to the interaction between large cells. For example, the adhesion of neutrophils to arterial endothelial cells is enabled by the interaction of multiple surface proteins on the cell linking to receptors on the vessel wall [22]. Those neutrophils also play a pivotal role in the capture of pathogens in the blood stream with the aid of the multimeric blood protein von Willebrand factor (VWF), which will be described in Chapter 2.3.2. VWF putatively binds multivalently with the polymeric molecule DNA to immobilize bacteria, which will be presented in

Chapter 7. Moreover, DNA on its own is a multivalent molecule as will be depicted below (Chapter 2.3.1). Additionally, how this multivalency and selectivity can be exploited to create nanometer sized tools will be illustrated next. In fact, in this thesis DNA nanotechnology was used to study, on the one hand, multivalency itself (Chapter 6), but also signaling effects originating from multivalency (Chapter 4). Therefore, the basic knowledge about the so called Fas ligand (FasL) and its multivalent apoptosis induction investigated in this thesis will be presented in Chapter 2.3.3.

2.3.1 | Deoxyribonucleic Acid and Nanotechnology

A well-known macromolecule where multivalency effects play an important role is deoxyribonucleic acid (DNA) - life's genetic information carrier. The history of DNA began with the first remarkable discovery by the Swiss doctor Friedrich Miescher who managed to extract from white blood cells a substance he referred to as *Nuclein* in 1869 [40]. Another researcher who had been honored with the Nobel Prize in 1910 for characterizing the DNA's building blocks was Albrecht Kossel [41]. Almost half a century later the helical structure was correctly proposed by Francis Crick and James Watson with the help of Rosalind Franklin [42]. These and many more findings are the basis of our current understanding of DNA and will be briefly summarized in the following.

The DNA Molecule

Single stranded DNA (ssDNA) is a polymer built from repeating subunits called nucleotides. Each nucleotide consists of the following three building blocks: a sugar (2-deoxyribose), a negatively charged phosphate group and one of the four nucleobases adenine (A), thymine (T), cytosine (C) and guanine (G). The nucleotides are covalently linked to each other via the 5' phosphate and the 3' hydroxyl group of two adjacent pentose sugars forming the DNA's backbone and resulting in its directionality. The DNA sequence (or its information) is defined by the combination of the four bases. Moreover, the interaction between these bases also allow two ssDNAs to form a double stranded (ds) DNA helix via Watson-Crick basepairing (s. Fig. 2.2 (A)). Here, A and T bind with two hydrogen bonds to each other and C and G with three. When the sequences of two ssDNAs match, meaning they are complementary to each other, all hydrogen bonds of each base pair collectively link the two ssDNAs in a multivalent manner. The resulting energies for each basepairing event as well as its effect on the nearest neighbor bases was introduced by SantaLucia et al. and forms the basis of sequence dependent DNA hybridization prediction tools such as Mfold [43–45]. The total energy ΔG of the basepair

formation can be estimated by

$$\Delta G = \sum_{i=1} n_i \Delta G(i) + \Delta G(tGC) + \Delta G(tAC) + \Delta G(s). \quad (2.21)$$

Here, $\Delta G(i)$ refers to the changes in free energy for possible Watson-Crick nearest neighbor (NN) interactions determined in various hybridization studies. n_i accounts for the occurrence of each NN. $\Delta G(tGC)$ and $\Delta G(tAC)$ represents the effect of the terminal bases GC and AC, respectively. $\Delta G(s)$ describes an additional entropic penalty for self-complementarity [43]. Online prediction tools have adapted this model and allow to determine for any given sequence the free energy corrected for temperature as well as a range of salt conditions [45].

To describe the hybridization kinetics, a slightly modified version nicely summarized by Cantor and Schimmel will be presented [46]. Assuming two complementary ssDNA strands equally mixed at time $t=0$ allows to write the change in ssDNA concentration over time as follows:

$$\frac{dC_s}{dt} = -k_{on} C_s(t)^2 \quad (2.22)$$

with C_s being the concentration of ssDNA at the given time and k_{on} the hybridization rate. This equation can be solved by integration which results in:

$$C_s(t) = C_s(0) \frac{1}{k_{on} t C_s(0) + 1} \quad (2.23)$$

The hybridized fraction can therefore be formulated as:

$$f_h(t) = 1 - \frac{C_s(0)}{C_s(t)} = 1 - \frac{1}{k_{on} t C_s(0) + 1} \quad (2.24)$$

Later on this equation will be used in a slightly modified version accounting also for a fluorescently unlabeled f_u and labelled fraction f_l :

$$f_h(t) = 1 - f_u - f_l = 1 - f_u - \frac{1}{k_{on} t C_s(0) + 1} \quad (2.25)$$

While dsDNA is found to be stiff with a persistence length depending on the buffer conditions of roughly 100 bp, allowing to estimate the end to end distance by [47–50]:

$$l(dsDNA) = N \cdot a \quad (2.26)$$

with N referring to the number of bases and a to the distance between two bases

($a = 0.34\text{nm}$). For ssDNA, persistence lengths in the range of 0.7 nm to 6 nm have been reported in literature and additionally, it has been found that the buffer condition as well as sequence have an immense effect on the end-to-end distance [51–54]. Hence, many different models have been introduced to describe the shape of ssDNA such as the Freely Jointed Chain (FJC) model [55]. As a rough estimate of the end-to-end distance a random walk can be assumed:

$$\langle d^2 \rangle = N \cdot a^2 \quad (2.27)$$

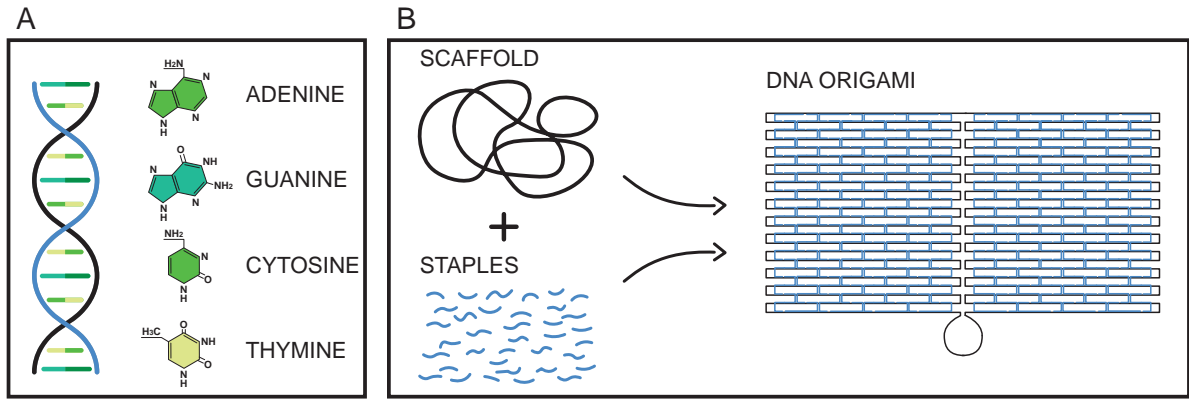


Fig. 2.2.: Schematic illustration of DNA and DNA origami. (A) dsDNA schematically represented with the four bases Adenine, Guanine, Cytosine and Thymine. (B) Schematic illustration of DNA origami folding from a long ssDNA scaffold strand with short ssDNA staple strands.

DNA Origami Nanotechnology

Already in the 1980s Nadrian C. Seeman saw the potential to build nanometer sized objects from DNA [56]. However, another 20 years needed to pass for Paul Rothemund to pave the way towards a new research area: DNA origami nanotechnology [57]. Here, the selectivity of DNA basepairing allows to fold long ssDNA (typically the genome of the M13mp18 bacteria phage) called *scaffold* with the aid of short synthesized oligonucleotides (*staples*). These staples hybridize during a thermal annealing process to *a priori* defined locations on the scaffold and enable the self-assembly of any desired two or three dimensional object (s. Fig. 2.2 (B)). The structure utilized in this thesis is a one-layer rectangle with roughly the dimension of 70 nm × 100 nm. To address certain positions on the DNA origami, staples are designed to protrude vertically from the structure or are functionalized with any desired molecule such as Biotin to name one. This design can be implemented, for example, with the freeware caDNAno, or the Picasso software specialized for the

rectangular structure [58, 59]. Through its adaptivity and precision, DNA origami nanotechnology has evolved as a well-established technique for the study of processes on the nanometer scale and raised the interest to apply it in future nanomedicine [16]. Recent work by Fangfei et al., for example, has provided evidence that cells could be sorted by tetrahedral DNA frameworks decorated with multiple stoichiometrically arranged ligands [18]. Older work by Hariadi et al. allowed to examine collective myosin movement on a DNA origami sheet and in the group of Liedl they tested DNA origami objects as possible immuno-stimulators [60–62]. Additional outstanding work was provided by Douglas et al. who created a DNA nanorobot designed as a locker equipped with an aptamer-gated opening-mechanism allowing to carry molecular payloads inside to deliver to cells [63].

2.3.2 | Von Willebrand Factor

In the bloodstream we come across another multivalent molecule, namely the mechanosensitive von Willebrand Factor (VWF), which will be characterized in this thesis (Chapter 7). VWF is well-known for its role in primary hemostasis, the first step in wound healing. When blood vessels are ruptured high shear forces resulting from increased blood flow stretch VWF from a globular to an elongated conformation and thereby expose binding sites to many different kinds of molecules and cells (e.g. collagen or platelets) [64, 65]. Consequently, the formation of aggregates for wound stilling is enabled. But, numerous other processes are also linked to VWF such as cell proliferation, angiogenesis and inflammation [66]. During inflammation for example VWF is released to the bloodstream [66]. At the same time neutrophils, a type of white blood cells, are activated and relieve their inner structures, such as DNA, to form so called neutrophil extracellular traps (NETs). These NETs are large meshes which immobilize pathogens and their virulence factors [21]. Herein, VWF was suggested to interact with these NETs to stabilize and at the same time aid the attachment to blood vessel walls [67]. The molecular mechanism behind the VWF NET interaction is not yet fully understood. However, it is assumed that VWF simultaneously binds to collagen on endothelial cells and to DNA in the NETs [23]. In order to unravel the interaction mechanism one has to understand the molecular structure of VWF. In detail, VWF is a multimeric protein with sizes up to 40 000 kDa, where the 500 kDa Dimers form the repeating unit linked to each other via interchain N terminal disulfide bonds [69]. Electron microscopy and crystallography paired with bioinformatic sequence analysis has provided the general accepted multiple domain structure as shown in Figure 2.3.2. Here, the A and D domains consist of globules of 4-7 nm, where different domains have been identified to interact with multiple ligands

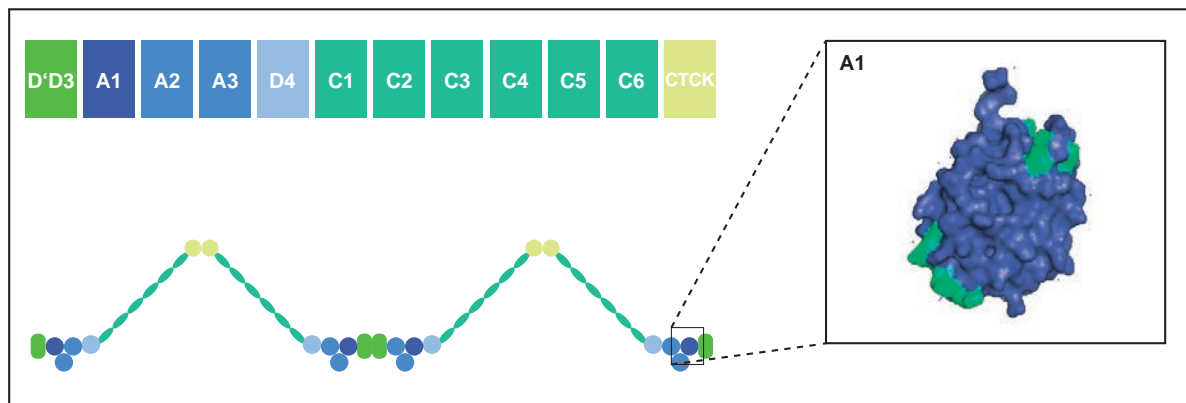


Fig. 2.3.: Multidomain VWF structure with A1 domain. Multiple domains of VWF monomer represented as colored rectangles and multimeric structure (four monomers) depicted below. Inset: Structure of A1 domain with positively charged Arginines illustrated in green adapted from PDB data published by Emsley et al. [68].

and cell receptors [70]. Interestingly, many of the binding regions are hidden when VWF is present in its inactivated globular shape. However, high flow rates above 1000 s^{-1} cause VWF to elongate and relieve the binding sites [71]. For the fully stretched VWF monomer sizes between 60 nm and 85 nm have been reported in literature [70, 72, 73]. Especially, the A1 domain has been identified to bind multiple proteins such as the platelet glycoprotein *GpIb* α , cell surface sulfatides, subendothelial heparans and Collagen VI, but only when the VWF is in its open conformation [68]. The A1 domain itself has a size of $4\text{ nm} \times 4\text{ nm} \times 3\text{ nm}$ and the distance between two A1 domains from different monomers have been proposed to be roughly 20 nm [68, 72]. As the A1 domain contains multiple charged arginines (highlighted in green in Fig. 2.3 Inset) electrostatic attractions have been suggested to play a role in binding with for example the *GpIb* α [74–76]. Also, Grassle et al. provided evidence that the interaction of the VWF-A1 domain with DNA is electrostatically driven [23]. They observed binding of VWF to DNA when Ristocetin, an antibiotic which is believed to relief the A1 domain binding site, was added. But, when shielding the negative charge on DNA with polycationic chitosan, binding was prevented [23]. Up to now, however, the mechanism of DNA binding to VWF remains unknown and will be discussed in Chapter 7.

2.3.3 | FasL Inducing Apoptosis

Fas Ligand (FasL) is a molecule where multivalency plays a role in signal transduction of living cells. FasL binds to the transmembrane receptor FasR, also known as cluster

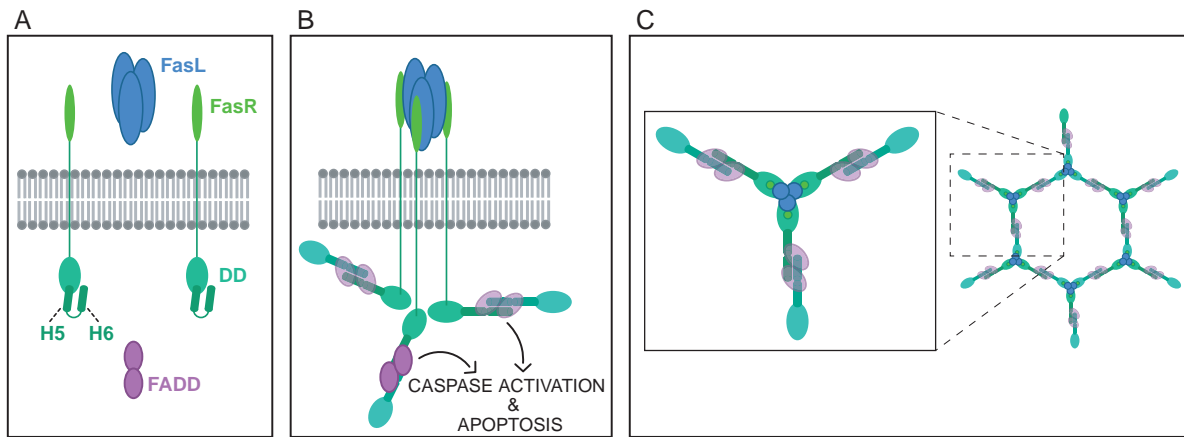


Fig. 2.4.: Schematic illustration FasL-FasR interaction. (A) Unbound state: FasR is in an inactive conformation. (B) Bound state: dimerization of the death domain (DD) and subsequently the interaction with Fas-associated death domain result in caspase activation and apoptosis induction. (C) Hexameric illustration of FasL induced FasR clustering. Adapted from [79, 80].

of differentiation 95 (CD95) or apoptosis antigen 1 (APO-1) (s. Fig. 2.4). Both macromolecules are categorized in the tumor necrosis factor (TNF) superfamily and play a pivotal role in cell proliferation, invasion or death [77–79]. FasL is in terms of this thesis interesting due to the fact that a single soluble FasL trimer binding to FasR does not efficiently induce any signaling cascades inside the cell [81]. However, when multiple linked entities of FasL bind simultaneously they can trigger apoptosis, a form of programmed cell death. Holler et al., for example, compared a hexameric FasL fusion antibody to FasL trimer and demonstrated that only the hexameric version was highly cytotoxic [82]. Also, the research by Zhang et al. provides evidence that a multivalent interaction of FasL is required to induce cell apoptosis. Here, they constructed a DNA tetrahedron functionalized with up to six Fas peptides and determined an enhancement of apoptosis when the tetrahedrons were equipped with a minimum of three Fas peptides [83]. A study investigating the effect of FasL spacing on apoptosis induction was done in the group of Monzel [20]. By functionalizing FasL to a supported lipid bilayer, they could control inter-ligand distances by varying the functionalization densities. Thereby, they determined an optimal average FasL distance of 9-11 nm for efficient apoptosis [20]. These distances in fact, are hypothesized to result from intracellular processes induced upon FasL binding to FasR. It is suggested that FasL switches FasR from an inactive state to an active conformation [79, 80, 84–87]. In more detail, FasR consists of three domains: an extracellular domain where FasL predominantly binds to two of the three cysteine rich domains (CRD), a transmembrane domain and an intracellular domain that is essential

for signal transduction inside the cell. The intracellular domain includes a 80 aminoacid domain named the death domain (DD). This domain contains two helical structures (helix 5 and helix 6) which are believed to facilitate DD dimerization only when FasL is bound. In return, this dimerization allows interaction with the Fas-associated death domain (FADD), which leads to caspase 8-dependent apoptosis (s. Fig. 2.4) [79, 80, 84, 85]. However, up to now, this multivalent phenomenon has not been studied in a defined and controlled manner. Therefore, in Chapter 4 I will introduce a DNA origami tool to investigate spatial and conformational effects on apoptosis induction mediated by FasL.

3 | Characterization of Binding Interactions

To study binding interactions many different methods have been developed over the years. In the following, three techniques will be briefly introduced which have been applied in this thesis. First, Fluorescence Correlation Spectroscopy (FCS) will be depicted as it is a well accepted method to study binding processes in solution. Next, the principles of Microscale Thermophoresis will be outlined. Also with this method, interactions of soluble binding partners are investigated. Compared to conventional FCS it has the benefit that not only diffusional effects upon binding change the thermophoresis signal but also conformational changes or changes in charge and hydration shell can be investigated. Last but not least, the Electrophoretic Shift Assay will be delineated. It has a broad acceptance especially in biochemistry research and convinces with its simplicity and vividness. Each of these techniques rely on fluorescence - the release of electromagnetic radiation of a molecule or protein when returning from an excited state back to the ground state.

3.1 | Fluorescence Correlation Spectroscopy

In the single-molecule technique Fluorescence Correlation Spectroscopy (FCS) intensity fluctuations $F(t)$ resulting from fluorescently labelled molecules diffusing through a sub-femto liter excitation volume are correlated. The intensity of these fluctuations reveals information about the concentration of fluorescent molecules, while the frequency of fluctuations uncovers the size of fluorescent particles. Therefore, FCS allows to study binding processes which result in a change in diffusivity of the fluorescent particle [88–90]. The typical FCS set-up consists of a confocal microscope, where the laser light is guided through a dichroic mirror towards a high numerical aperture objective ($NA > 0.9$) creating a small focus excitation volume in the sample. The fluorescence signal of particles diffusing through this volume is again collected with the objective. Due to its larger wavelength

compared to the excitation light, the fluorescence signal is directed with a dichroic mirror towards fluorescent filters and a pinhole which selects for the z focal plane of the observation volume. Next, the signal is passed onto an avalanche photodiode (APD) and a hardware correlator correlates the signal fluctuations to receive the autocorrelation curves $G(\tau)$. Via fitting, the diffusion time τ_D , triplet time τ_T and sample concentration c can be determined [91, 92]. For the study of binding interactions especially τ_D is relevant, as it becomes larger for complexed molecules. A brief overview of the theoretical concept will be presented below, for a more detailed description of the technique the reader is referred to literature [93, 94].

The normalized autocorrelation is defined by the temporal correlation of the fluorescence intensity at time t and after a delay time τ :

$$\tilde{G}(t) = \frac{\langle F(t+\tau)F(t) \rangle}{\langle F(t) \rangle^2} = 1 + \frac{\langle \delta F(t+\tau)\delta F(t) \rangle}{\langle F(t) \rangle^2} = 1 + G(\tau), \quad (3.1)$$

where $\delta F(t) = F(t) - \langle F(t) \rangle$ describe the intensity fluctuations. In return, these fluctuations depend on the following characteristics [92]:

1. illumination intensity profile $I(\mathbf{r})$
2. detection probability defined by the optical components $\Psi(\mathbf{r})$
3. spatial fluorescent particle distribution $c(\mathbf{r}, t)$
4. brightness $B = \kappa\epsilon q$ resulting from the average photon counts from a single fluorophore which is defined by the detector efficiency κ , the extinction coefficient ϵ and the quantum efficiency q of the fluorophore

These characteristics are summarized in the formula

$$F(t) = B \int I(\mathbf{r})\Psi(\mathbf{r})c(\mathbf{r}, t)d\mathbf{r}. \quad (3.2)$$

The fluorescence detection profile is defined as $\Omega(\mathbf{r}) = I(\mathbf{r})\Psi(\mathbf{r})$ which can be approximated by a three-dimensional Gaussian distribution:

$$\Omega(\mathbf{r}) = \Omega_0 \exp(-2\frac{x^2 + y^2}{\omega_0^2}) \exp(-2\frac{z^2}{z_0^2}) \quad (3.3)$$

with ω_0 being the radius perpendicular to the beam (x, y) and z_0 the radius in z -direction. The structure parameter

$$S = \frac{z_0}{\omega_0} \quad (3.4)$$

therefore, describes the ratio of radial and axial expansion of the detection volume. For simplifications in the following only $G(\tau)$ will be used instead of $\tilde{G}(t)$. Taken together, we obtain

$$G(\tau) = \frac{B^2 \int \int \Omega(\mathbf{r}) \langle \delta c(\mathbf{r}, t) \delta c(\mathbf{r}', t + \tau) \rangle \Omega(\mathbf{r}') d\mathbf{r} d\mathbf{r}'}{(B \langle c \rangle \int \Omega(\mathbf{r}) d\mathbf{r})^2}, \quad (3.5)$$

where now the intensity fluctuations are interpretable as concentration fluctuations $\langle \delta c(\mathbf{r}, t) \delta c(\mathbf{r}', t + \tau) \rangle$ due to Brownian motion, which can be described by the diffusion coefficient D as

$$\langle \delta c(\mathbf{r}, t) \delta c(\mathbf{r}', t + \tau) \rangle = \langle c \rangle (4\pi D \tau)^{3/2} \exp\left(-\frac{|\mathbf{r} - \mathbf{r}'|}{4D\tau}\right). \quad (3.6)$$

When Eq. 3.4, Eq. 3.3 and Eq. 3.6 are inserted into Eq. 3.5 one obtains

$$G(\tau) = G(0) \left(1 + \frac{\tau}{\tau_D}\right)^{-1} \left(1 + \frac{\tau}{S^2 \tau_D}\right), \quad (3.7)$$

where the translational diffusion time $\tau_D = \frac{\omega_0^2}{4D}$ corresponds to the average duration time of a fluorophore within the detection volume. The amplitude at $\tau = 0$ represents the average number of fluorescent particles within the detection volume according to Poissonian statistics:

$$G(0) = \frac{\langle \delta F(t) \delta F(t) \rangle}{\langle F(t) \rangle^2} = \frac{\langle \delta N \delta N \rangle}{\langle N \rangle^2} = \frac{1}{\langle N \rangle}. \quad (3.8)$$

Hence, the variance of fluctuations allows to draw conclusions on the concentration within the sample. One, therefore, obtains the autocorrelation curve for freely diffusing particles:

$$G_D(t) = \frac{1}{N \left(1 + \frac{\tau}{\tau_D}\right) \sqrt{1 + \frac{\tau}{\omega^2 \tau_D}}}. \quad (3.9)$$

Consequently, fitting this relation provides information about the particle diffusivity. The Einstein-Smoluchowski equation relates the diffusion coefficient D to the drag coefficient γ in a low Reynolds number medium [95, 96]:

$$D = \frac{k_B \cdot T}{\gamma} \quad (3.10)$$

with k_B the Boltzmann's constant and T the absolute temperature.

Accordingly, one can draw conclusion on the particle shape. For a spherical particle of

radius r in a medium with the viscosity η , γ is described by the Stokes' law as [97]:

$$\gamma = 6\pi \cdot \eta \cdot r. \quad (3.11)$$

A disk-shaped object of radius R is represented by the following relation [98]:

$$\gamma = 12\pi \cdot \eta \cdot R. \quad (3.12)$$

The drag coefficient for a rod-shaped object can be estimated by [99]:

$$\gamma = \frac{3\pi \cdot \eta \cdot L}{\ln(L/d) + 0.312 + 0.565 \cdot d/L - 0.100 \cdot (d/L)^2}, \quad (3.13)$$

where L denotes the length of the rod and d the diameter.

However, not only diffusion influences the autocorrelation curve. There are also other physical phenomena affecting the intensity fluctuations e.g. triplet kinetics [100]. Therefore, depending on the fluorophore Eq. 3.9 has to be modified to account for these kinetics. The triplet contribution arises from the fact that fluorescent molecules in the excited state not necessarily relax into the ground state, but instead decay to the triplet state. Here, the relaxation to the ground state is quantummechanically forbidden and therefore longer excitation lifetimes are observable in the range from 0.5 to 10 μs , which are detectable as dark-times in FCS. Hence, the autocorrelation curve can be modified with a triplet term, describing the probability of a fluorophore entering the triplet state, which base on optical Bloch equations [101]:

$$G_T(\tau) = (1 + \frac{T}{1-T}) \exp(-\frac{\tau}{\tau_T}), \quad (3.14)$$

where τ_T corresponds to the triplet relaxation time and T the fractional population of the triplet state.

In this thesis, FCS was applied to study binding reactions, where multiple species contribute to the signal. Hence, the autocorrelation curve must be appended with additional diffusion terms:

$$G(\tau) = N^{-1} \sum_{i=1}^m x_i (1 + \frac{\tau}{\tau_{Di}})^{-1} (1 + \frac{\tau}{\omega^2 \tau_{Di}})^{-1/2}. \quad (3.15)$$

Here, m denotes the total number of different particles and x_i the fraction of particles with a diffusion time τ_{Di} . Most commonly, the two component fit was applied which

simplifies to:

$$G(\tau) = N^{-1} \left[\left(1 + \frac{\tau}{\tau_{D1}}\right)^{-1} \left(1 + \frac{\tau}{\omega^2 \tau_{D1}}\right)^{-1/2} + (1-x) \left(1 + \frac{\tau}{\tau_{D2}}\right)^{-1} \left(1 + \frac{\tau}{\omega^2 \tau_{D2}}\right)^{-1/2} \right] \quad (3.16)$$

Typical FCS autocorrelation curves are shown in Figure 3.1 (A). When the diffusion time increases upon binding, K_D values are obtainable with FCS in titration experiments. Therefore, the unlabeled species needs to be two orders of magnitude larger than the labelled species to get well resolvable fits for conventional FCS. One possibility to avoid this major drawback is the Two-Color-FCS approach where both species are labelled with different fluorophores [92]. For most systems characterized in this dissertation, the diffusional changes upon binding were well distinguishable with conventional FCS. Only the interaction between the A1 domain and DNA was not measureable with conventional FCS. To study this interaction Microscale Thermophoresis was applied, which will be explained in the following Chapter.

3.2 | Microscale Thermophoresis

Another powerful tool to study binding interactions is Microscale Thermophoresis (MST). In MST, the directed movement of fluorescent molecules influenced by a temperature gradient, which is called thermophoresis, is investigated. The main benefit of MST for quantifying binding interactions is, that thermophoresis is not only affected by size changes, but also changes in charge, hydration shell and conformation. Already in 1856, the phenomenon of thermophoresis was first described by Carl Ludwig [102]. Spatial inhomogeneous temperatures result in transport of heat energy. A mixture of particles within a liquid exposed to a temperature gradient responds with concentration diffusion fluxes, also referred to as Soret effect [103]. Local concentration differences result in diffusion of particles along the gradient (Ficks's law) [104]. The total mass flux \mathbf{j} is described by

$$\mathbf{j} = \mathbf{j}_D + \mathbf{j}_T = -\nabla_c D - c \nabla T D_T \quad (3.17)$$

with c referring to the concentration and D to the diffusive mobility and D_T the thermophoretic mobility defining the velocity in a temperature gradient $v = D_T \nabla T$. In steady state the net flux $\mathbf{j} = 0$ and one obtains a differential equation:

$$\frac{dc}{c} = -\frac{D_T}{D} dt \quad (3.18)$$

with the solution:

$$\frac{c(x)}{c_0} = \exp\left(-\frac{D_T}{D}(T(x) - T(x_0))\right) = \exp(-S_T \Delta T) \quad (3.19)$$

with c_0 characterizing the local concentration at position x_0 . For small concentration changes ∂c the Soret coefficient describing the magnitude of thermodiffusion in steady state can be defined as $S_T = \frac{\partial G}{\partial T}$ with the Gibbs-free energy $dG = -SdT + Vdp + \mu dN$ [105]. At constant pressure and for a closed system the Soret coefficient is therefore proportional to the entropy $S_T = S/k_B T$. The two main contributions affecting the Soret coefficient in aqueous solutions are an ionic and a hydration contribution:

$$S_T = \frac{A}{k_B T} \left(-s_H + \frac{\beta \sigma_{eff}^2 \kappa}{4\epsilon\epsilon_0 k_B T^2} \right), \quad (3.20)$$

given by the hydration entropy $s_H = S_H/A$ per molecule surface A with an effective surface charge σ_{eff} , the Debye screening length κ , the vacuum permittivity ϵ_0 , the dielectric constant for water ϵ and the temperature dependent solvent dielectric constant $\beta = 1 - (T\epsilon)\partial\epsilon/\partial T$ [105]. To induce a temperature gradient a MST instrument is equipped with an infrared laser locally heating up a small capillary containing a fluorescently labelled sample (ca. 5 μl). To read out the local sample concentration a second laser excites the fluorescent particles at the same spot and the fluorescent intensity is determined with (F_{hot}) and without (F_{cold}) heating [106]. The difference in fluorescent intensity can be calculated as:

$$\Delta F = \frac{F_{hot}}{F_{cold}} = \frac{c_{hot}}{c_{cold}} = \exp(-S_T \Delta T). \quad (3.21)$$

To summarize, the Soret coefficient is determined by the particle size, its charge, the buffer conditions and the hydration entropy of the particle. If one of these parameters is affected in a binding interaction, it will influence the local concentrations upon a local temperature change. By varying the concentration of the unlabeled binding partner in a titration series, ΔF will be proportional to the fraction of bound species and by fitting with Eq. 2.9, K_D values are obtainable [107] (s. Fig. 3.1 (B)). In comparison to conventional FCS, a large size difference of the two binding partners is not required for MST, as it is not only effected by diffusional changes. But, this sensitivity comes at the cost of a high impact of the type of fluorophore and the buffer condition. Moreover, MST is an ensemble measurement, while FCS is a single molecule technique. For both techniques, studies with polydisperse samples, e.g. multimeric proteins, are intricate. The next method described, provides a solution for these samples.

3.3 | Electrophoretic Mobility Shift Assay

An electrophoretic mobility shift assay (EMSA), also called mobility shift electrophoresis, is commonly used for protein-DNA binding measurements. Generally, in electrophoresis charged particles move through a gel matrix e.g. a polyacrylamide or agarose gel by applying a constant voltage to the surrounding buffer [108]. Assuming a particle with the charge q and mass m in an electric field \mathbf{E} , two forces describe the motion of the particle: the electric force $\mathbf{K}_{el} = q\mathbf{E}$ and a frictional force $\mathbf{R} = -\gamma\mathbf{v}$ depending of the velocity \mathbf{v} and the drag coefficient γ . Consequently, the Newtonian equation of motion relates these forces to velocity by $\mathbf{K}_{el} - \gamma\mathbf{v} = m\frac{d\mathbf{v}}{dt}$, which results in the following differential equation where vectors have been substituted with scalars:

$$\frac{dv}{dt} + \frac{\gamma}{m}v = \frac{K_{el}}{m} \quad (3.22)$$

The velocity of a particle moving in a constant electrical field is thereby described by:

$$v(t) = \frac{K_{el}}{\gamma}(1 - \exp(-\gamma t/m)) \quad (3.23)$$

which eventually reaches a constant velocity of

$$v(t) = q \frac{E}{\gamma} \quad (3.24)$$

As stated above the drag coefficient is determined by the size of the particle and viscosity of the medium (s. Eq. 3.11, Eq. 3.12 and Eq. 3.13). So far, only the size of the particle has been considered. However, there are also other effects influencing the velocity of the particle such as the ion cloud forming around the charged particle. Additionally, details of the gel matrix need to be considered when determining the friction force. For DNA, for example, so called reptation models have been introduced aiming to describe the migration through a gel matrix when an electrical field is applied. Lumpkin et al. propose a theory where the motion of DNA follows along a so called *reptation tube* created by the surrounding gel pores [109]. The mobility μ is described by the charge q of DNA, γ the drag coefficient of a chain within the tube with length L and h_x the end-to-end distance of the chain along the field direction (x):

$$\mu = \frac{q}{\gamma} \times \frac{\langle h_x^2 \rangle}{L^2} \quad (3.25)$$

Since the exact mobility of the particle, however, is not relevant for the analysis of EMSAs the reader is referred to literature for detailed information [109–111].

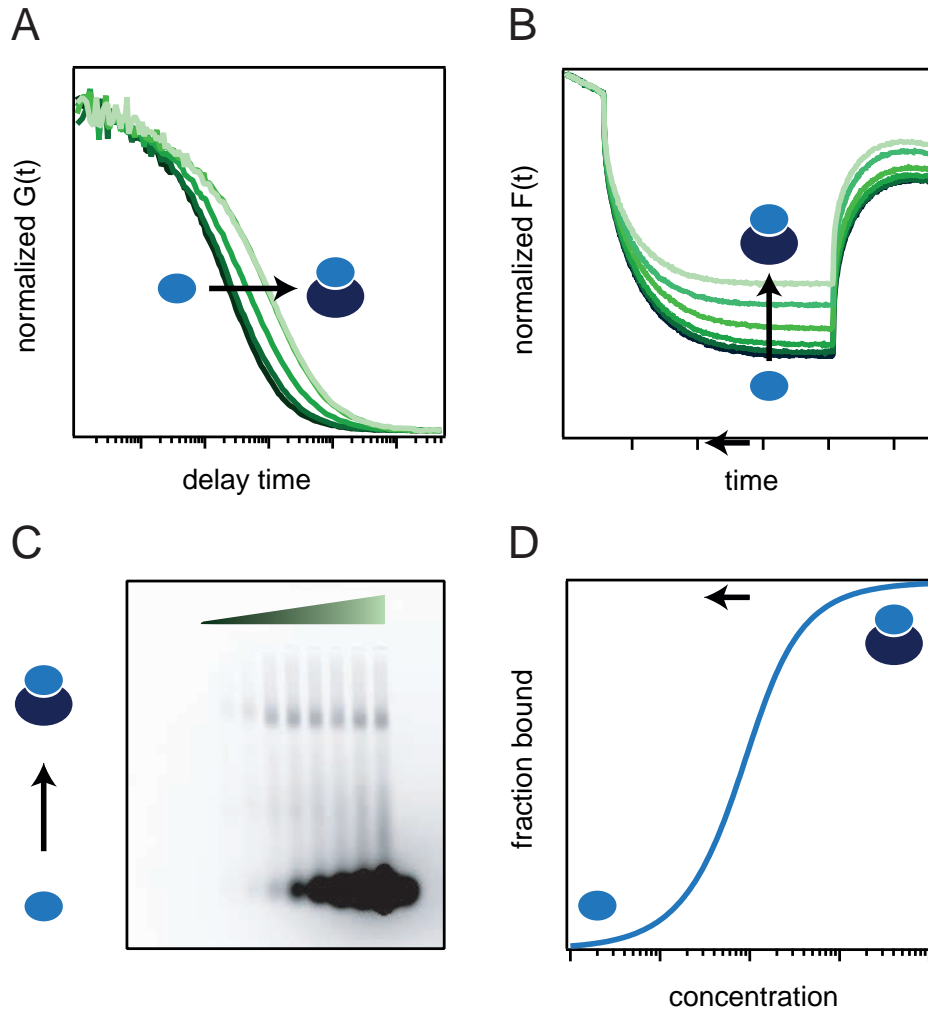


Fig. 3.1.: Overview of Binding Methods. (A) Typical FCS autocorrelation curves. Upon binding, curves shift right due to an increase in size and hence in diffusion time. (B) Typical MST curves. Usually, the higher the bound fraction, the higher the fluorescence plateau due to change in thermophoretic movement. (C) Typical EMSA gel image. Bound complex migrates due to e.g. larger size slower through the gel matrix. (D) Typical fraction bound curve as a function of binding partner concentration.

To summarize, the velocity of particles migrating through the gel depends on their size, charge, shape as well as on the applied voltage and the mesh size of the polyacrylamide or agarose gel. Therefore, the principle concept of investigating binding reactions by using EMSA is based on the fact that bound complexes face changes in their size and charge and consequently migrate differently through the gel matrix compared to the

uncomplexed DNA/protein. These differences are later visible as separate bands in the gel as shown in Figure 3.1 (C). Hence, analyzing the number of particles in these separate bands allows to determine the bound fraction and with Eq. 2.9 the K_D of the interaction. For example, the number of particles is proportional to the fluorescence signal if particles are fluorescently labelled or stained with intercalating dyes in case of DNA. The strength of EMSA is its ability to study a large range of protein/DNA sizes as well as its possibility to investigate not only purified but also unpurified samples [108]. Also, stoichiometric effects are easily observable as multiple bands in the gel. However, a limiting factor for the determination of binding constants is that an EMSA is not conducted at thermodynamic equilibrium. In more detail, once migrating within the gel matrix unbound and complexed forms get separated and thereby unbinding processes might be favored. But, it is assumed that a so called *caging effect* stabilizes complexes. Yet, obtained K_D values have to be interpreted with caution, especially for weak binding interactions with fast off-rates [108, 112].

Experimental Studies

4 | Spatial FasL Arrangements Effect Apoptosis Induction

As mentioned in Chapter 2.3.3 FasL is a ligand of the tumor necrosis factor (TNF) superfamily, which plays a crucial role in both cell proliferation and apoptosis [77–79]. It has been reported by Peter et al. that e.g. immune cells eliminate cancer cells by FasL induced apoptosis [84]. Nevertheless, it has been observed that single FasL molecules are not capable of efficient apoptosis induction. Rather a minimum of two FasL entities were claimed to be required in potent cell killing [81]. Along with these studies, it was suggested that upon binding of the trimeric FasL to FasR, the latter arrange in a hexameric pattern, allowing to form the intracellular death domain which, in return, initiates caspase activation and thereby apoptosis induction [79]. Additionally, a FasL distance dependency of apoptosis signaling was suggested by Monzel and co-workers with most efficient apoptosis for 9 nm spacing between two FasL [20]. This data agrees well with the dimensions reported for the intracellular death domain by Scott et al. supporting the theory that FasL mediates the hexameric cluster formation and further signaling processes of FasR [20, 79, 80]. But so far, no study exists where they can control both FasL arrangement and number at the same time. Hence, it is yet unknown how these parameters effect FasL apoptosis induction. Therefore, I developed a DNA origami platform allowing a nanometer accurate placement of various number of FasL in different patterns, which will be described in the following. Results presented in the next chapter are adapted from Publication [P1].

4.1 | FasL DNA Origami Nanoagent Development

In order to have FasL arranged with certain distances at distinct places I used a one-layer DNA origami sheet (Fig. 4.1) [57]. FasL itself is trimerized via a T4-FOLDON and has a

C terminal Biotin. Accordingly, to attach FasL to the DNA origami two options were feasible:

1. Incorporate Biotin-DNA into the DNA origami and subsequently use wildtype (wt) Streptavidin to serve as a linker between DNA and FasL (s. Fig. 4.1 (A)).
2. Additionally, engineered monovalent (mv) Streptavidin coupled via maleimide chemistry to DNA was tested. Thereby, biotinylated FasL can attach to the single binding pocket of mv Streptavidin and the DNA can hybridize to handle DNA on the DNA origami (s. Fig. 4.3 (B)).

Evaluating the incorporation rate of both approaches with AFM, yielded an average number of 5 ± 0.3 wt Streptavidins and 4.9 ± 0.2 mv Streptavidins per DNA origami, respectively. Moreover, $(40 \pm 8)\%$ for wt and 32 ± 3 for the mv case were fully decorated with 6 FasL molecules. Furthermore, analyzing the AFM height profiles allowed the characterization of the functionalization with FasL on the Streptavidin-DNA origamis (s. App. Fig. A.1). Here, it was found that $(76 \pm 10)\%$ of analyzed DNA origamis having a Streptavidin attached, also carried a FasL. Along with these functionalizations, in total five different geometries were fabricated: three hexagonal patterns with an average inter-protein distance of 5 nm (NH5), 10 nm (NH10) and 30 nm (NH30). Also, two dimeric configurations were produced, where two FasL had either a distance of 10 nm (ND10) or 20 nm (ND20) (s. App. Tab. A.1). As AFM analysis successfully showed correct arrangement of Streptavidin and FasL, as a next step, a functionalization of these FasL DNA nanoagents to a surface, where cells would grow on, needed to be developed. Therefore, three surface attachment methods were tested:

1. Digoxigenin binding [113]
2. PEG-Thiol-Chemistry [59]
3. Cholesterol DNA in a lipid bilayer [114, 115]

Both, the first and the second option turned out to have major limitations. In the first case, the number of DNA origami localizable on the surface was very poor. In the second case, cells did not attach and hence made apoptosis analysis impossible. Therefore, I optimized the protocol for the attachment of FasL nanoagents onto a lipid bilayer as described earlier in the group of Liedl [114, 115]. As shown for the control sample in Figure 4.2 (A), cells adhered, spread and divided on the lipid bilayer. They were neither affected by the Cholesterol-DNA within the lipid bilayer, nor did the blank DNA origami cause apoptosis.

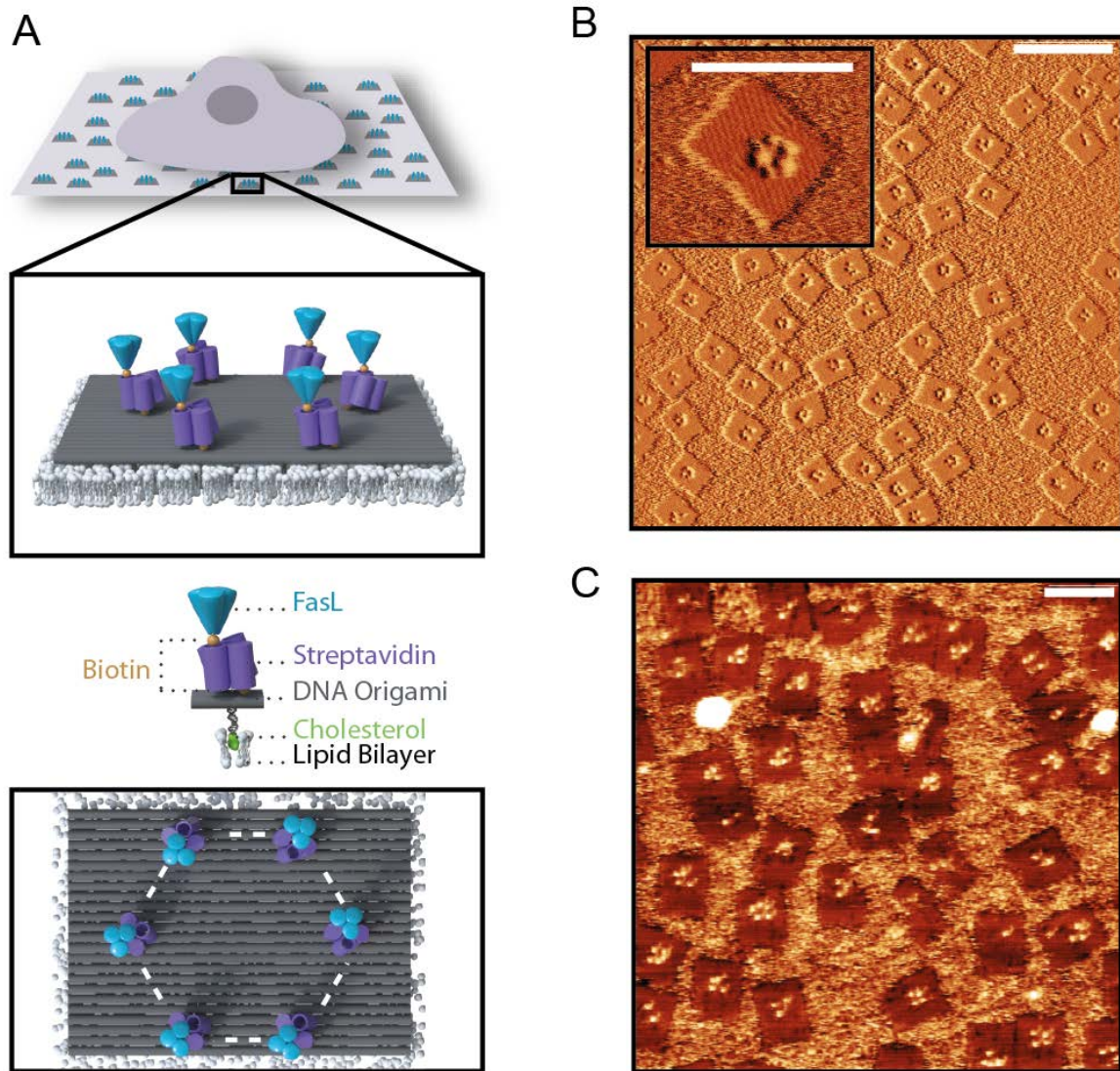


Fig. 4.1.: DNA origami functionalized with FasL. (A) Schematic illustration of a cell on a supported lipid bilayer functionalized with FasL nanoagents. The magnifications depict the FasL hexagonal arrangement on DNA origami via Streptavidin. (B) AFM Lock-In Amplitude image of DNA origami sheets on mica functionalized with Streptavidin (scale bar: 200 nm, color scale from dark to bright: 0 nm to 1.6 nm). The magnification shows the hexagonal attachment of Streptavidin on DNA origami (scale bar: 100 nm, color scale from dark to bright: 0 nm to 1.0 nm). (C) AFM image of the attachment of FasL and Streptavidin on DNA origami (scale bar: 100 nm, color scale from dark to bright: 0 nm to 4.5 nm).

4.2 | FasL DNA Origami Nanoagent is More Effective Than Single FasL Molecules

Therefore, these results allowed to further characterize FasL induced apoptosis on the functionalized lipid bilayer. When six FasL were arranged in a hexameric pattern with a distance of 10 nm between two adjacent FasL on the DNA origami, cells died immediately after briefly spreading (Figure 4.2 (A)). However, when FasL was membrane bound (without DNA origami) or in solution it also caused apoptosis, but substantially slower (on average 11 h later). To quantitatively analyze the event times of apoptosis, timelapse movies were recorded and label free apoptotic blebbing was manually analyzed for a minimum of 500 cells per condition, which was repeatedly verified in subsequent measurements. The distribution of apoptotic events over time for the hexagonal FasL arrangement is shown in Figure 4.2 (B). Here, it is observable that within only four hours after seeding the majority of cells had died. This also became obvious when analyzing the cumulative sum of apoptotic events (Figure 4.2 (C)). A higher percentage of cells died within the first four hours when subjected to NH10 compared to the control samples (soluble ~ 15 h, membrane bound FasL ~ 6 h and blank DNA origami < 24 h). Even at volume concentrations as low as 0.1 nM for the NH10, the majority of cells died within 4 h, whereas for 10 nM membrane bound FasL most cells died after 15 h. The statistical analysis of these results are shown in Figure 4.2 (D). Here, by calculating the inverse of the apoptotic event time τ_i for each cell, the apoptosis rate distributions were determined ($k_i = 1/\tau_i$) for a minimum of 500 cells per condition. The rank sum test revealed that the median apoptosis rate was significantly enhanced compared to the control samples (soluble or membrane bound FasL) even at higher volume concentrations. Taken together, these results confirm that, when FasL is spatially confined, apoptosis induction is efficiently enforced.

4.3 | FasL Conformation Influences Apoptosis Rate

Next, the effect of number and distance of FasL on apoptosis induction was investigated. As described earlier, five different FasL arrangements had been designed. In Fig. 4.3 (A) the peak location analysis is shown for different FasL configurations and the fitted peak locations are shown in App. Tab. A.1. Interestingly, only for the 10 nm distance between

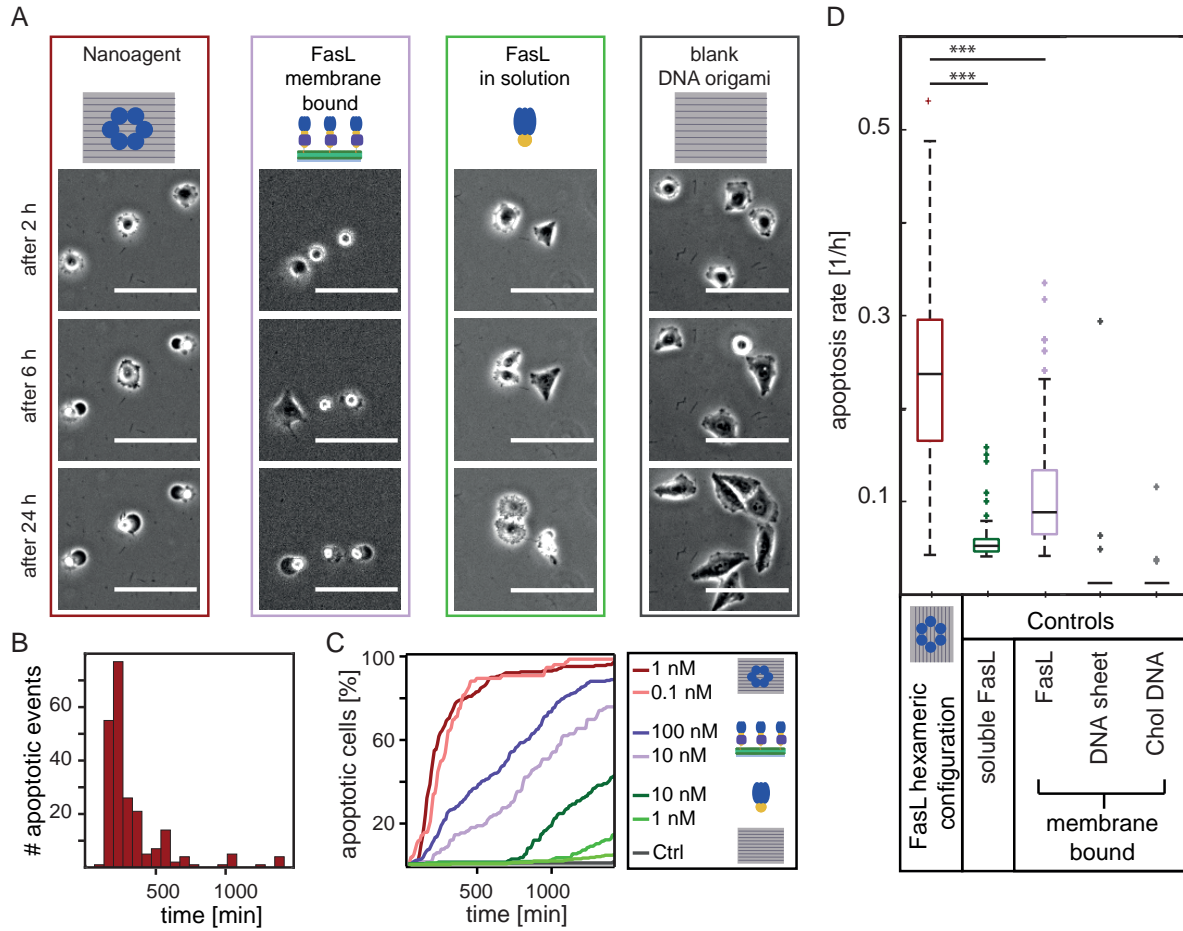


Fig. 4.2.: Comparison of FasL apoptosis induction. (A) Exemplary brightfield images showing cell reaction when seeded on membrane with FasL attached to DNA origami (red), FasL attached to membrane (lilac), FasL in solution (green) and control sample with blank DNA origami (grey) at different time points after seeding (2 h, 6 h and 24 h). Cells in the control samples spread and divide, but in the nanoagent sample apoptotic blebbing is induced quickly. (B) Histogram analysis of apoptotic blebbing events over time for 1 nM FasL nanoagent, showing within 4 h most cells die. (C) Cumulative sum of apoptotic cells normalized by total analyzed cells for each condition ($n < 500$ cells/condition). Apoptosis induction is most efficient for the FasL nanoagent (red), less effective if FasL alone is functionalized onto lipid bilayer (lilac), but more efficient than soluble FasL (green). (D) Comparison of median apoptosis rate for 1 nM FasL nanoagent, 1 nM soluble FasL and 10 nM membrane bound FasL, unfunctionalized DNA origami and Cholesterol coupled DNA. Significant enhancement of apoptosis rate for FasL nanoagent compared to soluble or membrane bound FasL is observable. Unfunctionalized DNA origami or DNA alone do not affect cells. $n < 500$ cells/condition. Ranksum test: $***p < 0.001$, $**p < 0.01$, $*p < 0.05$.

two adjacent FasL in an hexameric arrangement efficient apoptosis induction was evident ((3.1 ± 0.1) h). For larger and smaller distances, death times were significantly larger ((14.0 ± 0.3) h and (11 ± 1) h), respectively. Moreover, the data indicates that spacing has a more pronounced effect than number. For the FasL Dimer configurations (ND10 and ND20) also fast apoptosis induction was observable ((3.6 ± 0.1) h). However, comparing it to the NH10 sample, the second peak after roughly 5 h was more pronounced for the FasL Dimer configurations compared to the NH10. Also, statistically comparing the time-to-death distributions of the FasL Dimer arrangements with the NH10 probe revealed that NH10 induced apoptosis 3 x significantly more efficient. When comparing the FasL Dimer configurations among themselves, it was observable that the 10 nm distance was 2 x significantly more effective than 20 nm spacing. For FasL attached to the membrane without arranging it on a DNA origami, the first peak was detectable after (6.0 ± 0.4) h. Another second peak is localizable at times comparable to the large hexagonal conformation ((14 ± 1) h).

As the wildtype Streptavidin has in total four binding pockets, two of them would be addressable for FasL attachment - although sterically unlikely. Hence, one cannot exclude the possibility that two FasL bind at the same defined location on the DNA origami. In order to rule out this artefact, all experiments presented above were repeated with the monovalent Streptavidin attachment strategy (Fig. 4.3(B)). Although, the general trends were well reproducible, overall the apoptosis times were significantly larger. Also, here the NH10 arrangement was most efficient in apoptosis induction, compared to the larger or smaller hexagonal arrangements as well as the FasL Dimer or Monomer conformations. Nevertheless, the first detectable peak locations shifted to 5 h. Additionally, the second peaks for the monovalent attachment methods were more pronounced compared to the wildtype Streptavidin configurations. Possible explanations for these deviations will be given in Chapter 4.5. Nonetheless, as the key findings were also for the monovalent coupling well reproducible, in summary, these results prove that spacing of FasL molecules plays an important role in apoptosis induction. Furthermore, they illustrate that number of FasL is less crucial than distance.

4.4 | FasL DNA Origami Nanoagent Potency

Having demonstrated that NH10 induces apoptosis efficiently raised the question how potent is the FasL nanoagent? In other words: how many nanoagents are needed to kill one cell? In order to answer this question, I quantified the number of fluorescently labelled DNA origami on a lipid bilayer for varying initial volume concentrations (Fig.4.4

(A)). Moreover, different time points during the preparation process were monitored e.g. wash steps and medium exchange. This investigation revealed that after three hours in cell medium the number of detected DNA origamis decreased by 50% compared to the initial number. Here, it needs to be noted that the functionalization with Cholesterol is not covalent and hence a substantial loss of DNA origamis during wash steps needs to be accounted for. Nevertheless, a nanoagent surface concentration was obtainable for which apoptosis induction was most efficient (Fig. 4.4 (B)). No significant reduction in death-

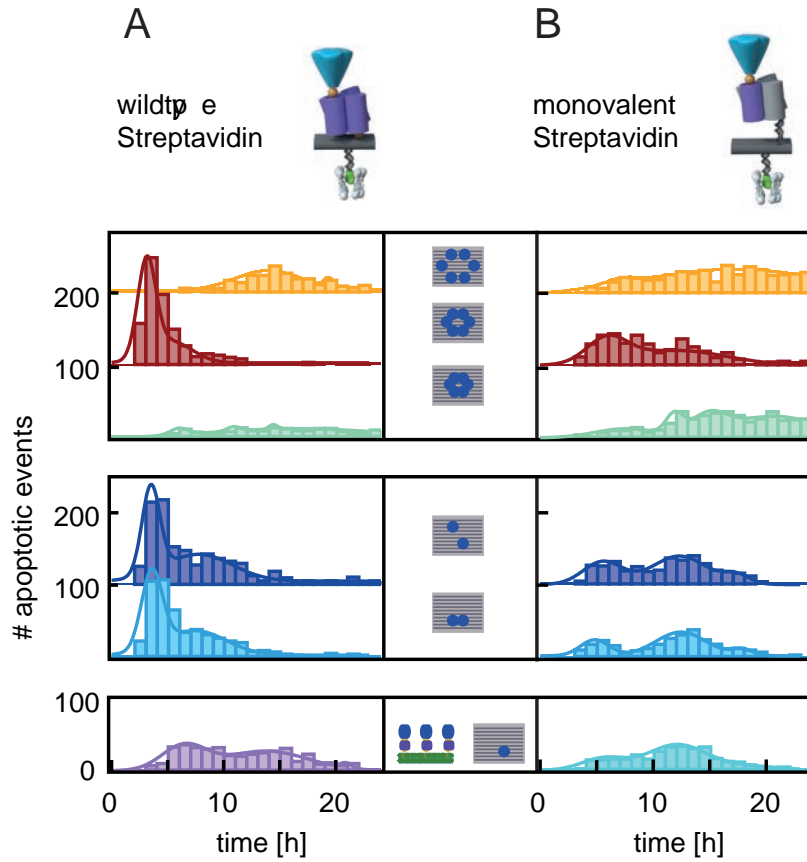


Fig. 4.3.: Distance dependency of FasL apoptosis induction. Comparison of distributions of apoptotic event times for different FasL configurations on DNA origami as shown in legend for the wildtype (A) and monovalent (B) Streptavidin functionalization. Histograms were fitted with up to three Gaussian distributions (peak locations are given in App. Tab. A.1). Fastest apoptosis was observable for NH10 (red), ND10 (blue) and ND20 (dark blue). For hexagonal arrangements with larger (NH30, orange) and shorter (NH5, mint) distances, as well as membrane bound FasL (10 nM, lilac) or single FasL on DNA origami (Monomer FasL, light blue) apoptosis was significantly reduced. Overall, apoptosis induction timing was significantly reduced for the monovalent functionalization compared to wildtype Streptavidin.

times was detectable between 0.6 up to 4 nanoagents per μm^{-2} . However, further decreasing the surface concentration resulted in a significant reduction of the apoptosis rate. Therefore, the data indicates that a saturation regime is observable above a critical surface concentration. To estimate how many nanoagents on average are in contact with a single cell, a cell surface of $1600\mu\text{m}^2$ is presumed [116]. Therefore, around 80 nanoagents per cell were estimated for a surface concentration of $0.6\mu\text{m}^{-2}$. Accounting for the average occupancy efficiency of Streptavidin (83 %) and FasL (76 %) as mentioned earlier, a number of fully functional nanoagents can be approximated to 50 per cell. Essentially, this shows that less than 100 nanoagents per cell are required to efficiently induce apoptosis, which indicates a very high potency of the nanoagent.

Finally, the apoptosis induction efficiency for NH10 in solution was studied (Fig. 4.4 (C)). In contrast to the surface bound nanoagents, the apoptosis rate asymptotically reaches saturation with increasing nanoagent volume concentration and is comparable to a typical binding isotherm. Fitting the data with the Hill equation,

$$y = \frac{\max}{1 + \frac{x_{1/2}}{x}} \quad (4.1)$$

with the maximal rate at $\max = (0.29 \pm 0.02) \text{ h}^{-1}$ therefore allows to determine a critical volume concentration $x_{1/2}$ for efficient apoptosis induction of $(0.09 \pm 0.02) \text{ nM}$. Assuming a $K_D = 90 \text{ nM}$ as suggested by literature a number of roughly 100 nanoagents per cell can be estimated, which agrees well with the number obtained for the surface bound nanoagent [117]. Additionally, when comparing these numbers to data obtained for single FasL in solution, one finds that even at 100 times higher numbers of FasL per cell (e.g. for a volume concentration of 10 nM), apoptosis induction is remarkably weaker. In conclusion, this data provides evidence that stimulating cells with FasL presented in an optimal hexagonal arrangement, efficiently triggers apoptosis.

4.5 | Discussion

To summarize, I successfully designed, produced and evaluated a DNA origami platform for the study of FasL arrangement on apoptosis induction. I was able to show that FasL positioned with an optimal spacing efficiently enhanced apoptosis signaling compared to single FasL membrane bound or in solution (Fig. 4.2). Additionally, it became evident that the distance between two FasL had a more pronounced effect compared to number (Fig. 4.3). Comparable observations have also been made in the area of immuno-stimulation. Veneziano et al. for example have reported that a defined spacing

distinctively triggered B cell immune response [19]. Also, for FasL it was shown that two linked FasL substantially increase apoptosis efficiency [81].

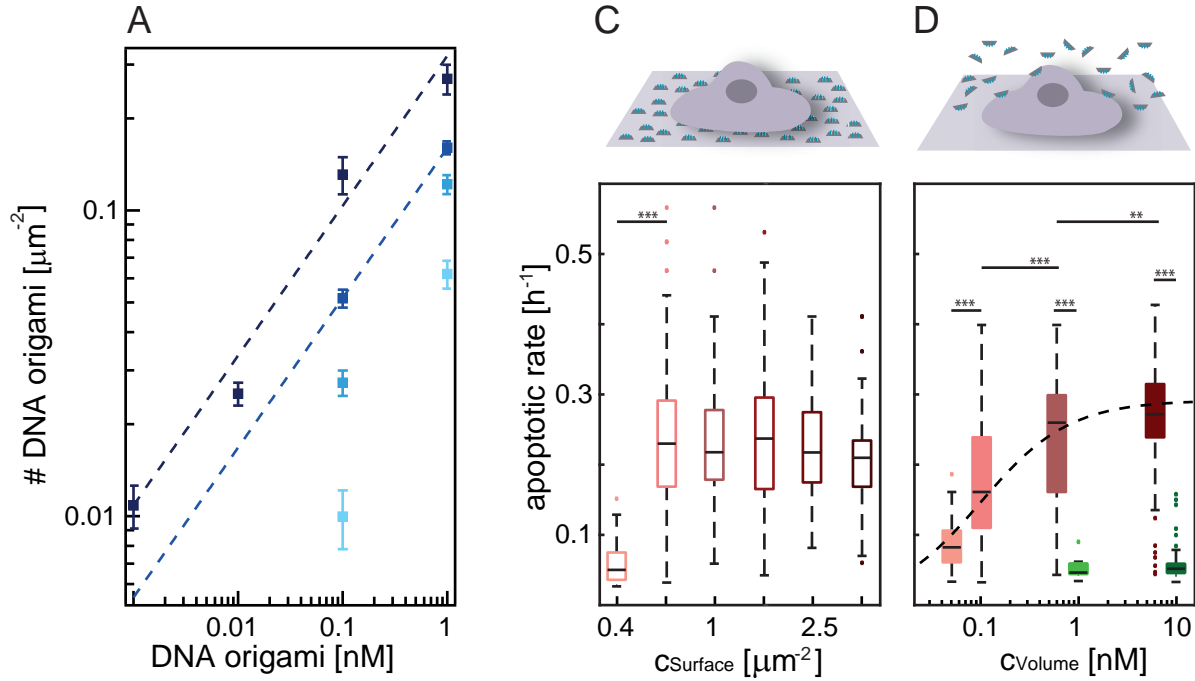


Fig. 4.4.: High apoptotic potency for low FasL nanoagent concentrations. (A) Average DNA origami number determined on lipid bilayer for various initial volume concentrations. Different colors represent different time points during measurement from dark to bright: initial DNA origami number after functionalization on lipid bilayer, after washing and changing to cell medium, after 3 h in cell medium and after 24 h in cell medium. Fit $f(x) = a * x^b$ with $a = 0.32 \pm 0.001$, $b = 0.49 \pm 0.3$ and extrapolation curve with $b_2 = b$, $a_2 = 0.16 \pm 0.004$ (B) Median apoptosis rate of FasL nanoagent at different surface concentrations. A drop of apoptosis rate is observed below $0.6 \mu\text{m}^{-2}$. For higher concentrations no significant apoptosis enhancement is observable. (C) Comparison of median apoptosis rate of FasL nanoagent (red) or single FasL (green) in solution at different volume concentrations. Asymptotic saturation for increasing volume concentrations observable, fitted with Eq. 4.1 with $\text{max} = (0.29 \pm 0.02) \text{ h}^{-1}$ and $x_{1/2} = (0.09 \pm 0.02) \text{ nM}$. $n < 100$ cells/condition. Ranksum test: $***p < 0.001$, $**p < 0.01$, $*p < 0.05$.

Additionally, with the DNA origami platform, an optimal spacing of 10 nm was deducible, which agrees well with the values reported by the group of Monzel and by Scott et al. [20, 80]. In the former study they attached FasL to a supported lipid bilayer and by varying the number of FasL incorporated, they estimated the average spacing between two FasL [20]. However, they were not able to provide evidence whether number or positioning

played a role. Moreover, here I observed that, when comparing the nanoagent to membrane bound FasL, a significant reduction in the apoptosis triggering time was detectable (Fig. 4.2). Furthermore, an even more pronounced effect was obtainable when comparing single FasL to FasL-nanoagents in solution. Although a 1000-fold lower concentration was used, the hexagonal arranged FasL with a 10 nm spacing was significantly more potent than soluble FasL. Also, Zhang et al. measured an enhancement when they functionalized up to six Fas peptides to a DNA tetrahedron [83]. However, they only observed an 8-fold increase in potency compared to the soluble peptide (5 μM compared to 40 μM) [83]. Instead, with concentrations lower than 1 nM efficient apoptosis triggering was detectable for the FasL nanoagent applied in this study. An explanation for the higher potency compared to the study by Zhang et al. might result from their three dimensional tetrahedron design, which presumably does not allow a simultaneous interaction of more than three Fas peptides with the cell at the same time. Also, their Fas-DNA tetrahedron putatively is more flexible, which could be a reason for a smaller apoptosis enhancement compared to my study. In fact, when using the monovalent Streptavidin coupling, I also found a reduction in apoptosis efficiency compared to the wildtype Streptavidin attachment method presumably resulting from higher flexibility. One could also presume that the higher efficiency is due to the fact that up to two FasL can bind to the wildtype Streptavidin, whereas for the monovalent only a single FasL can attach. However, this assumption is contradicted by the results obtained for the larger (NH30) and smaller hexagons (NH5). The data suggests that unfavorable distances between two FasL weaken apoptosis triggering. Also, we hypothesize that it is sterically unfavorable that multiple FasL bind to the same Streptavidin simultaneously. Instead, it is more likely that the higher flexibility of the mv Streptavidin functionalization reduces apoptosis efficiency. In fact, the coupling of mv Streptavidin necessitated the hybridization of the DNA coupled to the mv Streptavidin to a DNA origami handle. Additional to the size of the Streptavidin itself (roughly 5 nm), the DNA linker adds roughly 6.8 nm on top. On the one hand, for mv Streptavidin we therefore obtain a reduction in location precision and on the other hand, an increase in flexibility.

To generate an even more precise localization on the DNA origami, it might be favorable to omit Streptavidin and test direct functionalization of FasL to DNA. A technique which gained a lot of interest in the recent years concerning protein DNA engineering is using unnatural aminoacids [118–120]. Also other protein-DNA linking methods exist, however, unnatural aminoacids provide the smallest possible covalent linker. Here, for example an azide modified aminoacid could be incorporated at the C-terminus of FasL and via click chemistry react with dibenzocyclooctyne (DBCO) on DNA [121, 122]. Nonetheless, the

data with a larger linker provides strong evidence that the distance between two FasL molecules crucially defines apoptosis triggering. The fact that not only small distances (5 nm) but also larger distances (30 nm) reduce apoptosis efficiency might hint towards inner cell mechanisms preventing apoptosis signaling. Also, this excludes that multivalency effects alone play a role, which would result in an increasing binding strength for a larger number of FasL on the DNA origami. Rather a correct conformation of FasL with optimal distances significantly effect apoptosis (NT10, ND10 and ND20). Up to now, a recognized theory for FasL induced apoptosis suggests that upon FasL binding to FasR, the intracellular unit of the transmembrane receptor switches from an inactive to an active conformation. Thereby the dimerization of the intracellular deathdomain (DD) is initiated, which in return enables caspase activation (s. Chapter 2.3.3) [79, 80, 84–87]. A possible explanation for the reduced apoptosis rates for smaller and larger FasL spacing, therefore, might be that the dimerization is hindered. Shorter distances than 10 nm between two adjacent FasL might prohibit DD dimerization, whereas larger distances above 20 nm might initiate multiple individual dimerization initiation points but hinder the formation of a hexagonal cluster formation as suggested by literature [79, 80, 84, 85]. Overall, I was able to show that DNA nanotechnology serves well as a tool for studying nanoscale organization of ligands effecting signaling pathways in cells. The results shown affirm that distance and arrangement of FasL play a pivotal role in apoptosis signaling.

5 | FCS as a Method to Study Ligand Interactions on Living Cells

Ligand receptor interactions are often the initiation point for signaling pathways within the cell and thereby facilitate communication of a cell with its surrounding (s. Chapter 2) [6]. Characterizing binding of a ligand to a transmembrane receptor is therefore crucial to understand the underlying processes [79]. Additionally, the strength of binding usually relates to the potency of a ligand and can provide insights about drug efficiencies [123]. Hence, for research as well as for drug discovery, techniques allowing the determination of reliable binding affinities are of utmost importance. Currently, flow cytometry is commonly used for studying ligand binding to living cells [124–127]. However, this technique does not allow equilibrium measurements and is therefore limited to slow off-rates. Furthermore, usually high sample amounts are required to create good statistics. Other assays such as Surface Plasmon Resonance (SPR), enzyme-linked immunosorbent assay (ELISA) or EMSA can only measure binding on artificial membranes or single receptors [108, 128, 129]. New methods applying for example superresolution to resolve binding interactions need fixed cells and hence, do not facilitate measurements on living cells [89]. Both FCS and FCCS have already been successfully tested for determining binding statistics on the plasma membrane, but also here, fixed cells are essential [130–133]. Up to now, to our knowledge, there is no technique available which allows the characterization of binding to living cells with low sample consumption. We, therefore, tested an approach to measure binding of fluorescently labeled ligands to living cells by monitoring the concentration of unbound ligands in a titration experiment using FCS. This method will allow equilibrium measurements and thereby enable the characterization of a large range of K_D values. Additionally, these measurements can provide insights about time dependent processes such as internalization, and on- and off-rates should be obtainable. As equilibrium relaxation after dilutions are measurable without any washing steps, also fast off-rates should be accessible. Last but not least, we seek to build a set-up with low sample consumption enabling the characterization of rare and precious samples.

Results shown in the following are adapted from the Manuscript [M1]

5.1 | Ligand Depletion Theory

The principle of our approach relies on determining concentration of free ligand with FCS, instead of characterizing the amount of bound ligand. As cells are added to the sample volume, ligands will bind to their receptors and the concentration of free ligand will decrease, which we refer to ligand depletion (Fig. 5.1 (A)). As the concentration is inversely proportional to the number of fluorescent ligands within the detection volume, the amplitude of the autocorrelation curve will increase the more ligands are bound to cells (Fig. 5.1 (B)). In detail, the general formalism is based on binding equilibrium kinetics as introduced earlier in Chapter 2.1. The free ligand concentration is described by the following formula:

$$[L]_{free} = [L]_0 - \frac{(K_D + [R]_0 + [L]_0 - \sqrt{(K_D + [R]_0 + [L]_0)^2 - 4[R]_0[L]_0})}{2} \quad (5.1)$$

Here, $[L]_0$ is the total ligand concentration. The total receptor concentration, $[R]_0$, depends on the number of receptors per cell N_R as well as the total number of cells N :

$$[R]_0 = \frac{N_R N}{V N_A}, \quad (5.2)$$

where V refers to the sample volume and N_A the Avogadro constant. The decrease in concentration depends on the binding strength of the ligand, as well as the receptor concentration defined by the amount of cells added (s. Fig. 5.1 (C)). The higher the receptor concentration or the binding strength the larger the expected depletion shift. A titration experiment is carried out to obtain the binding strength of a ligand and the depletion curve is fitted with Eq. 5.1 with K_D as a free parameter.

Therefore, the measurable K_D range can be controlled with the number of cells added. The HEK-293 cells tested in this study express 900 000 CD33 receptors upon antibiotic induction (s. App. B.4). To obtain 100 nM receptor concentration in a sample volume of 200 μ l, the number of cells needed can be estimated by:

$$N = \frac{[R]_0 N_A V}{N_R} \approx 10000000. \quad (5.3)$$

According to these assumptions, FCS depletion measurements should be feasible for K_D values up to 100 nM.

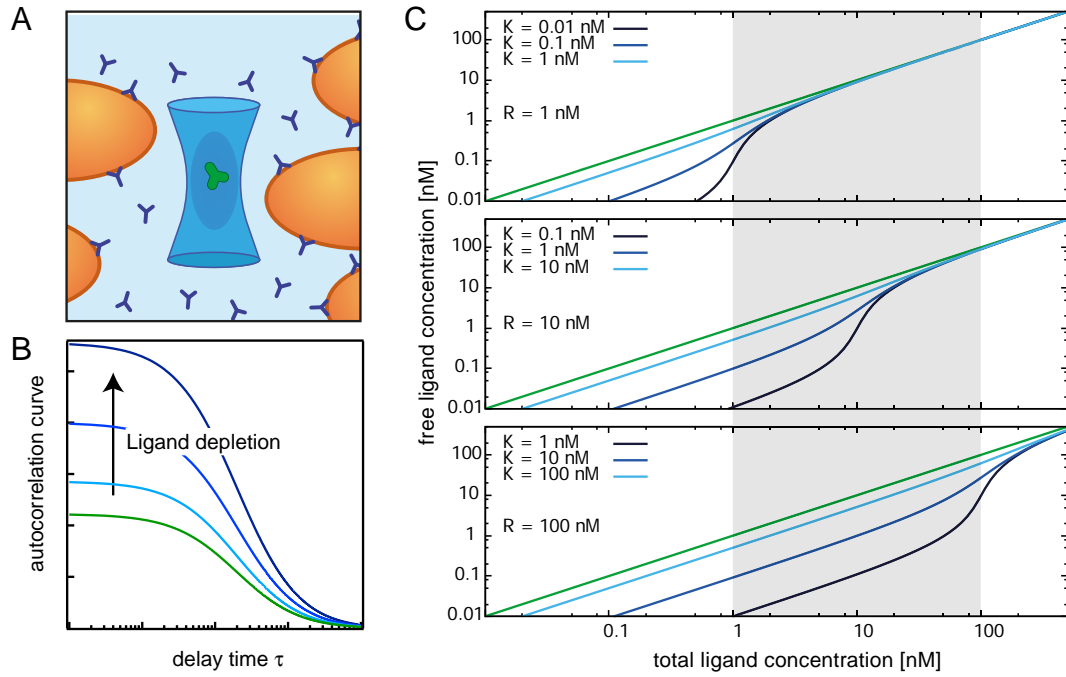


Fig. 5.1.: (A) Schematic illustration of ligand depletion. The concentration of free ligands will decrease upon binding to cells. (B) Ligand depletion is proportional to the autocorrelation amplitude. The more ligands are bound, the lower the measured concentration in the detection volume. (C) Effect of receptor concentration on depletion shift. The higher the receptor concentration, the larger the depletion shift. The grey-shaded area denotes the linear concentration regime for FCS as determined in Fig. 5.3

5.2 | Probe Characterization

Having introduced the concept of ligand depletion, next the ligand itself will be characterized. We decided to use a commercially available Alexa 488 antibody (AB) targeting the CD33 receptor which is expressed on HEK-293 cells upon induction. First, AB binding was verified and characterized with flow cytometry. Next, the diffusional and fluorescent characteristics in different buffers were investigated with FCS. Furthermore, the linear regime, in which reliable concentration estimations are accessible, was evaluated via a titration experiment with FCS.

5.2.1 | Alexa 488 Antibody Binds to Cells

Flow cytometry characterization verifies binding and allows a K_D estimation (Fig. 5.2). Here, the fluorescence of each cell is obtained individually and the distribution of the whole cell population is studied. A titration series with different antibody concentrations

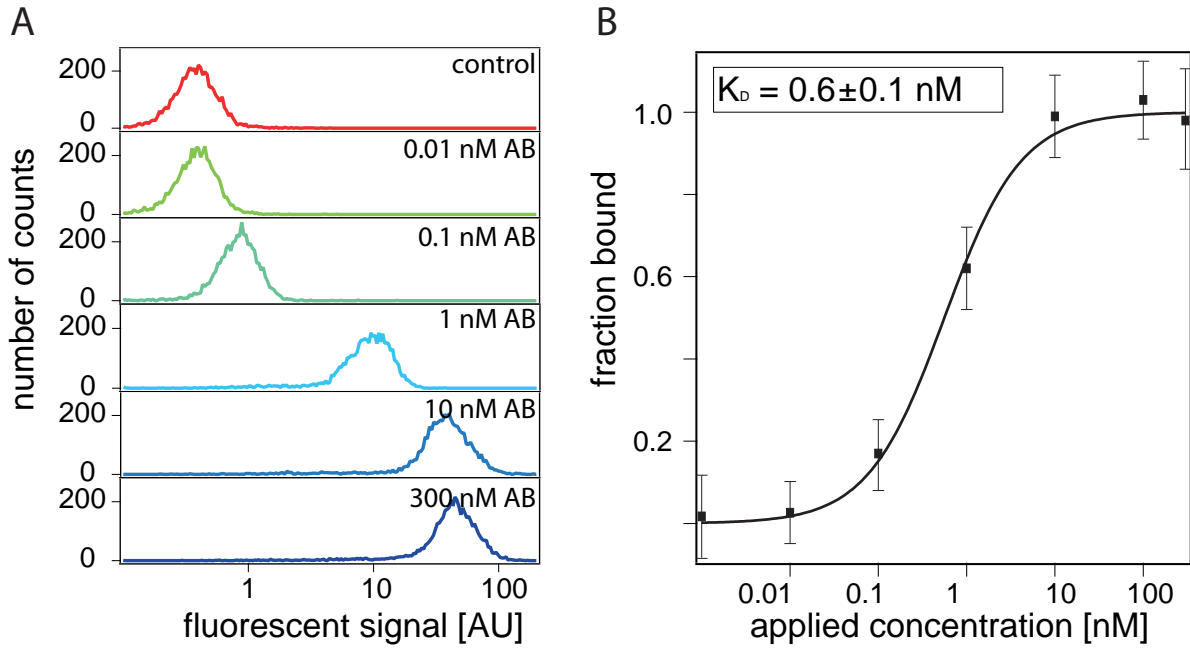


Fig. 5.2.: Flow cytometry characterization of Alexa 488 antibody binding to induced HEK-293 cells. (A) For different antibody concentrations the fluorescent signal of the cells was obtained (number of cells $N = 5000$). The fluorescence shift allows to estimate the fraction of antibodies bound per cell (B). Fit yields a $K_D = (0.6 \pm 0.1) \text{ nM}$.

is shown in Fig. 5.2 (A). With increasing antibody concentration, the fluorescence per cell rises. To estimate the fraction of antibodies bound, the fluorescence distribution shift was normalized to the highest fluorescent values with and without antibody (control). Fitting these values in relation to the applied antibody concentration allowed the determination of the binding strength of the antibody to the CD33 receptor ($K_D = (0.6 \pm 0.1) \text{ nM}$).

5.2.2 | Diffusional Characteristics

Next, the fluorescent and diffusional characteristics of the AB were investigated using FCS in different buffers and a linear concentration regime was obtained (Fig. 5.3). To elucidate effects of buffer changes on the fluorescence of the antibody FCS measurements were compared in PBS and cell supernatant (Fig. 5.3 (A)). No significant deviation in countrate or diffusion time was obtained. Therefore, it can be assumed that upon cell addition, the buffer change should not influence the concentration measurement. Two-component fits were carried out yielding $\tau_D = (275 \pm 18) \mu\text{s}$, where the fast diffusing component presumably originates from free dye and was set to $\tau_D = 25 \mu\text{s}$.

When inspecting the countrates, occasionally large spikes were observable, probably

generated by AB aggregates. However, omitting these curves in the further analysis, allowed to extract a titration curve, as shown in Figure 5.3 (B). The titration curve was fitted with the background corrected function $f(x) = x a (1 + v/x)^2$, where v denotes the relative background ($a = 3.34 \pm 0.02$, $v = 0.03 \pm 0.2$) [134]. The data indicates that concentration measurements are feasible in both buffers, as the curves overlap well. Indeed, there was no increase in autofluorescence observable when cell supernatant was used. In order to obtain the molar antibody concentration the data was fitted with a linear fit giving a conversion factor of 12.7 nM/ μ g. Using this calibration, a regime was obtainable where a linear relation between added antibody concentration and measured antibody concentration was accessible (Fig. 5.3 (B) grey-shaded area). Hence, between 1 nM and 100 nM a reliable concentration measurement with FCS in cell medium is possible.

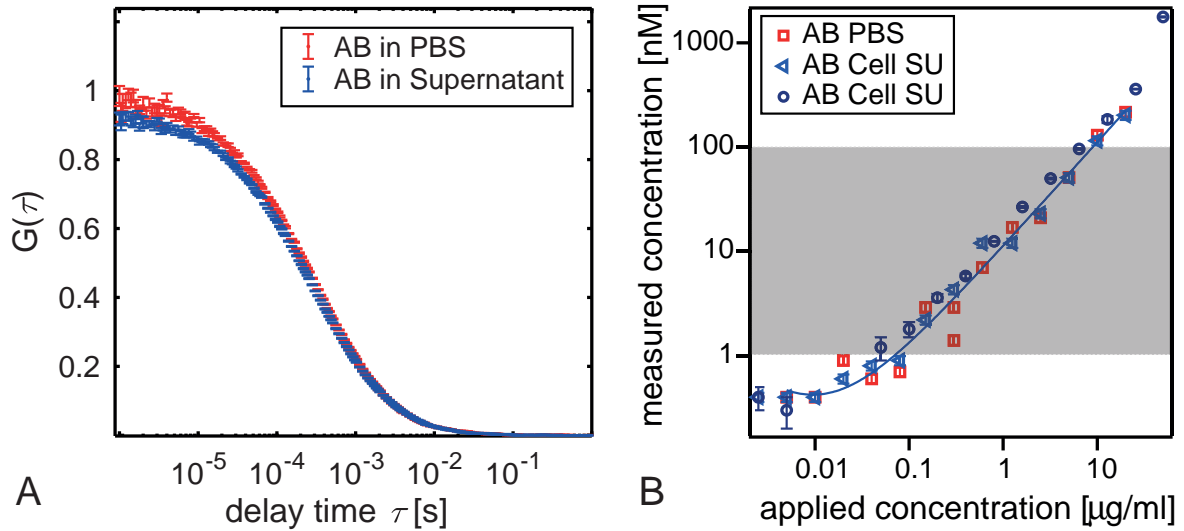


Fig. 5.3.: Characterization of Alexa 488 antibody in different buffers. (A) Comparison of normalized autocorrelation curves in PBS (red) and in cell supernatant (blue). (B) Titration experiments of Alexa 488 AB in PBS (red) and cell supernatant (blue). Independent of buffer condition similar values were obtained. To determine the influence of background noise at low concentrations, data points were fitted with the background corrected function $f(x) = x a (1 + v/x)^2$, ($a = 3.34 \pm 0.02$, $v = 0.03 \pm 0.2$). The grey shaded area visualizes the linear regime, optimal for FCS measurements.

5.3 | Set-ups for the Separation of Cells from the FCS Measurement Volume

A crucial step for these FCS binding measurements was to create a cell-free detection volume to hinder diffusing cells from disturbing the FCS signal. Therefore, various set-ups were developed (Fig. 5.4). Two different types of set-ups had been tested to prevent cells from entering the measurement volume. In the first type, a membrane serves as a separation. In the second type, a hydrogel creates a cell free measurement area.

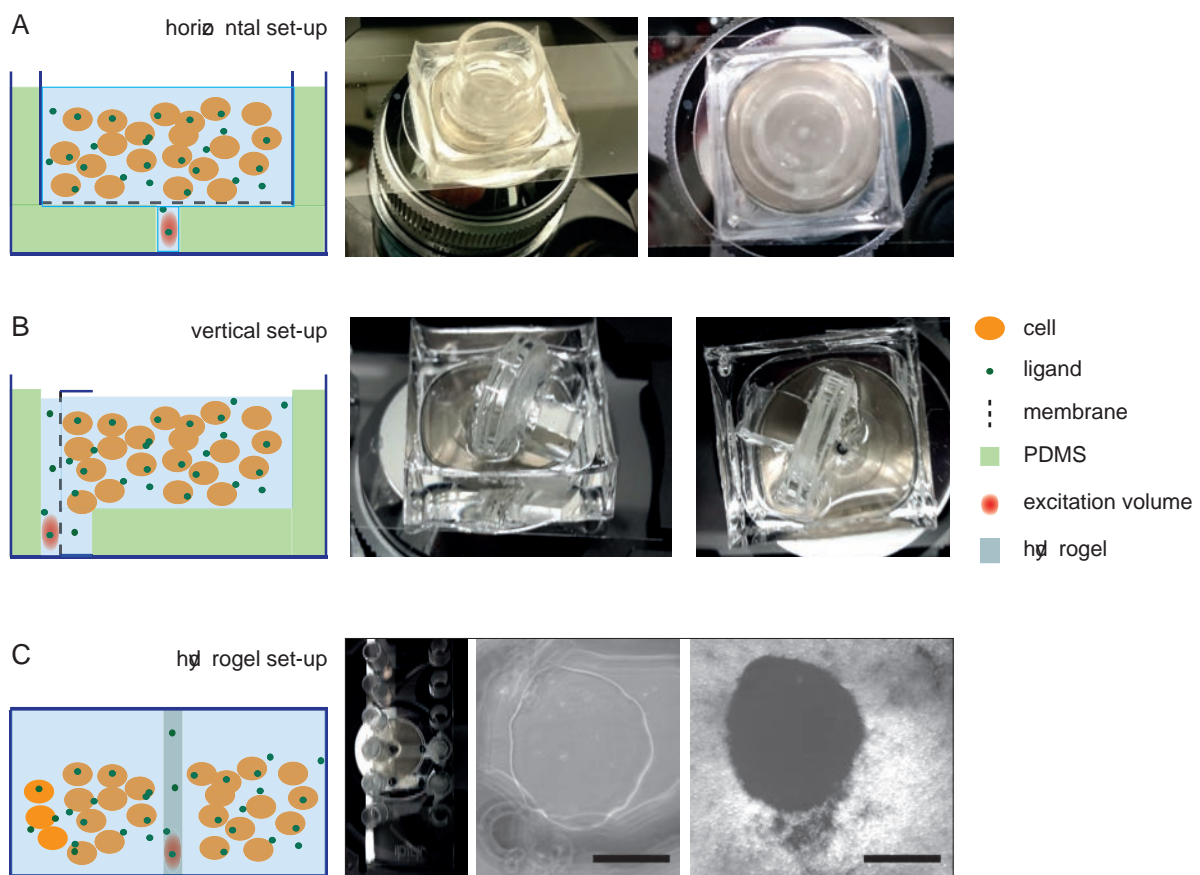


Fig. 5.4.: FCS set-ups for depletion measurements. (A) Cell culture insert with membrane at bottom surrounded with PDMS that separates cells from the small measurement cavity. (B) Vertical membrane separation to avoid bubbles hindering diffusional exchange. (C) Hydrogel serves as a separation between the cells and the detection area. FCS signal was recorded within the hydrogel, allowing for ligand exchange. Hydrogels were UV induced in an Ibidi Chamber (left image). Middle image: hydrogel without cells; right image: hydrogel surrounded with cells. Scale bar 500 μm .

First, a membrane-insert was used, which was surrounded by PDMS to minimize the sample volume. A small channel beneath the membrane was created to allow FCS signal measuring (s. Figure 5.4 (A)). Due to presumably encapsulated bubbles which supposedly hinder ligand exchange between the cell compartment and the FCS measurement area, a vertical set-up was also tested. Here, the measurement channel is separated vertically from the cell compartment with a membrane (s. Figure 5.4 (B)).

Last but not least, instead of a membrane, a hydrogel was used as a separation barrier for cells. For this set-up, the detection volume was placed inside the hydrogel which allowed AB diffusion but hindered cells from entering (s. Figure 5.4 (C)).

5.4 | Cell Measurements with FCS

According to measurements shown in Chapter 5.2 and ligand depletion theory in Chapter 5.1, measurements should be possible with an antibody concentration between 1 nM to 100 nM. For a receptor concentration of 50 nM, an antibody concentration of 20 nM, and a K_D value of 0.6 nM a free ligand concentration of 0.4 nM is expected (s. Eq. 5.1). Hence, a depletion shift of 19.6 nM is theoretically presumed. In the following, first, the measurements done with the cell culture insert are discussed. Secondly, hydrogel measurements are depicted.

5.4.1 | Membrane Insert Set-ups

The cell culture inserts from Millicell contain a membrane with a pore size of $3\mu\text{m}$ and thereby hinder cells from diffusing into the detection volume but allow ligands to pass through. The effect of cell addition on the antibody autocorrelation curve is shown in Figure 5.5. Firstly, an antibody solution was added to the channel (2 $\mu\text{g}/\text{ml}$ corresponding to 25 nM as shown in Figure 5.3). Secondly, the insert was added without cells to correct for possible concentration effects due to ligand interaction with the insert. Thirdly, cells which contained 2 $\mu\text{g}/\text{ml}$ antibody, were added to the insert to obtain a total receptor concentration of 45 nM (Figure 5.5 (A)) without changing the initial antibody concentration. After 30 minutes incubation, the receptor concentration was stepwise increased to a total concentration of 300 nM by adding more cells (Figure 5.5 (B)). After cell addition, a signal drop due to antibody binding was not observable. Instead, the autocorrelation amplitude decreased referring to an increase in concentration. Hence, no depletion shift was obtainable.

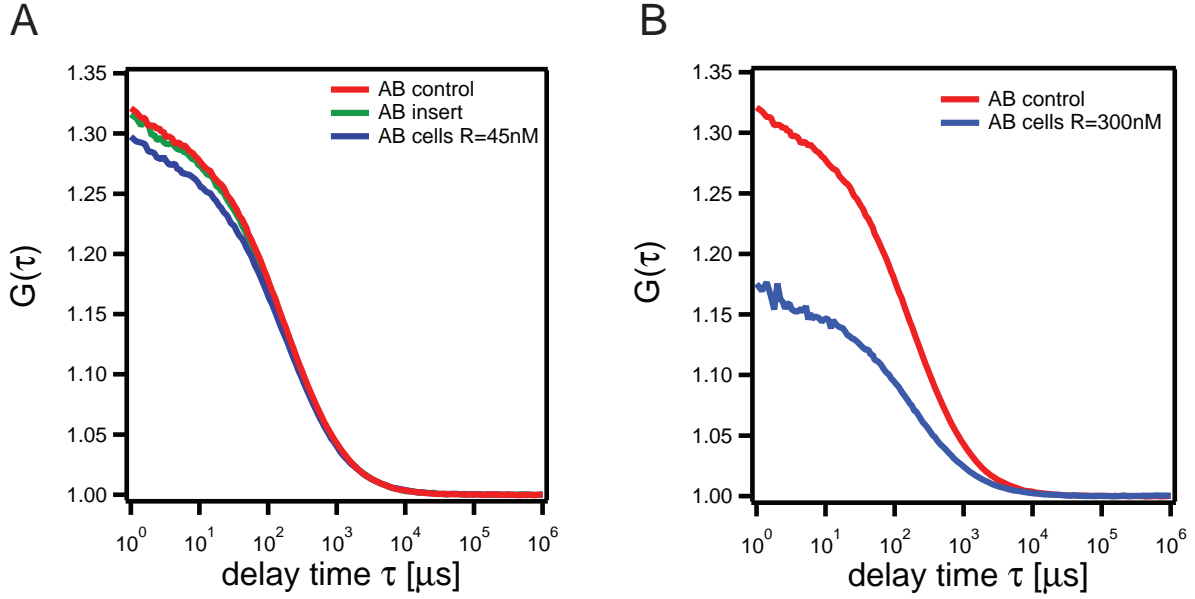


Fig. 5.5.: Antibody binding measurement with membrane insert. Comparison of auto-correlation curves for different concentration of induced HEK-293 cells ((A) $[R_0] = 45 \text{ nM}$, (B) $[R_0] = 300 \text{ nM}$). Instead of an increase in autocorrelation amplitude (decrease in concentration), amplitudes rises and hence, no binding was detectable.

5.4.2 | Hydrogel Set-up

As the membrane set-up did not allow to measure ligand depletion, another set-up using a hydrogel as separation between cells and measurement volume was tested. The hydrogel was produced with UV illumination in an Ibidi slide as previously described by Dietrich et al. with an average mesh size in the nanometer regime [135]. First, measurements within and outside of the hydrogel were compared to test whether the gel affected antibody diffusion (Fig. 5.6(A)). For the data within the hydrogel a larger tail towards higher diffusion times was observed and the standard diffusion autocorrelation fit could not be applied. Instead, Eq. 3.16 was modified with the factor α accounting for anomalous diffusion:

$$G(\tau) = N^{-1} \left[\left(1 + \left(\frac{\tau}{\tau_D} \right)^\alpha \right)^{-1} \left(1 + \omega^{-2} \left(\frac{\tau}{\tau_D} \right)^\alpha \right)^{-1/2} \right] \quad (5.4)$$

Fit parameters are given in Table 5.1. The anomalous diffusion putatively arises from antibodies stuck within the hydrogel matrix and therefore explaining the large tail in the autocorrelation curve. To test whether the hydrogel acts as a barrier for cells, dilution experiments were conducted. Three simultaneous measurements were recorded: One where HEK cells expressing CD33 were added to the channel; in another channel HEK

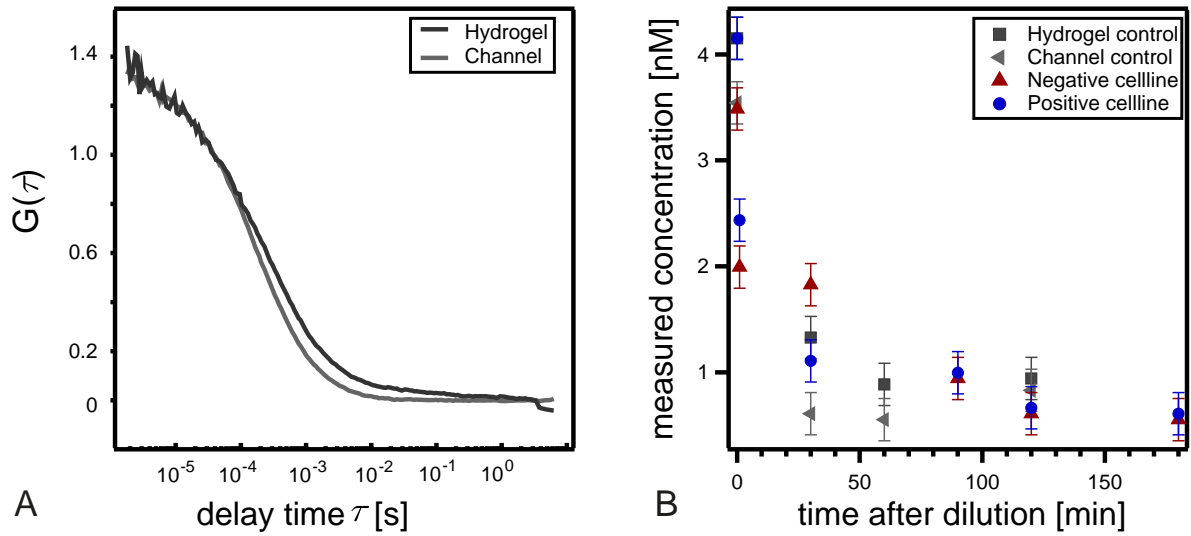


Fig. 5.6.: Antibody cell measurement with hydrogel set-up. (A) Comparison of normalized average autocorrelation curves within (dark grey) and outside (grey) of the hydrogel. (B) Comparison of measured concentration after dilution with CD33 negative cells (red), CD33 positive cells (blue) and cell supernatant in hydrogel (dark grey) and in channel (light grey), respectively. Expected equilibrium time 2h for a hydrogel size of 900 μm . After 2.5h the concentration of the positive and negative cell sample leveled at (0.6 ± 0.2) nM.

cells lacking CD33 receptors were used as control cells and two control samples were acquired within and outside of the hydrogel. Here, solely cell supernatant was used to account for the dilution upon cell addition. The hydrogels measured a size of about (900 ± 70) μm (Fig. 5.4 (C)) defining a equilibration time of roughly 2 h. First, in each channel an antibody concentration of 20 nM was added. Sequentially, the concentration within and outside of the hydrogel was measured for all three chambers. As shown in Figure 5.6 (B) the measured concentration $((4 \pm 2)$ nM) was significantly lower than the titrated concentration of 20 nM. Also, the determined concentration of sequential measurements within the same channel deviated by 2 nM. After two hours, 75 μl antibody solution was pipetted out of all channels, to add 50 μl of positive, negative cells or cell supernatant to the channels, respectively. Hence, a final antibody concentration of 2 nM

Tab. 5.1.: Autocorrelation fit parameters for Alexa 488 antibody within and outside of the hydrogel.

	τ_D [ms]	α
Channel	0.17 ± 0.01	
Hydrogel	0.23 ± 0.02	0.9 ± 0.1

was expected. After 3 h after cell addition, both signals, in the positive and negative control channel, leveled at a concentration of (0.6 ± 0.2) nM. A signal drop was only expected for the positive cell line at a receptor concentration of 100 nM. Hence, no specific antibody receptor binding was determinable.

5.5 | Discussion

The goal of this study was to develop a set-up allowing the characterization of ligand binding to living cells with low sample consumption. Instead of quantifying the amount of bound ligand, we aimed to measure the concentration of free ligands. The binding of ligands to cells would reduce the amount of free ligands, which we refer to as ligand depletion. The idea was to extract K_D values from titration experiments, on- and off-rates or receptor concentrations.

Therefore, two different types of set-ups had been developed to allow FCS concentration determination in a cell free area. In one set-up a membrane served as a barrier between the cell compartment and the detection volume. In the other set-up, a hydrogel hindered cells from entering the measurement area [135]. However, neither with the membrane set-up nor with the hydrogel set-up specific antibody cell binding was observable.

Up to now, it remains unclear why measurements were unsuccessful. Nonetheless, possible explanations might be found in the ligand depletion approach itself. The main drawback of this concept is that it cannot be detected where the ligand binds to. Molecules segregated from the cells themselves might affect the concentration measurement. In fact, these segregates might be autofluorescent themselves and thereby interfere the concentration determination. Although FCS antibody measurements were not affected by cell supernatant, these segregates might play a role when a high concentration of cells are added (Fig. 5.3). This possibly explains why the concentration increased instead of decreased for the cell culture insert measurements (Fig. 5.5). Furthermore, another disadvantage of this method is, that it is indistinguishable whether the antibody binds truly to the cells or to e.g. the chamber walls or segregated cell molecules instead. Additionally, it cannot be excluded that unfunctional antibodies - not capable of binding - are present in the sample. These antibodies would not be visible in flow cytometry, however, in a FCS concentration measurement, they would lower the depletion effect.

For the hydrogel, for example, the determined initial concentration was 80% lower than the added concentration (Fig. 5.6 (B)). This deviation presumably arises from unspecific binding to the hydrogel or the chamber walls (although passivating with BSA prior to measurement). Additionally, it cannot be ruled out that the residual concentration in the

end was too low to distinguish a difference between the positive and the negative cell line. Also, it needs to be elucidated whether the antibody bound unspecifically to the negative control cells and therefore lowering the unbound ligand concentration in the negative control as well.

Moreover, for the hydrogel measurements changes in the diffusional characteristics were observed when recording the autocorrelation curve within the hydrogel (Fig. 5.6 (A)). The hydrogel matrix might trap or interact with the antibodies, which might be an explanation for the anomalous diffusion observed [136, 137]. Banks et al. for example found that beads within an agarose gel showed anomalous diffusion on the short length scales measured with FCS [137]. Hence, the hydrogel set-up would only allow very small ligands to diffuse freely through the gel. Therefore, it is not recommendable to measure the FCS signal within the hydrogel if the ligands have a comparable size to the mesh size of the hydrogel. Nonetheless, it would be beneficial to further investigate creating hydrogels with larger mesh sizes, putatively with different gels. Golden et al. for example have created hydrogel networks with embedded micrometer sized channels for a selective macromolecule delivery [138]. Moreover, instead of measuring within in the gel, one could create a gel surrounding the measurement area. This would solve potential problems with anomalous diffusion and the gels would serve well as cell barriers.

Another issue are the long equilibration times which need to be solved. In fact, this is not only time consuming, but also cell processes might affect values gathered by ligand depletion. Internalization of ligands for example is a process which can be as fast as few minutes after binding or can take up to a few hours after the initial interaction [139–141]. Also, cell viability might be affected negatively when keeping cells at high concentrations for a long time. A solution here would be to decrease the sample volume further to reduce the equilibration times. For example, at our chair also Laser cutters are being tested to produce small chambers in Plexiglas. Literature for instance has reported that microliter small cavities can be created in glass by using laser ablation [142–144]. In conclusion, measuring antibody binding with the depletion of FCS signal was not successful in the scope of this study. However, tuning hydrogel mesh sizes to create larger pores or creating even smaller measurement chambers to reduce equilibration times are possible improvements for future method developments.

6 | A DNA Origami Platform to Study Multivalency

As shown in the previous chapters multivalency is an inevitable mechanism nature has evolved in order to allow biological recognition by enabling both tight binding and high specificity. Also, this concept is utilized in DNA nanotechnology to design higher order assemblies with multivalent hybridization sites [58, 145–147]. However, up to now the avidity of multiple DNA strand hybridization accompanied with both electrostatic and steric constraints has not been evaluated quantitatively. In the following, I will present a multivalent tool aiming to design a well defined and adaptable model system with tunable individual binding strength as a function of complementary sequence length [43, 44, 148]. Additionally, DNA as a framework allows to define nanometer precise receptor and ligand distances [57]. With both, the control of arrangement and K_D value, we seek to thoroughly characterize effects of linker flexibility, concentration enhancements and valency on avidity. The model system described below allows up to four simultaneous binding events with adaptable individual binding strengths, its rigidity is tunable by varying the length of single stranded and double stranded parts and last but not least, linker distances as well as receptor placements are straightforward adjustable (s. Fig. 6.1). The avidity effect was studied with multiple different methods, such as FCS, MST and EMSA. Data presented below is adapted from the Manuscript [M2].

6.1 | Characterization of the Model System

A schematic illustration of the model system is shown in Fig. 6.1. Here, a rectangular one-layer DNA origami with up to four protruding handles with different sequences at a distance of 20 nm served as a tetravalent receptor (exact design is shown in App. Fig. A.5). Three ligands which can bind to the receptor have been designed: 1) a monovalent ligand which has only one single stranded targeting sequence at one end which is complementary

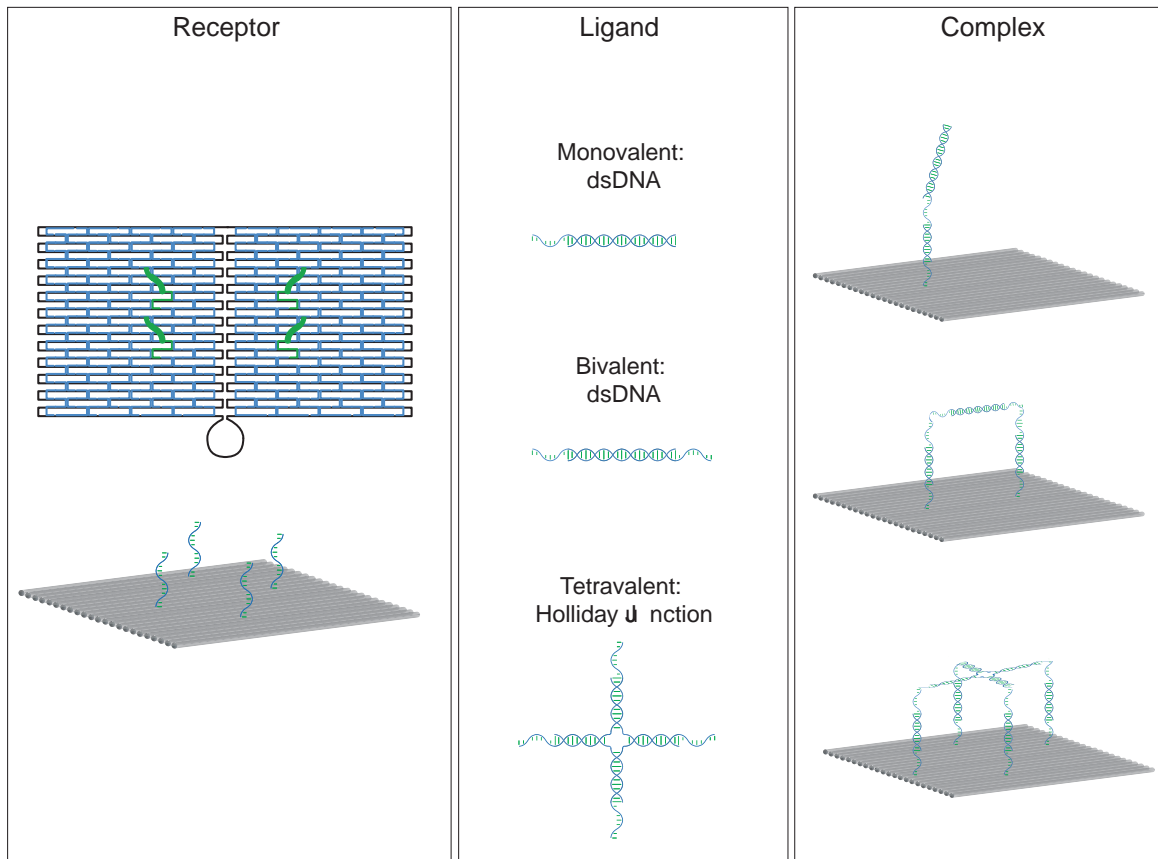


Fig. 6.1.: Schematic illustration of the multivalency model system. Receptor: Rectangular one-layer DNA origami with up to four protruding handle strands at a distance of 20 nm. Monovalent Ligand: dsDNA with one single stranded target sequence. Bivalent Ligand: dsDNA with two single stranded target sequences at the 3' and 5' end 20 nm apart. Tetravalent Ligand: Holliday Junction with four single stranded targeting sequences. Monovalent complex: single stranded target sequence binds to protruding handle on DNA origami. Bivalent complex: both target sequences of the bivalent ligand bind to two handles on the DNA origami. Tetravalent complex: all four targeting sequences of the Holliday Junction hybridize to the four handles on the DNA origami.

to one handle on the DNA origami. 2) a bivalent ligand, where on both, the 5' and the 3' end, a single stranded targeting sequence can hybridize to two handles on the receptor. 3) a tetravalent ligand consisting of a Holliday Junction (HJ) with four single stranded targeting sequences capable of binding to all four handle sequences of the DNA origami. In order to allow bending of the ligand once bound to one handle, each targeting sequence also contained a spacer of 10 nt. The monovalent control ligands consist of the same linker (dsDNA for the bivalent system or HJ body for the tetravalent system), but contain only one targeting sequence.

6.1.1 | Bivalent Ligand

Prior to detailed binding studies, first the functionality of the model system was thoroughly characterized. Correct folding as well as binding of ligand and receptor were investigated with AFM, EMSA and FCS (Fig. 6.2). The mono- and the bivalent ligand consist of two single stranded DNA sequence with a 59 bp long complementary part resulting in a linker length of 20 nm. Strand 1 (S1) also contained an Atto 655 fluorophore for fluorescent binding measurements. These ssDNA strands were mixed in a 1:1 ratio and annealed in a 2h temperature ramp. In order to test whether these strands had correctly hybridized, EMSA was used (s. Fig. 6.2 (A)). For the hybridized duplex (D) an upward shift in the gel was observable. Due to the mass and size increase, when both strands are connected, the migration velocity in the agarose matrix is reduced and the duplex runs slower than the single strands. Also, no further bands were detectable in the duplex lane, confirming that strand 1 and 3 have correctly folded. Next, the folding of the DNA origami and the binding of the duplex to its handles was studied. The AFM image in Fig. 6.2 (B) depicts the rectangular sheets, which verified that staples and scaffold have annealed properly. Also, the DNA strands of the bivalent ligand were visible on top of the rectangular sheets confirming that ligand and receptor form a complex. The same result has also been obtained when studying the diffusion of the bivalent ligand alone and after addition of the DNA origami receptor with FCS, which is depicted in Fig. 6.2 (C). A right shift of the autocorrelation curve was observable, when DNA origami was added to the solution. Once the fluorescently labelled duplex is bound to the DNA origami, its diffusion coefficient is reduced from $(47 \pm 5) \mu\text{m}^2 \text{s}^{-1}$ to $(7 \pm 4) \mu\text{m}^2 \text{s}^{-1}$ determined by fitting with a two component model (Eq. 3.16). Studying the diffusional shift over time allowed to characterize the hybridization kinetics of ligand receptor binding (Fig. 6.2 (D)). Here, the change in fraction hybridized is shown as a function of time, which was fitted with Eq. 2.25 resulting in an on-rate $k_{on} = 6 \cdot 10^6 \pm 2 \cdot 10^6 (M \cdot s)^{-1}$. Interestingly, the hybridized fraction did not saturate at 1, but at 0.7, implying that 30% of the fluorescently labelled ligands did not bind to the DNA origami.

6.1.2 | Tetravalent Ligand

Concerning the tetravalent ligand (Holli), the characterization is shown in Figure 6.3. Holli consists of up to 8 hybridized strands. The body (a Holliday Junction) is formed by

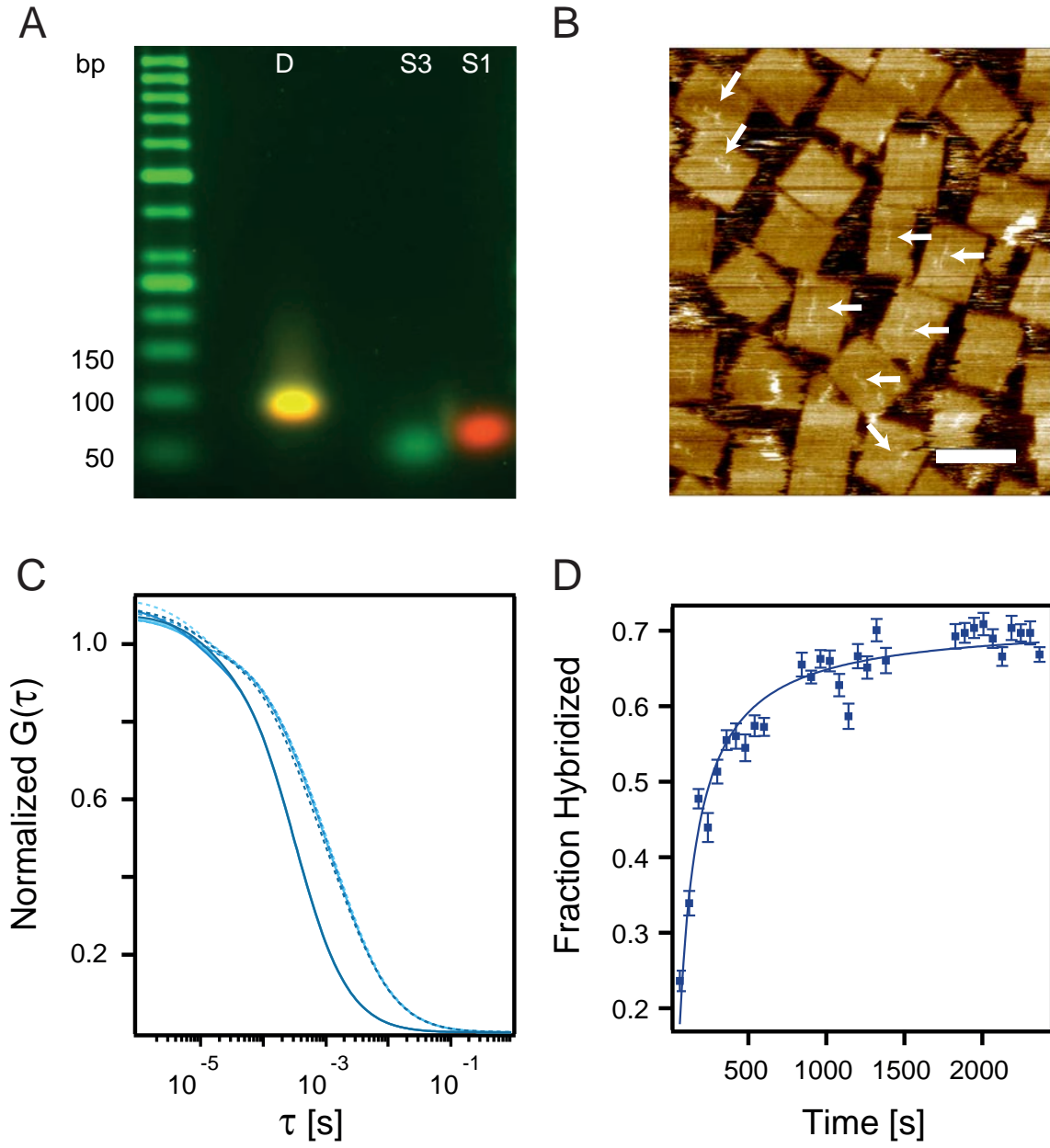


Fig. 6.2.: Bivalent model system characterization. (A) EMSA assay showing the migration difference of single stranded target strands S1 and S3 and the hybridized duplex (D). Red channel shows fluorescence of Atto 655 dye on S1. Green channel depicts signal of Sybr Green staining. (B) AFM image of DNA origami receptors with bound ligand marked with arrows. Scale bar 100 nm, color scale from dark to bright: 0 nm to 8.9 nm. (C) FCS curves for bivalent ligand (solid lines) and after hybridizing to DNA origami (dashed lines). (D) Fraction of bivalent ligand bound as a function of time. Fit Eq. 2.25: $k_{on} = 6 \cdot 10^6 \pm 2 \cdot 10^6 (M \cdot sec)^{-1}$.

four 60 nt long DNA strands (H1-H4), where each arm contained a 20 bp long complementary sequence for one target strand (T1-T4), respectively. Each target strand is 50 nt long consisting of the 20 nt individual complementary sequences, a 10 nt spacer for bending and a 20 nt individual target sequence. These target sequences can uniquely bind to a handle of a length between 8 and 20 nt on the DNA origami. EMSA showed how the different strands hybridized after the 2 h annealing process (Fig. 6.3 (A)). Here, H1 is complementary to H2 and H4, whereas H3 is complementary to H2 and H4, respectively. A clear band shift was observable when complementary strands were mixed in a 1:1 ratio and annealed. However, faint lower bands were also detectable, implying that uncomplexed or not fully functional Holliday Junctions were present in the sample and these sample impurities necessitate further purification steps. Hence, prior to measurements the annealed structures were purified in an agarose gel, where the highest band was cut out and the sample recovered (s. App. Fig. A.6). After purification two methods were applied to study the multivalency effect of the tetravalent Holli. In Fig. 6.3 (B) an exchange PAINT test visualizes how the tetravalent ligand (red) binds to the DNA origami. First, TIRF movies were recorded with the imager binding to the handles on the DNA origami (Cy3b). Next, the Holliday Junction was added and hybridization was checked with an imager binding to possibly all four arms of Holli (Atto647N). This allowed us to tackle how does handle accessibility effect binding and furthermore, is the tetravalent ligand able to bind with all four arms? On this representative image three handle sites are visible and were colocalized with only one arm of the Holliday junction. While accessibility had been studied before by Strauss et al. revealing an efficiency from roughly 60 - 90 % for single handles on the DNA origami, having in total four possible binding sites should result in an almost 100 % colocalization rate [149]. However, data analysis showed that only 80 % of the DNA origami had Holli attached. Additionally, it was observable that in only 30 % of the cases Holli bound with more than one arm to the DNA origami, which might hint towards bad sample integrity or electrostatic repulsion (s. Chapter 6.3). Also, FCS data showed that Holli bound to the DNA origami (s. 6.3 (C) and (D)). A clear right shift in diffusion time and resulting reduction in diffusion coefficients from $D = (57 \pm 5) \mu\text{m}^2 \text{s}^{-1}$ to $D = (6 \pm 3) \mu\text{m}^2 \text{s}^{-1}$ was observable when the DNA origami was added. However, this shift was less for the monovalent compared to the tetravalent ligand (one arm versus four arms). When characterizing the bound fraction for different DNA origami concentrations, the fraction of the monovalent was reduced by around 20% compared to the tetravalent ligand. However, both curves did not reach a maximal bound fraction of 100 %. Also, the steepness of both curves deviates significantly from the expected shape for an estimated $K_D = 1 \text{ pM}$ for a 16 bp binding (dashed line),

which might result from electrostatic repulsion (s. Chapter 6.3).

6.2 | Characterization of Monovalent vs Bivalent Binding

As the results for the tetravalent ligand showed deviations from the expected behavior, which implies that other effects like sample integrity or electrostatic repulsion might interfere with the binding process, I decided to characterize first the binding of the monovalent and the bivalent ligand. For different length of the complementary sequence hybridization was studied with FCS for the DNA duplex with one or two arms (s. Fig. 6.4 (A)-(D)). For all complementary sequences a clear distinction between mono- and bivalent binding was observable. This deviation, however, was reduced towards stronger binding (11 bp and 12 bp). A clear left shift of both green and blue curves were well detectable when comparing the fraction bound curve for 9 bp and 10 bp, hinting towards an avidity effect. While for the monovalent binder hardly any hybridized fraction was determinable, a full fraction bound curve was measureable for the bivalent 10 bp binding. Next, the normalized fraction bound data was fitted with the general binding isotherm (Eq. 2.9). All determined K_D values were plotted as a function of binding site base pairs in Fig. 6.4 (F). Also, the theoretical expected K_D values calculated with MFold are shown as grey data points [45]. While the monovalent K_D data lay above these theoretical expectations, smaller K_D values were only determinable for the 9bp and 10 bp bivalent binding. Moreover, for the 11 bp and 12 bp bivalent interaction the acquired K_D values seemed to saturate and a lower binding strength was observable compared to theoretical predictions. This trend originates from a phenomenon that is referred to as sensitivity saturation in this thesis. To illustrate this problem, I plotted various binding isotherm from 0.1 nM to 0.001 nM for a constant ligand concentration of 0.5 nM (s. Fig. 6.4 (E)). While the curves for 0.1 nM and 0.01 nM are still distinguishable, for stronger binding these curves more and more equalize and become indistinguishable. Unless one cannot reduce the amount of ligand (due to sensitivity of the method), the gathered K_D values will saturate at approximately one tenth of the ligand concentration applied. Also, using MST did not allow to determine K_D values below 0.1 nM (s. App. Fig. A.7). Taken together, for the bivalent ligand with a 10 bp long complementary sequence a clear shift towards stronger binding was observable compared to the monovalent ligand. However, for shorter or longer complementary sequences the methods applied in this thesis did not allow the determination of reliable K_D values.

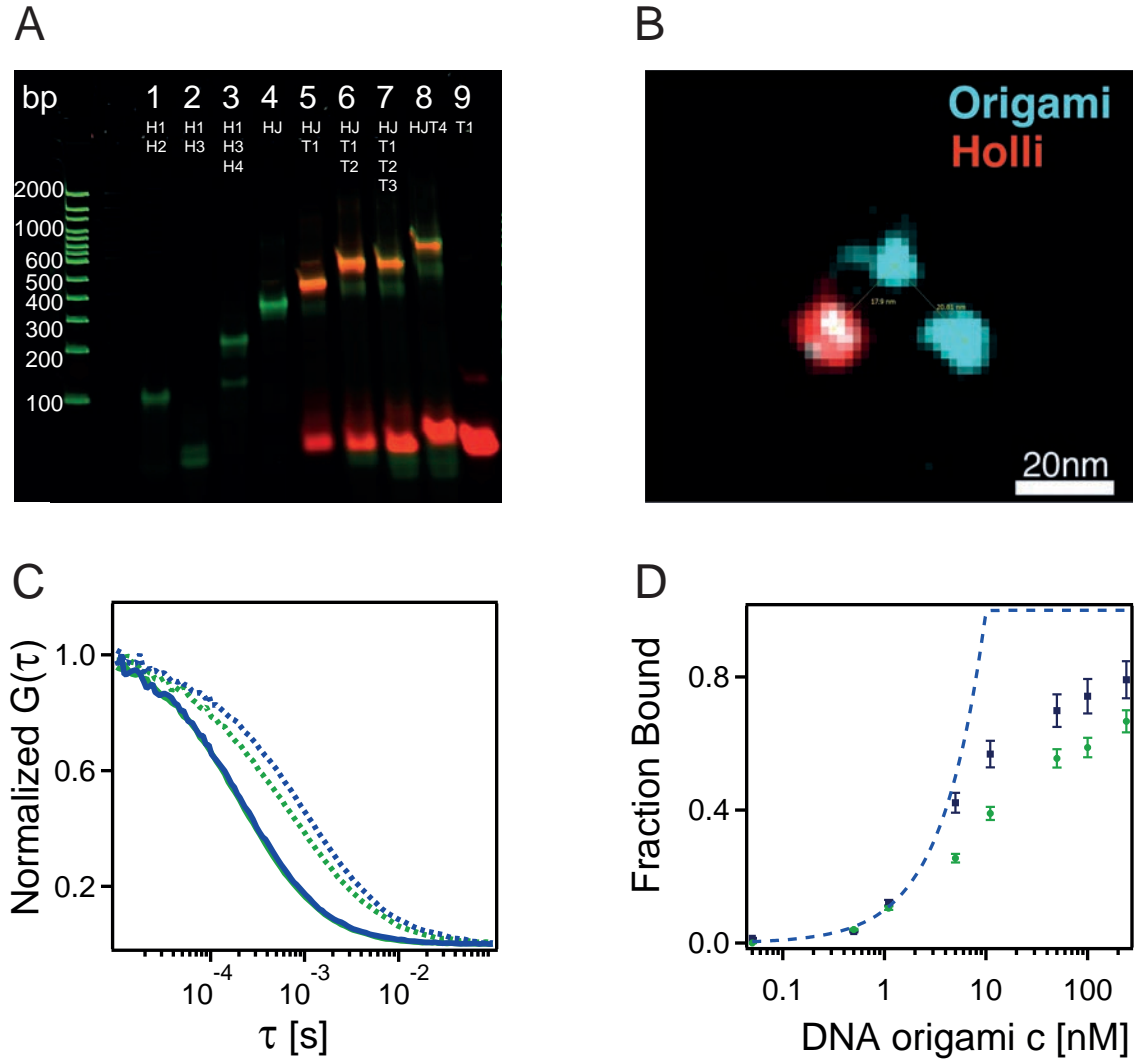


Fig. 6.3.: Characterization of the tetravalent model system. (A) Composite of red (Atto 655) and green (Sybr Green staining) channel of an EMSA image depicting folding of the tetravalent Holliday Junction (HJ). Bands show result after annealing of different components: HJ body strand H1-H4, where H1 is complementary to parts of H2 and H4, but not to H3; target strands T1-T4 complementary to only one HJ body strand indicated by the number, where T1 is labelled with Atto 655. (B) Composite PAINT image of Tetravalent Holliday Junction binding to DNA origami, verified with two different imager strands hybridizing either to handle (blue) or target strand (red), respectively. (C) FCS curves for tetravalent (blue) or monovalent (green) HJ alone (solid line) or bound to DNA origami (dashed line). (D) Fraction of HJ bound as a function of DNA origami concentration for monovalent (green) or tetravalent (blue) binding. Fit with $K_D = 1$ pM.

6.3 | Discussion

This study aimed to create an adaptable, well defined multivalency model system with predictable K_D values. By choosing DNA as a framework nanometer precise receptor and ligand distances could be guaranteed [57]. Additionally, by varying the complementary sequence length, predictions on the binding strength could be made, which has been extensively studied and modeled in literature [43, 44, 148]. Likewise, a compelling benefit over methods such as protein engineering is the straight forward designing. Many different companies provide DNA services with up to 100 bp synthesis. Also, scaffold DNA for the DNA origami can be bought online (s. Chapter B.2). Moreover, DNA nanotechnology had already proven to provide tools for the study of multivalency. Rinker et al. for example created a multihelical DNA origami with distinct aptamer placement for thrombin binding. Here, EMSA and AFM studies showed that dual-aptamer placement increased protein binding tenfold [150]. Another interesting multivalency study with DNA origami had been performed by Shaw et al., where they could provide evidence that the spatial organization of ephrin ligands altered EphA2 receptor phosphorylations and cell invasiveness [151]. However, here in this thesis a model system was created with even more adaptivity, programmability, controllability and simplicity. Instead, of using proteins or other macromolecules possibly introducing artefacts, the model system presented solely consist of DNA. Concerning the ligands EMSA assays revealed that the mono- and bivalent ligand hybridized well and no further purification was necessary (s. Fig. 6.2 (A)). For the tetravalent ligand containing up to eight strands, however, unfolded structures or DNA strands were observable requiring agarose purification (s. Fig. 6.3 (A)). Here, instead of a 59 bp complementary sequence for the mono- and bivalent ligand, the strands of the Holliday Junction fold with 20 bp complementary sequences. This concept of using multiple strands to form the tetravalent ligand allows flexibility in ligand distance and sequence length, but it also makes the system more complex and less controllable. Hence, for further tests it is advisable to design a Holiday Junction consisting of only four DNA strands to simplify the system. Similar tools have actually been developed throughout this study in the group of Smith [152]. For example, they used a Holliday Junction to study crosslinking of actin networks or EphA2 phosphorylation by SWL peptide multivalency, respectively [152, 153].

For the DNA origami receptor well established protocols exist and AFM (s. Fig. 6.2 B) as well as EMSA verified correct folding [154]. Further, the binding of the ligand towards the receptor was confirmed with multiple methods such as FCS, MST, EMSA, DNA PAINT and AFM (s. Fig. 6.2 and Fig. 6.3 (B) & (C) and App. Fig. A.7). Additionally, when

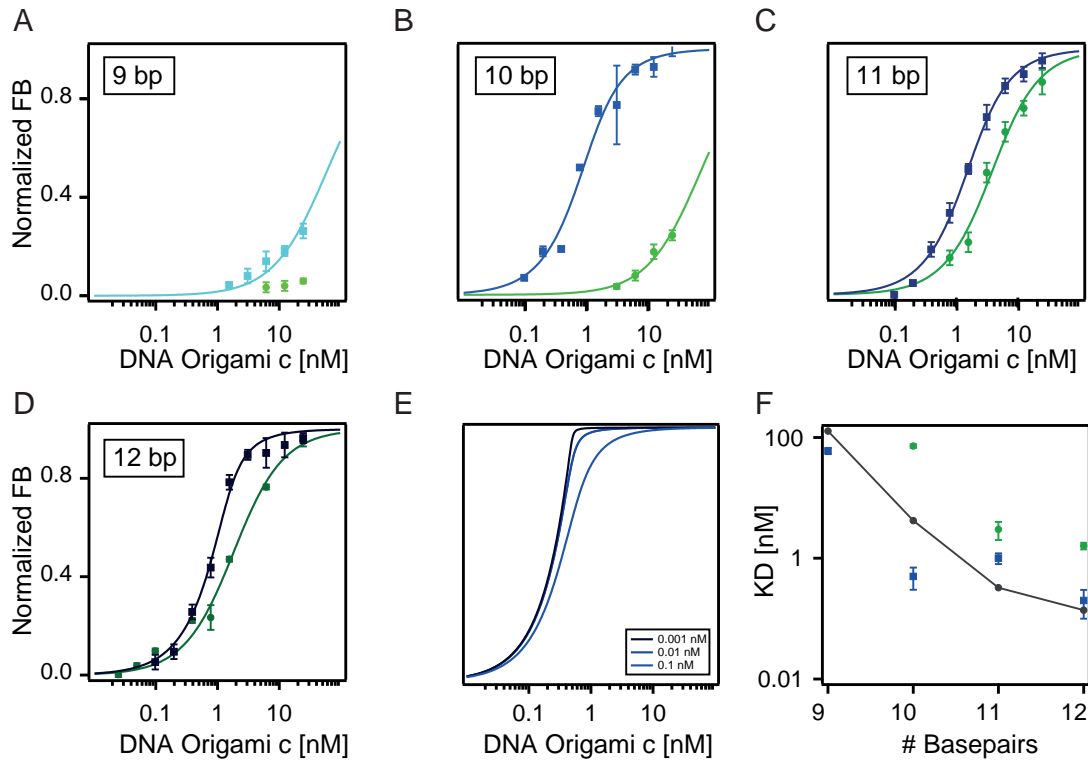


Fig. 6.4.: Avidity as a function of basepairing. (A) - (D) Normalized fraction bound over DNA origami concentration for the mono (green circles) or bivalent (blue squares) ligand for different length of complementary sequence: (A) 9 bp, (B) 10 bp, (C) 11 bp and (D) 12 bp. (E) Theoretical fraction bound curve for different K_D values from 0.1 nM to 0.001 nM (light to dark blue). (F) K_D values as a function of basepairing for mono (green circles) and bivalent (blue squares) hybridization. Grey values depict theoretical values calculated with Mfold [45].

characterizing the hybridization times with FCS an on-rate of $k_{on} = 6 \cdot 10^6 \pm 2 \cdot 10^6 (M \cdot sec)^{-1}$ which is in line with values stated in literature [155]. Interestingly, however, in all FCS binding studies the fraction of bound species saturated at levels between 70 - 90 %, which can only be rationalized with ligands with corrupt target strands or ligands lacking fluorescent labelling. The former would, especially for the monovalent ligand, appear as a species which does not bind even at high receptor concentrations. The latter would result in a competitor species, which binds instead of the labelled ligands. IDT for example guarantees a sample purity of 75-85 %, which would result in an unlabeled competitor fraction of up to 25%. Nevertheless, normalizing the fraction bound curves to the plateau values allowed the determination of K_D values as a function of basepairing length (s.

Fig. 6.4 (A)-(D)). For each length the bivalent ligand bound stronger compared to the monovalent ligand. But, the K_D values saturated at 0.5 nM from a 11 bp hybridization length onwards. As mentioned above this is explainable with sensitivity saturation.

Depending on the sensitivity of the method applied a certain concentration of ligand is necessary to circumvent noise problems. The ligand concentration, in return, also determines the lowest K_D value quantifiable, since the curves become indistinguishable for K_D values lower than approximately one tenth of the applied ligand concentration (s. Fig. 6.4 (E)). This also explains the fact that theoretical estimated K_D values for a monovalent hybridization was lower than the measured bivalent hybridization for 11 and 12 bp binding (s. Fig. 6.4 (F)). In fact, this is also observable for monovalent hybridization studies in literature. Here, a MST study for example reports for a 16 mer hybridization a $K_D = 0.2$ nM, theory however would predict a K_D value in the femtomolar region [156]. Similarly, Xu et al. determined for a 20 bp DNA a $K_D = 0.3$ nM clearly underestimating the binding strength [157].

However, not only the sensitivity saturation plays a crucial role in the determination of a multivalency effect. In the following, I will therefore discuss other effects enhancing or reducing the K_D change from monovalent to bivalent binding theoretically (Fig. 6.5). Here, I adopt the theory described in the group of Knapp and Netz (s. Chapter 2)[34–36]: The dissociation constant for a bivalent molecule with an individual dissociation constant K_{mono} can be described by:

$$K_{D,bv} = \frac{K_{mono}^2}{\exp(\frac{\Delta G}{k_B T}) 2\pi c_{eff}} \quad (6.1)$$

Therefore, two main effects play a substantial role in the bivalency effect: the effective concentration c_{eff} and an energetical term $\exp(\frac{\Delta G}{k_B T})$ accounting for steric hindrance or electrostatic repulsion.

First, the critical influence of the effective concentration will be described as a function of receptor distance d and depends on the length of the ligand linker r and its flexibility denoted by Δr .

$$c_{eff}(d) = \frac{1}{2(2\pi)^{3/2}} \frac{\exp(-1/2 \frac{(d-r)^2}{\Delta r^2})}{\Delta r r^2} \quad (6.2)$$

This dependence is shown in Fig. 6.5 (B). Especially, when the receptor distances are in the regime of few tens of nanometer (bivalent ligand : 20 nm dashed line) flexibility substantially effects the effective concentration (up to 3 orders of magnitude). In return, the larger the effective concentration the lower the bivalent K_D , which is depicted in Fig. 6.5 (C). Here, Eq. 6.1 was simplified by neglecting the energy term. Therefore, assuming

a monovalent $K_D = 100$ nM (dashed line, e.g. 10 bp hybridization of the monovalent DNA

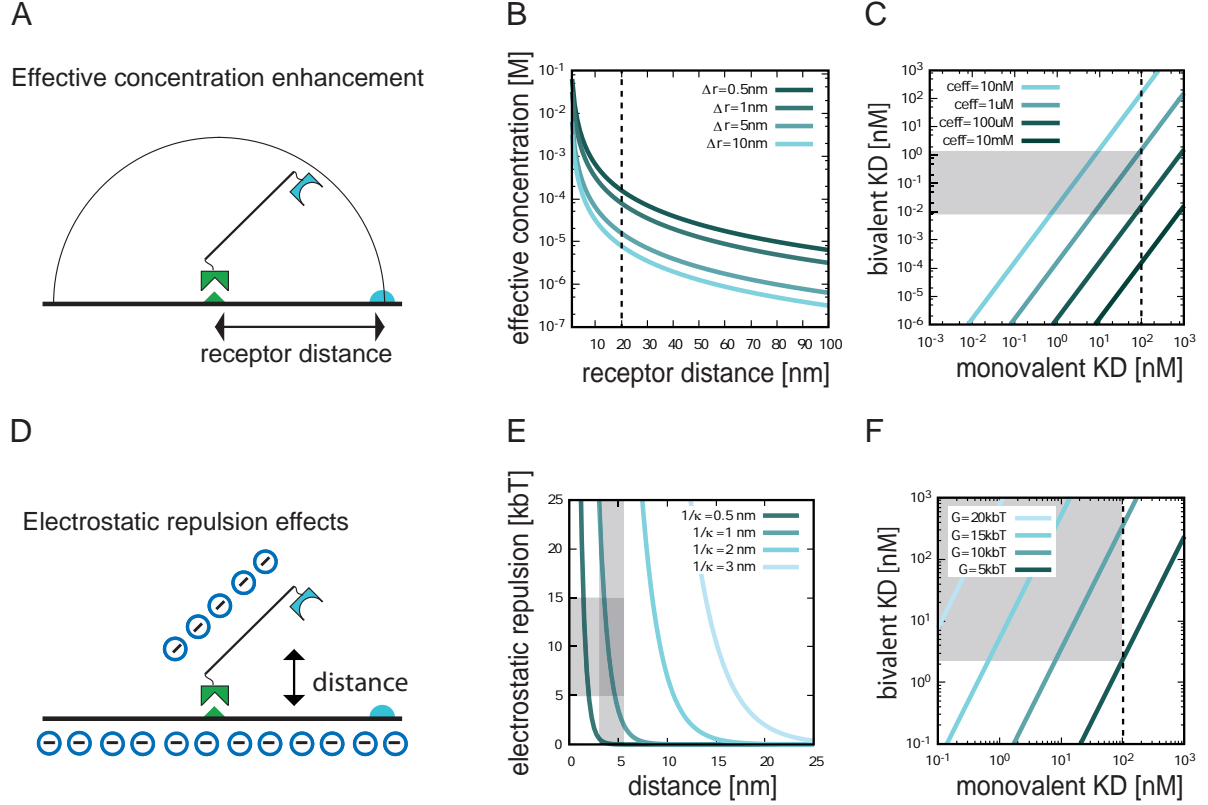


Fig. 6.5.: Theoretical estimation of bivalent hybridization. (A) Schematic illustration of the concentration enhancement due to bivalency. (B) Effective concentration as a function of receptor distance for different flexibility lengths from 0.5 nm to 10 nm (dark to light blue). (C) Estimation of bivalent K_D over monovalent K_D for different values for the effective concentration from 10 nM to 10 mM (light to dark blue). The shaded area highlights the range of predicted values for the bivalent model system. (D) Schematic illustration of electrostatic repulsion of ligand and DNA origami. (E) Change in electrostatic repulsion with distance for different Debye screening lengths κ^{-1} from 0.5 nm to 3 nm (dark to light blue). The shaded area highlights the uncertainty in values for the bivalent model system. (F) Bivalent K_D as a function of monovalent K_D for different values for the electrostatic repulsion G from 5 to 20 $k_B T$ (dark to light blue). The shaded area highlights the expected values for the bivalent model system. Dashed lines refer to the monovalent K_D .

ligand) three orders of magnitudes in the effective concentration result in 10 orders of magnitude for the bivalent K_D . When estimating the influence of the effective concentration on the K_D value for the bivalent ligand, a flexibility of $\Delta r = 1$ nm, a monovalent $K_D(mono) = 100$ nM, a ligand linker length $r = 100$ nm and a receptor distance of $d = 20$ nm (perfect match) were presumed. These assumptions yield a bi-

valent $K_{D,bv} = 20$ pM, which deviates in one order of magnitude from the measured $K_{D,bv,m} = (500 \pm 200)$ pM. However, as the grey area visualizes, the uncertainties arising from the flexibility of the rod and its impact on the effective concentration did not allow for an exact estimation.

Moreover, up to now the energy term has not been taken into account. Since both, the ligand (DNA) and the receptor (DNA origami) are negatively charged, presumably the contribution of electrostatics is not negligible. The potential of the DNA origami ligand complex can be estimated by [158]:

$$\Phi_{plane}(z)[k_B T] = \frac{4\pi \cdot l_B \cdot r \kappa^{-1}}{S \cdot b} \cdot \exp(-\kappa z) \quad (6.3)$$

where the Bjerrum length of water is $l_B = 0.7$ nm and the Debye screening length $\kappa^{-1} = 1.1$ nm [159]. $S = 0.9$ nm² denotes the area per elementary charge of the DNA origami and $b = 0.34/2 = 1.7$ nm the distance per elementary charge as suggested by literature [160]. The ligand is assessed as a charged rod of the length $r = 0.34 \frac{nm}{bp} \cdot 59bp = 20$ nm. The electrostatic repulsion as a function of distance is shown in Fig. 6.5 (E). The effect of the energy term on the bivalent affinity is plotted in Fig 6.5 (F). Taking these numbers into account and assuming a distance $z = 0.34 \frac{nm}{bp} \cdot 16bp = 5.4$ nm, the energy term can be estimated to $E = 8k_B T$. Now, this in return would result in a bivalent dissociation constant of $K_{D,bv} = 68$ nM, which overestimates the measured $K_{D,bv,m} = (500 \pm 200)$ pM by two orders of magnitude. This deviation might result from an overestimation of the electrostatic term. For example, the effect of charged ions within the buffer have not been taken into account apart from the Debye screening length. The negatively charged DNA will accumulate positively charged counterions and will reduce the concentration of negatively charged ions in its vicinity [161]. Hence, the electrostatic repulsion is shielded and thereby the energetical term might be significantly lower than assumed above. In the review by Lipfert et al., for instance, they state that 150 mM of a monovalent salt will reduce the repulsion roughly 10-fold. Furthermore, they argue that divalent metal ions such as Magnesium decrease the electrostatic effect even further [161]. Nonetheless, electrostatic repulsion cannot be neglected, which might also explain the fact that the K_D values for the monovalent ligand deviates by around 40% from the theoretical predicted values obtained with Mfold [45]. Hence, for future research it might be beneficial to include simulation data to achieve a better estimation of the effect of electrostatic repulsion.

Taken together, purely accounting for the effective concentration enhancement overestimates the bivalency effect and therefore, the energetic term is not negligible and clearly lowers the expected bivalent K_D value. Hence, with both the energetic term and the

concentration effect an upper and a lower boundary can be approximated, which frame the measured dissociation constant from $K_{D,bv} = 0.02 \text{ nM}$ to 68 nM . Actually, when scanning multivalency studies of other biological samples, often low avidity effects are stated. Concerning for example the thrombin binding study mentioned earlier by Rinker et al. only a tenfold enhancement from 100 nM to 10 nM was found [150]. Also, Karush et al. determined only a 30-fold affinity enhancement for a bivalent antibody binding to a surface antigen on *Bacillus sp.* compared to the monovalent antibody [13]. Nevertheless, there are also examples where significant avidity enhancements had been identified. In the examination by Mack et al. they investigate the effect of linker length on avidity. Here, they synthesized bivalent sulfonamide ligands with different lengths and achieved an enhancement from 16 nM for the monovalent to 3 pM for the bivalent ligand [162]. These discrepancies in literature make clear that the model system itself as well as the chosen methods have an enormous effect on the outcome of a multivalency study.

Here in this investigation, indeed avidity enhancements were observable for the monovalent and bivalent ligand, however, it is obvious that the methods chosen did not allow a reliable determination of both the mono- and the bivalent K_D at the same time. Instead, it became clear throughout this study, that methods, where the off-rate rather than the K_D value is determined, is favorable. Multivalency dominantly affects the off-rate due to rebinding effects [26]. Therefore, for further experiments non-equilibrium methods such as DNA PAINT, Surface Plasmon Resonance (SPR) or isothermal titration calorimetry (ITC) would be beneficial [59, 163].

7 | VWF DNA Binding

Another multivalent binding interaction which is affected by electrostatics is described in the following. As described in Chapter 2.3.2 VWF interacts with many different cells in the bloodstream to induce, for example, blood coagulation. It is yet unclear how VWF interacts in pathogen elimination. Here, it is presumed that VWF binds to DNA of neutrophil extracellular traps (NETs). By binding similarly to collagen on the blood vessel walls and to DNA, VWF is assumed to aid immobilizing these NETs [68]. However, the molecular mechanisms of VWF-DNA interaction remain unclear. Already in a previous study an electrostatic influence of DNA binding to VWF had been suggested [23]. Here, they showed that by neutralizing the negative charges on DNA with polycationic chitosan VWF binding was blocked. In their study, however, they could only demonstrate VWF DNA binding in presence of the antibiotic Ristocetin and up to now it remains unclear which molecular effect Ristocetin has on VWF or DNA. Hence, they could neither quantify binding without Ristocetin nor could they estimate the effect of electrostatics on VWF DNA binding. In the following chapter, VWF-DNA interaction will therefore be characterized without Ristocetin. Experimental results presented below suggest that the A1 domain of VWF acts as the main binding region. Furthermore, I will discuss how electrostatics govern the binding interaction of the A1 domain, as well as full-length VWF, to DNA. Also, the effect of shear and DNA sequence will be described below. Results shown in the following are adapted from the Publication [P2].

7.1 | Electrostatics Influence A1 Domain DNA Interaction

Up to now it remains an open question how electrostatics affect VWF-DNA binding. To this end, using BD and MD simulations my collaboration partners Sandoval-Perez and Aponte-Santamaria systematically investigated effects of molecule charge and ion solution. In the simulation data it became obvious that DNA mainly interacts with the triad of

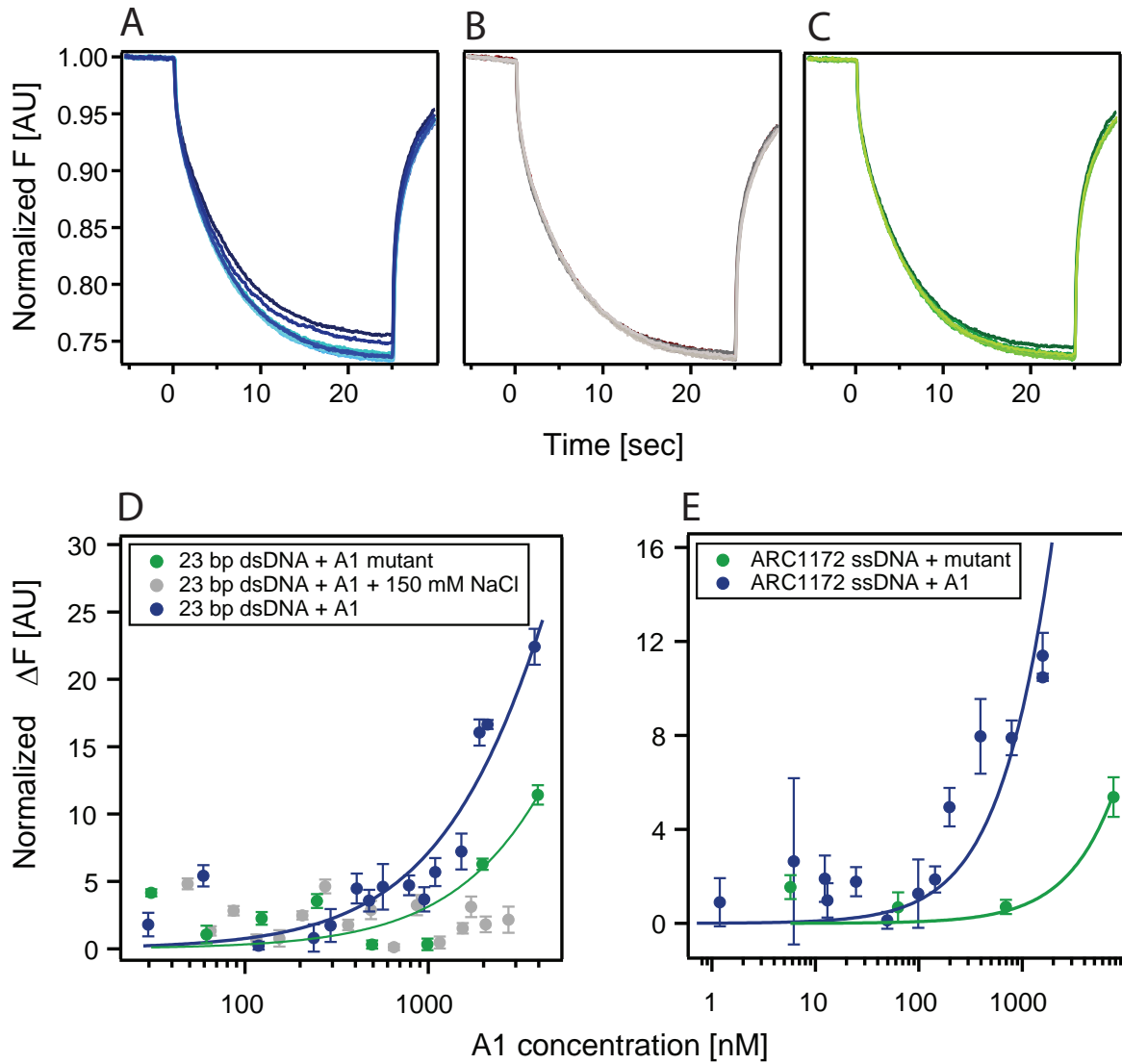


Fig. 7.1.: Electrostatics influence the A1 domain DNA interaction. Thermophoresis response curves for titrations of dsDNA binding to (A) wt A1 domain in PBS buffer (blue), (B) the wt A1 domain in PBS with additional 150 mM NaCl (grey) and (C) the A1 domain with mutations R1392A, R1395A and R1399A (green). Titration from high concentration (dark curves) to low concentration (bright curves). (D) Change in normalized fluorescence (ΔF) for 23 bp dsDNA and the A1 domain in PBS (blue) with $K_D = (13 \pm 1) \mu\text{M}$, the A1 domain with mutations R1392A, R1395A and R1399A (green) with $K_D = (30 \pm 6) \mu\text{M}$ and the A1 domain in PBS with additional 150 mM NaCl (grey). (E) Change in normalized fluorescence (ΔF) for ARC1172 ssDNA and the A1 domain in PBS (blue) with $K_D = (10 \pm 2) \mu\text{M}$ and the A1 domain with mutations R1392A, R1395A and R1399A (green) with $K_D = (130 \pm 7) \mu\text{M}$. Average \pm Standard deviation ($N = 4$).

arginines at the H4 region of the A1 domain (s. Chapter 2.3.2). Mutating these arginines with alanines in the BD simulations resulted in a significant reduction of interaction times with the dsDNA compared to the wt A1 domain. Also, changing the salt concentration had an effect on the interaction energy in simulations.

Hence, to test the model predictions experimentally MST binding measurements were conducted solely with the A1 domain and DNA, but without Ristocetin. In detail, the binding of a random 23 bp dsDNA and 42 nt ARC1172 ssDNA to recombinant A1 domain depicted in Figure 7.1 was investigated. Detailed experimental sample and method descriptions can be found in Appendix B and Chapter 3.2, respectively. For the wt A1 domain titration series, an upward shift of the normalized thermophoresis response curves was observable (Figure 7.1 (A)). This change in normalized fluorescence is plotted in Figure 7.1 (D) and was batch fitted with the general binding isotherm (Eq. 2.9) to determine the dissociation constant. For the 23 bp DNA binding to the A1 domain in PBS a $K_D = (13 \pm 1) \mu\text{M}$ was estimated. However, when 150 mM NaCl was added to PBS no binding was observable (Figure 7.1 (B)). Similar to the *in silico* results a smaller thermophoresis shift compared to the wt A1 domain was detectable when the negatively charged arginines were replaced by charge neutral alanines, in the following referred to as mutant A1 domain (Figure 7.1 (C)). Fitting the data, yielded an even higher dissociation constant of $K_D = (30 \pm 6) \mu\text{M}$. This effect was even more obvious when comparing the binding of the ARC1172 ssDNA to wt versus mutant A1 domain, respectively (Fig. 7.1 E). While the ssDNA bound to the wt A1 domain with $K_D = (10 \pm 2) \mu\text{M}$, for the mutant A1 domain the dissociation constant was estimated to $K_D = (130 \pm 7) \mu\text{M}$. Hence, both results confirm that the electrostatic interactions of the arginines in the A1 domain dominantly affect binding to dsDNA as well as ssDNA.

7.2 | VWF DNA Binding is Conformation Dependent

To characterize binding in physiologically more relevant conditions in the following the full-length VWF was tested and the effects of shear on binding was studied. Therefore, I used a FCS setup equipped with a shear cell as described by Lippok et al., which enables FCS measurements directly after the sample was sheared with a constant flow in a Couette-type flow chamber [69, 164]. When VWF binds to DNA, the hydrodynamic radius increases and the diffusion time of the complex gets larger, which is observable as a right shift of the autocorrelation function (s. Chapter 3.1). Therefore, by characterizing

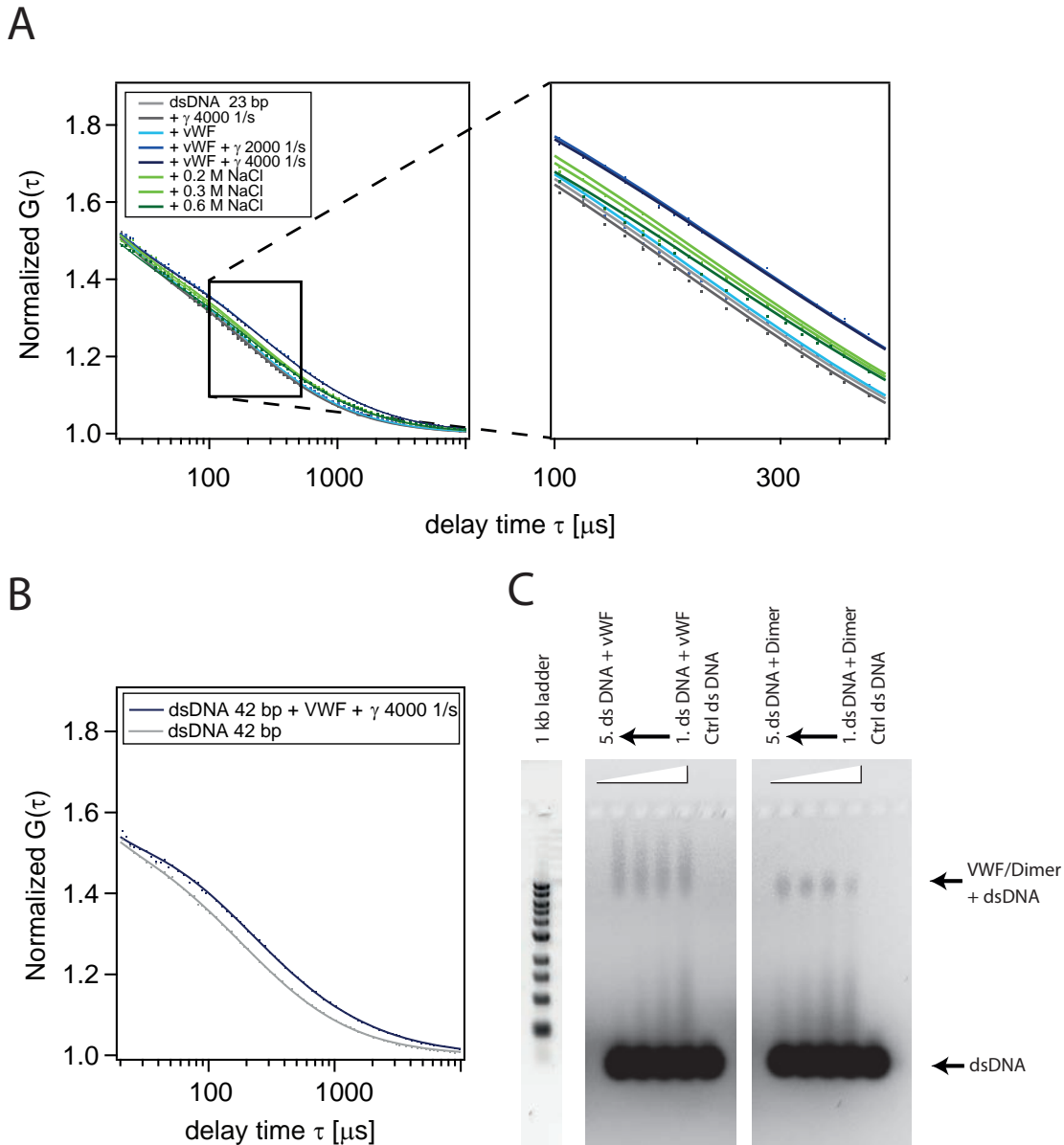


Fig. 7.2.: VWF multimer binding to dsDNA is shear-stress sensitive and sequence independent. Normalized FCS autocorrelation curves $G(\tau)$ for 23 bp (A) dsDNA alone (light grey), after shearing (dark grey), after addition of VWF (light blue) and after shearing at different rates indicated in the legend (dark blue). Green curves show effect on binding after addition of different salt concentrations: 0.2 M (light green), 0.4 M (green) and 0.6 M (dark green). (B) Change in normalized autocorrelation curves for ARC1172 42 bp dsDNA (grey) after VWF multimer addition and shearing (dark blue) with rates indicated in the legend. (C) EMSA for ARC1172 dsDNA ($c = 300$ nM) binding to different concentrations of full-length wt VWF ($130 \mu\text{g ml}^{-1}$ (1.) to $4 \mu\text{g ml}^{-1}$ (5.)) or full-length Dimer ($313 \mu\text{g ml}^{-1}$ (1.) to $10 \mu\text{g ml}^{-1}$ (5.)). Ctrl dsDNA only contains 300 nM Cy5 labelled DNA. For visualization purposes the upper sections of (D) and (E) were contrast enhanced.

the diffusion time of the labelled 23 bp (Figure 7.2 (A)) or the 42 bp dsDNA (Figure 7.2 (B)) with or without VWF allows to draw conclusions on binding. For the 23 bp DNA a diffusion time of $(197 \pm 5) \mu\text{s}$ was determined, which corresponds to a diffusion coefficient of $(80 \pm 10) \mu\text{m}^2 \text{s}^{-1}$. Neither applying a shear force to DNA alone nor VWF addition without shearing introduced any change in the FCS autocorrelation curve (Figure 7.2 (A) grey and light blue curves). However, shearing with a rate of 2000 1/s and 4000 1/s after VWF addition resulted in a right shift of the autocorrelation curves, respectively. When fitting the autocorrelation functions with two component models a fraction of $(22 \pm 2) \%$ of DNA were identified in the bound state with a diffusion time of $(0.9 \pm 0.2) \text{ms}$. This confirmed that VWF bound to the DNA, but only when VWF was stretched and the hidden A1 domains become accessible. Furthermore, when salt was added the curves shifted to the left resulting in a reduction of the bound fraction by $(57 \pm 4) \%$, further confirming that the interaction between DNA and VWF is electrostatically driven.

Repeating these experiments with the longer 42 bp dsDNA, revealed the same effect. By fitting the autocorrelation curve for the 42 bp dsDNA a diffusion time of $(210 \pm 4) \mu\text{s}$ and hence a diffusion coefficient of $(71 \pm 8) \mu\text{m}^2 \text{s}^{-1}$ was obtained. Upon addition of VWF and shearing, an increase in diffusion time to $(1.1 \pm 0.5) \text{ms}$ for the bound complex was observable (Figure 7.2 (B)). Hence, I not only showed that the interaction is conformation and salt dependent, but also that binding is independent of DNA sequence.

Additionally, these results were affirmed by EMSA (Figure 7.2 (C)). Here, different concentrations of multimeric or dimeric VWF were mixed with 300 nM of the 42 bp ARC1172 DNA and run on an agarose gel. Small or highly negative molecules run faster and travel further than large or charge neutral/positively charged molecules (s. 3.3). Unbound dsDNA migrated quickly through the agarose matrix and was observable as a single band at the bottom (Ctrl ds DNA samples). However, when DNA was bound to the large and charge neutral VWF, migration was slower and a second higher band was visible in the red channel. The Dimer VWF band was determined in the green channel since the protein was fused with an eGFP molecule (s. B). Not only for the multimeric VWF but also for the dimeric VWF a DNA band was observable at this protein region.

To investigate the salt effect more thoroughly EMSA studies were carried out at different salt concentrations. Figure 7.3 (A) exemplifies a titration series of full-length VWF Dimer with 500 nM dsDNA, where at lower Dimer concentrations the fraction of dsDNA at the Dimer band decreases. The fluorescence signal of the dsDNA at the Dimer position was normalized and plotted against the Dimer concentration (Figure 7.3 (B)). To deduce the dissociation constant for different salt concentrations, the general binding isotherm (Eq. 2.9) was fitted. An increase in ionic strength of 40 mM resulted in a 100-fold reduction

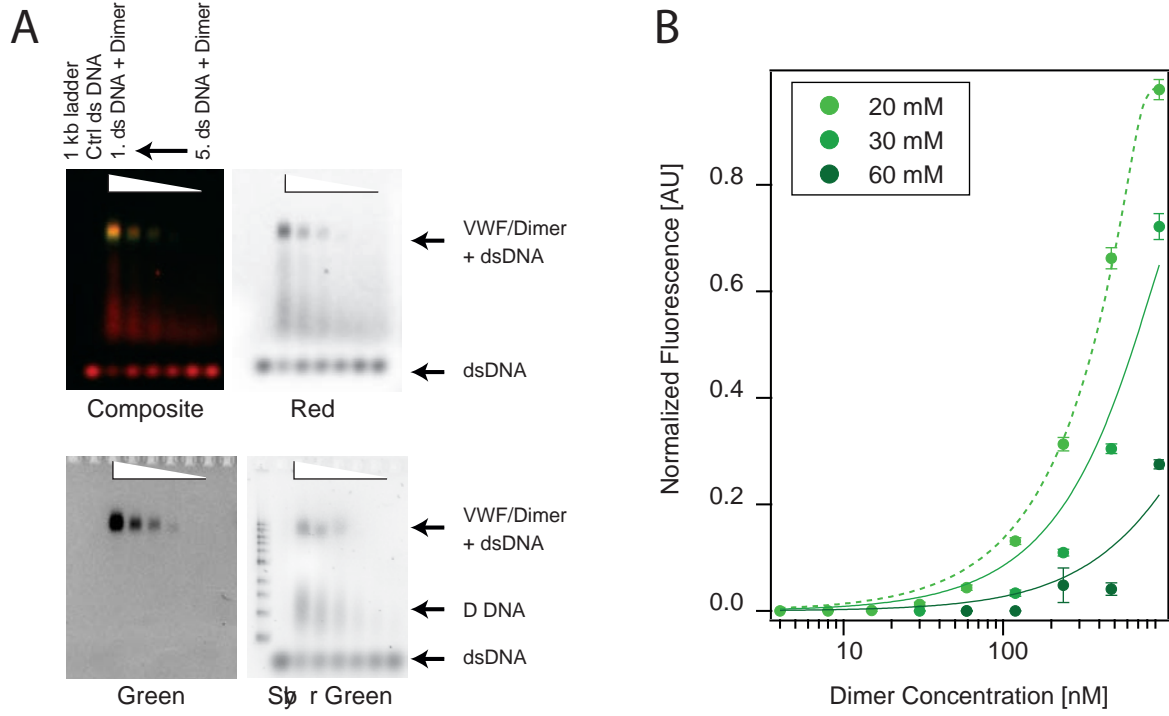


Fig. 7.3.: Binding of dsDNA to VWF Dimer analyzed by EMSA. (A) EMSA for ARC1172 42 bp dsDNA ($c = 500$ nM) binding to a concentration series of full-length VWF Dimer from 0.47 mg ml^{-1} to $15 \text{ } \mu\text{g ml}^{-1}$ at an ionic strength of 20 mM. Ctrl ds DNA contains 500 nM Cy5 labelled DNA only. Composite image shows an overlay of green channel (eGFP-Dimer) and red channel (Cy5 DNA). The Sybr Green image shows the gel after staining. For visualization purposes the upper sections of the Red channel was contrast enhanced. (B) Normalized dsDNA fluorescence analyzed at the Dimer band for different ionic strengths from 20 mM to 60 mM. Data was fitted with K_D values from (21 ± 20) nM to (3 ± 1) μM , respectively.

in binding strength from $K_D = (21 \pm 20)$ nM to $K_D = (3 \pm 1)$ μM . Also, when the ionic strength was further increased to 80 mM no binding of the 42 bp DNA to the VWF Dimer was deduced (App. Fig. A.2). These results indicate that the binding of VWF and DNA is strongly influenced by electrostatics and confirm the predictions made by the BD and MD simulations as well as the results of thermophoresis and FCS experiments. Additionally, binding of the ARC1172 ssDNA to the VWF Dimer was analyzed with EMSA (App. Fig. A.3). Also here, a clear band shift was observable and allowed the determination of a dissociation constant. Plotting the normalized fluorescence of the ssDNA at the Dimer band against the DNA concentration and fitting with the general binding isotherm (Eq. 2.9) resulted in a K_D value of (1 ± 6) nM. Both experiments for

ssDNA and dsDNA therefore suggest similar K_D values, which are also in agreement to literature [165]. In summary, a strong salt dependence of VWF-DNA binding was revealed by EMSA studies. These results agree with observations made by thermophoresis and FCS experiments as well as *in silico* studies.

7.3 | Discussion

Overall, a variety of biophysical methods were suitable to characterize the binding of VWF and its A1 domain to ssDNA as well as to dsDNA. Taken together, the results obtained with different techniques agree within errors and confirm model predictions made by BD and MD simulations. Here, the A1 domain with its four arginines was identified as the main binding region for DNA. With thermophoresis I was able to experimentally confirm this statement. While the wt A1 domain bound to dsDNA and ssDNA with a K_D value of $K_D = (13 \pm 1) \mu\text{M}$ and $K_D = (10 \pm 2) \mu\text{M}$ the arginin-depleted A1 domain bound significantly weaker ($K_D = (30 \pm 6) \mu\text{M}$, $K_D = (130 \pm 7) \mu\text{M}$), respectively. A source of uncertainty, however, remains due to the limiting A1 domain concentration and therefore, a plateau in the binding isotherm was not reached. Hence, the obtained K_D values should be interpreted as a broad estimate, not as strict values. Nevertheless, a clear distinction could be made for wt A1 domain and mutant A1 domain, identifying the positively charged arginines as main interaction sites for DNA binding. Additionally, a clear hint towards the electrostatic nature of the interaction was provided when binding was remarkably reduced upon increasing the ionic strength of the buffer from 162 mM to 312 mM, which was also in good agreement with BD and MD simulations.

These results were then further validated with the full-length VWF characterized with FCS and EMSA. Regarding FCS, a decrease in the diffusion coefficient for the 23 bp DNA from $(80 \pm 10) \mu\text{m}^2 \text{s}^{-1}$ to $(18 \pm 2) \mu\text{m}^2 \text{s}^{-1}$ with 22 % of DNA being in the bound state was observed. Similarly, for the 42 bp DNA a reduction in the diffusion coefficient from $(71 \pm 8) \mu\text{m}^2 \text{s}^{-1}$ to $(13 \pm 8) \mu\text{m}^2 \text{s}^{-1}$ was measured. These results agree well with values reported by Lippok et al. ($19.5 \mu\text{m}^2 \text{s}^{-1}$) [69]. Binding, however, was only observable when VWF was sheared, suggesting that VWF needs to be stretched in order to expose its binding domain to DNA. In fact, literature supports these findings for different proteins interacting with the A1 domain of VWF such as collagen or the *GPIIb* on platelets [64]. Numerous studies have shown that VWF transitions from an inactive closed state to an active open conformation under shear stress above 1000s^{-1} [65, 71, 166, 167]. It is presumed that VWF thereby can link platelets to collagen on the blood vessel walls [68]. And hence, a similar function can be hypothesized for VWF mediating the immobilization

of NETs in the blood stream [23].

Apart from conformational effects on VWF DNA binding, electrostatics have been identified to play a pivotal role. In all experimental studies, as well as in the simulations, it was shown that an increase in ionic strength of the buffer reduced binding of VWF to DNA. FCS measurements showed that upon addition of 150 mM NaCl a reduction of the complexed fraction by $57 \pm 4\%$ was obtained, and hence presumably the binding strength of VWF towards DNA decreased. With EMSA I then investigated the electrostatic nature of VWF binding to DNA more thoroughly. Here, K_D values were obtained for various salt concentrations, showing a clear reduction in binding strength at higher ionic strengths. At low salt concentrations, K_D values ($K_D(ssDNA) = (1 \pm 6) \text{ nM}$ and $K_D(dsDNA) = (21 \pm 20) \text{ nM}$) are in good agreement with the nanomolar range values reported by Huang et al. ($K_D = 0.6 \text{ nM}$) [165]. Similar to the MST measurements, however a plateau for the dsDNA was not determinable, resulting in a large uncertainty regime. Nevertheless, a clear trend towards weaker binding for higher salt concentration was observable. This observation of salt-dependent binding has also been reported for other proteins binding to the A1 domain of VWF (e.g. *GPIb α* and Histones) [74–76]. While Jiang et al. found that VWF extension is not affected by increasing salt concentration, binding of *GPIb α* on platelets to VWF is drastically reduced [75].

Comparing the measurements conducted with thermophoresis and EMSA reveals that not only the interaction of the A1 domain with DNA but also the interaction of the VWF Dimer with DNA is salt dependent. Interestingly, the interaction of a single A1 domain was remarkably weaker ($K_D = 13 \mu\text{M}$) than the interaction of the dimeric VWF molecule ($K_D = (21 \pm 20) \text{ nM}$). A key factor explaining this finding is that the thermophoresis experiments with the A1 domain had to be carried out at higher salt concentrations due to lack of protein stability. Another explanation for these observations, however, might be a multivalency effect, which has previously been proposed in literature for multiple binding interactions with VWF [168–174]. Furlan summarizes the different association rates obtained for monomeric versus polymeric VWF with up to 100 fold higher affinities for the multivalent molecule [174]. Here in this work, for the VWF Dimer at least two A1 domains can bind with DNA (apart from other domains within a VWF Monomer). Taking the multivalency theory described in Chapter 2 into account, allows to roughly estimate the increase from monovalent binding strength to bivalent binding. If one assumes $K_D(bi) = K_D(mono)^2$, the estimation for the bivalent Dimer VWF would be $K_D(Dimer) = 0.2 \text{ nM}$, which is 10-fold lower than what has been determined with EMSA. But, taking into account that this estimation does not yet correct for any energy constraints and that the ionic strength for EMSA was significantly lower than for MST

measurements, these values match reasonably well. Another finding which supports this theory is the fact that binding of short DNA (16 bp) was not observed with EMSA (s. App. Fig. A.4). Indeed, this is expected when estimating the size of DNA and the distance between two A1 domains within a dimeric VWF molecule. For the 16 bp DNA a maximal length of 5.44 nm, and for the 42 bp DNA 14.28 nm would be expected (Eq. 2.26). Fu et al suggested an interdomain distance of 20 nm between two adjacent A1 domains [72]. Therefore, the 42bp DNA would not fully match the distance for a completely stretched VWF. However, when the VWF Dimer is not completely stretched, these distances might be shorter and hence allow for a bivalent interaction of the 42 bp DNA with two A1 domains of the VWF Dimer. But, the 16 bp DNA will certainly not enable simultaneous binding and therefore might explain that no interaction of the 16 bp DNA to VWF was observed in EMSA. Also, possibly due to the weak interaction and putatively due to lower shear forces in EMSA compared to FCS shear experiments, no binding was measurable for the 16 bp DNA (s App. Fig. A.4). Nonetheless, further tests are required to verify this theory. Confirming this assumption could potentially involve testing the binding of DNA with different lengths between 40 bp and 60 bp to the VWF Dimer and comparing these affinities to monomeric VWF in the future. To summarize, the experimental data affirms that binding of VWF and DNA is independent of DNA sequence, dominantly affected by electrostatic interactions and necessitates VWF to stretch and expose the A1 domain.

Conclusion and Outlook

8 | Conclusion and Outlook

In this dissertation, I characterized two biological interactions occurring in the human body influenced by multivalency. On the one hand, FasL induced apoptosis and on the other hand, VWF interacting with DNA. Additionally, I tested a new approach for the determination of ligand receptor binding on living cells. Further, I developed a DNA origami model system for a quantitative study of multivalent binding.

Starting with the first biological interaction, FasL apoptosis induction, previous studies had already shown that single FasL binding to FasR on cells do not efficiently induce apoptosis. However, multiple linked FasL were found to increase cell death induction [20, 81–83, 175]. In order to investigate this multivalency effect on cells in a defined manner, I constructed a DNA-based FasL platform which allowed the study of valence of FasL as well as FasL-FasL distance affecting signaling efficiency. Studying various different constellations of FasL attached onto a one-layer DNA origami sheet presented to cells on a lipid bilayer, have enabled to identify the key factors defining apoptosis triggering. Unlike expected, FasL number was less crucial compared to FasL spacing. It was found that a spacing of 10 nm between two adjacent FasL most effectively induced apoptosis, which agrees well with previous studies by Balta et al. and Scott et al. [20, 80]. For example, Balta et al. had functionalized single FasL proteins on a supported lipid bilayer. By varying the amount of FasL on the membrane they deduced an optimal average FasL-FasL spacing of 9 nm [20]. Although I found that a hexagonal conformation of six FasL on the DNA origami was significantly more effective, two FasL were sufficient to quickly induce apoptosis triggering. Remarkably, it was also noticed that distances exist which presumably inhibit apoptosis, which has not been observed so far. In fact, the model suggested by literature support these findings [72, 79, 84, 86, 87]. Here, theories presume that in order to induce apoptosis via caspase activation, the intracellular unit of FasR requires to dimerize with adjacent FasR receptor units. However, if FasL order FasR in disproportionate arrangements, the FasR spacing is locked and efficient dimerization is likely to be prohibited and therefore apoptosis triggering. My present investigations

support this theory and future work might provide a more detailed understanding. Using superresolution or Fluorescence Resonance Energy Transfer (FRET), for example, might further explain this clustering effect. Resolving the intracellular cluster formation of FasR induced by my FasL DNA origami nanoagents might allow additional insights into the whole signaling process. Previous work by Schichthaerle et al. for instance had shown that they could measure an inner cell protein complex with a resolution of three nanometers [176]. Another example is the study by Ma et al., in which they were able to characterize T-cell receptor clustering by FRET [177]. Although my work allowed to determine that less than 100 FasL DNA Origamis were sufficient to induce efficient apoptosis, an interesting question remains how the number of engaged FasL proteins translate to the number of FasR clusters on the surface and inside of the cell. Are FasR clusters confined to certain areas or widely spread amongst the cell surface? Additionally, death times can be controlled by different configurations of FasL but the question arises: how do they transfer to signaling times within the cell? For example, are signaling clusters simultaneously activated by multiple FasL DNA origami? Studying these timings could possibly give answers to the occurrence of two populations in death times observed for FasL Dimer DNA origami or FasL functionalized via monovalent Streptavidin. In a related system, namely the TRAIL apoptosis induction, however, it was found that mitochondrial levels influence the timing of cell response and should be investigated in future research as well [178]. Taken together, the developed DNA origami platform not only provided new insights for the understanding of the FasL-FasR signaling process and offers a versatile tool for future investigations, where stoichiometrically defined and nanometer precise arrangements of FasL are required. But also, the results in this dissertation might advance the development of therapeutic drug design. Knowing the key aspects of apoptosis triggering, might facilitate eliminating e.g. cancerous tissue by smart and adaptable DNA based nanomedicine.

To study multivalency binding interactions on living cells, a method was developed to allow the characterization of binding affinities with FCS. The new approach presented here was to study the concentration of free ligands in solution instead of the bound fraction. Therefore, a ligand depletion theory had been introduced, which predicted the effect of concentration decrease as a function of cells present in the sample and the expression of receptors per individual cell. First, binding of a commercially available antibody binding to CD33 receptors overexpressed on HEK cells upon antibiotic induction was verified. Next, different set-ups had been developed to ensure separation between cells and the detection volume of FCS. Yet, up to now, the tested set-ups suffer from non-specific

adsorption effects that impede a quantitative characterization of antibody binding to cells. However, possible improvements, that could be tested in future research, include: Firstly, reducing the sample size to microliter volumes by, for example, using laser ablation to create glass sample chambers [142–144]. Secondly, testing different membranes or hydrogels with larger mesh sizes. Research by Golden et al. for instance exemplified how they fabricated hydrogel networks for selective macromolecule and particle delivery [138]. Both suggestions might solve one major drawback of this method, namely the extensive equilibration time, which putatively effects cell viability as well as it might introduce artefacts due to internalization. Thereby, combined with further improvements concerning the set-up development, this new approach might provide a new tool for the study of multivalent binding interactions on living cells.

In order to characterize multivalency itself in a defined manner, a DNA based multivalent platform was developed. The aim was to create a multivalent ligand-receptor system whereby binding was solely mediated via DNA hybridization of single stranded DNA overhangs. Thereby, this tool benefits from a well predictable nanometer precision which allows to characterize multivalency as a function of individual (sequence dependent) binding strength as well as receptor ligand distance. DNA origami was chosen to serve as a multivalent receptor by having protruding single stranded handles at distinct places serving as binding sites for ligands. These ligands either consisted of a tetravalent DNA Holliday Junction or a bivalent dsDNA rod with single stranded arms to bind to the DNA origami. The spacing of ligand binding sites were defined such that they match the distances of the binding sites on the DNA origami. By applying multiple different methods, I verified binding of the ligand to the DNA origami. However, the determination of multivalency effects were limited by the following effects: Firstly, the K_D range determination was restricted by the maximal concentration of DNA origami that was synthesizable without facing aggregation problems. Secondly, the sensitivity of the methods applied did not allow for a reliable K_D determination below 0.5 nM. Therefore, up to now, only for the 10 bp hybridization, both, the monovalent and the bivalent interaction were well characterizable. Here, by adapting theoretic assumptions presented in literature a lower boundary was estimated [34–36]. At the same time, by assessing the electrostatic repulsion effects, resulting from the negatively charged DNA, an upper boundary was deduced. Taken together, both theoretical calculations frame the gathered effects measured in this thesis. These findings, therefore, provide a number of important implications for future practice. They show that it is crucial for further research to choose the right combination of methods which together allow the determination of weak as

well as strong interactions for multiple hybridization lengths. While it was found that FCS is limited to K_D values in the range of 0.5 nM to 100 nM, surface based methods might enable the characterization of K_D values above 100 nM as less material is required. Here, as little as 0.5 nM DNA origami are sufficient to create a fully covered surface of DNA origami and thereby circumvent high sample concentrations needed for weak binding interactions in solution [59]. However, it has to be kept in mind that e.g. TIRF is restricted, on the one hand, by bleaching for strong binding events and, on the other hand, by the minimal on-time required to gather enough photons for a reliable signal-to-noise ratio. In parallel, using non-fluorescent methods such as surface plasmon resonance might benefit as an additional technique verifying results obtained by TIRF and FCS [128, 163]. In summary, my results therefore provide new insights and important suggestions for future experimental design.

Last but not least, I was able to determine four key factors influencing binding of the multivalent VWF to DNA. Firstly, using MST, I identified the A1 domain and its three arginines as the main binding sites of VWF for DNA, in agreement with MD and BD simulations. Secondly, FCS showed that the binding interaction was DNA sequence independent and thirdly, shear sensitive. These three results coincide with the natural habitat and structure of VWF. The A1 domain of VWF is only accessible when VWF is stretched e.g. due to the blood flow in blood vessels [64–66, 71, 164, 166, 167]. Finally, with MST, FCS and EMSA, I found that the VWF-DNA interaction was strongly dependent on the ionic strength of the buffer. This has also been noticed for other proteins interacting with VWF and is likely due to the negatively charged phosphates of DNA and the positively charged arginines of the A1 domain of VWF [23, 74–76]. Moreover, it was observed that both single stranded and double stranded DNA interact with VWF and that the length of DNA influences binding. For short DNA (16 bp), for instance, no binding to VWF was measureable. This result putatively originates from multivalency as the affinity might have been too low to be observable with the applied methods. However, for longer DNA (42 bp) presumably the binding strength is enhanced as it might be able to interact with two A1 domains at the same time. In fact, an increase in binding strength was derived, when comparing the K_D value determined for the single A1 domain (micromolar range) to the values measured for the VWF Dimer (nanomolar range). However, to further investigate how multivalency effects VWF-DNA binding, additional experiments are required. It remains to be studied in more detail how the binding strength depends on DNA length. What is the minimum length required so that DNA can interact with multiple units of VWF at the same time? Moreover, a comparison of the strength of DNA

binding to monomeric, dimeric and multimeric VWF could clarify if the multivalency effects arise from multiple binding interactions with the A1 domain, as suggested by my results. Or whether also other units within one VWF monomer influence binding to DNA. To summarize, the data of the VWF-DNA binding measurements combined with MD and BD studies provide comprehensive insights on the key parameters affecting this interaction and thereby aid the understanding of its role in capturing pathogens inside blood vessels.

From DNA origami model systems to living cells, the findings presented in this dissertation provide a comprehensive overview of multivalent binding processes in biology and at the same time evidence the strength of DNA nanotechnology as a powerful tool for studying multivalency interactions. Most importantly, my work shows that once we understand the underlying mechanism we can stimulate cells in a controlled manner by artificially designed nanoagents. In particular, functionalizing DNA nanotechnology agents with, for instance, viral proteins could generate an immune response and thereby serve as future vaccines. In addition, attaching ligands in a distinct manner using multivalency effects to allow interactions only with virus particles, might improve blocking agents preventing viruses from entering the host cell in the first place. These easily adaptable novel drugs might provide future solutions for pandemic outbreaks requiring fast medication.

Nothing in life is to be feared,
it is only to be understood.
Now is the time to understand more,
so that we may fear less.

Marie Curie
first woman to be awarded a Nobel Prize

Appendix

A | Supplementary Information

Differential Equations A.1

$$\frac{d[RR]}{dt} = k_1[lRR] + k_{-2}[RRl] - (k_1 + k_2)[RR][ll]$$






$$\frac{d[RR]}{dt} = k_1[lRR] + k_{-2}[RRl] - (k_1 + k_2)[RR][ll]$$

$$\frac{d[lRR]}{dt} = k_1[RR][ll] + k_{-2}[lRRl] - k_1[lRR] - k_2[lRR][ll] - \frac{k_2}{f}[lRR][S]$$

$$\frac{d[RRl]}{dt} = k_2[RR][ll] + k_{-1}[lRRl] - k_2[RRl] - k_1[RRl][ll] - \frac{k_1}{f}[RRl][S]$$

$$\frac{d[lRRl]}{dt} = \frac{k_1}{f}[RRl][S] + \frac{k_2}{f}[lRR][S] - (k_1 + k_2)[lRRl]$$

Tab. A.1.: Different FasL DNA origami nanoagents. Distance refers to the average spacing of two adjacent FasL molecules on DNA origami. Peak locations for Gaussian fit of apoptotic events for coupling with wt Streptavidin or mv Streptavidin.

Name	Illustration	Distance [nm]	Peak Location [h] wt Streptavidin	Peak Location [h] mv Streptavidin
NH10		10	$3, 1 \pm 0, 1$	5.9 ± 0.2
NH5		5	17 ± 1	$15 \pm 0, 4$
NH30		30	$14 \pm 0, 3$	17 ± 17
ND10		10	$3, 6 \pm 0, 1$	$12, 5 \pm 0, 1$
ND20		20	$3, 5 \pm 0, 1$	$12 \pm 0, 3$

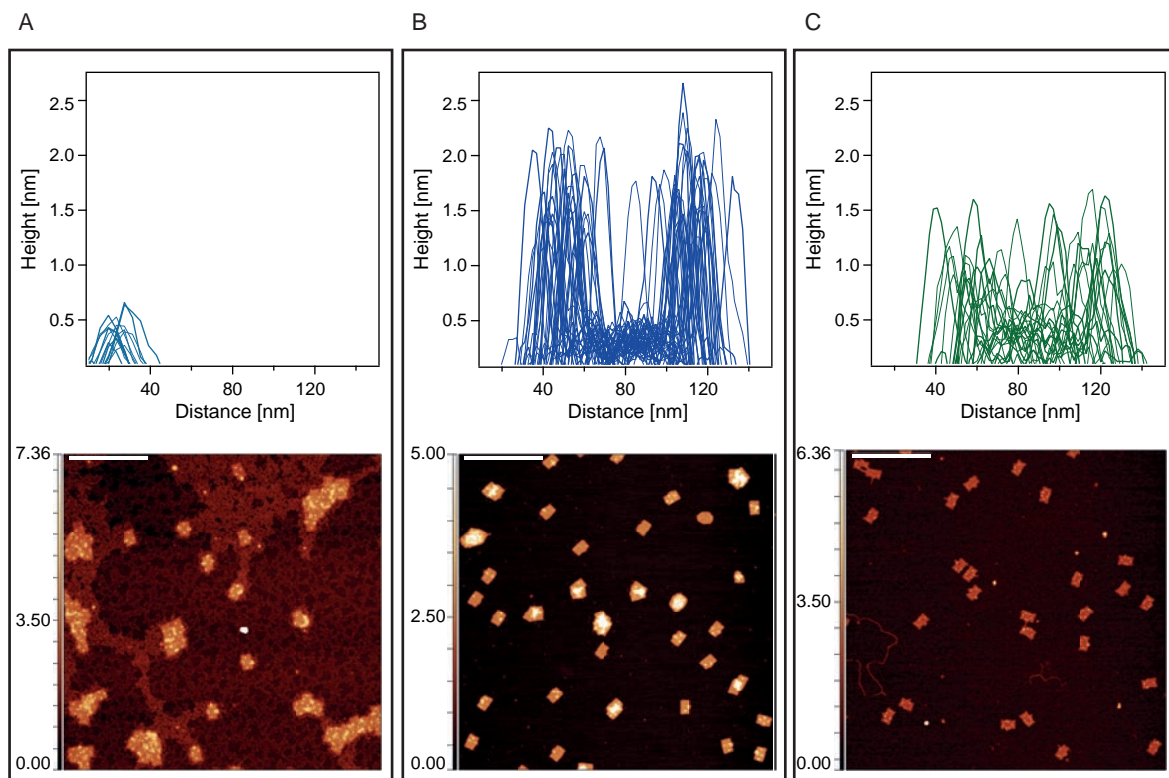


Fig. A.1.: Evaluation of FasL arrangement on DNA origami with AFM. Evaluation of FasL height on mica (A), FasL and Streptavidin height on DNA origami (B) and Streptavidin height on DNA origami (C).

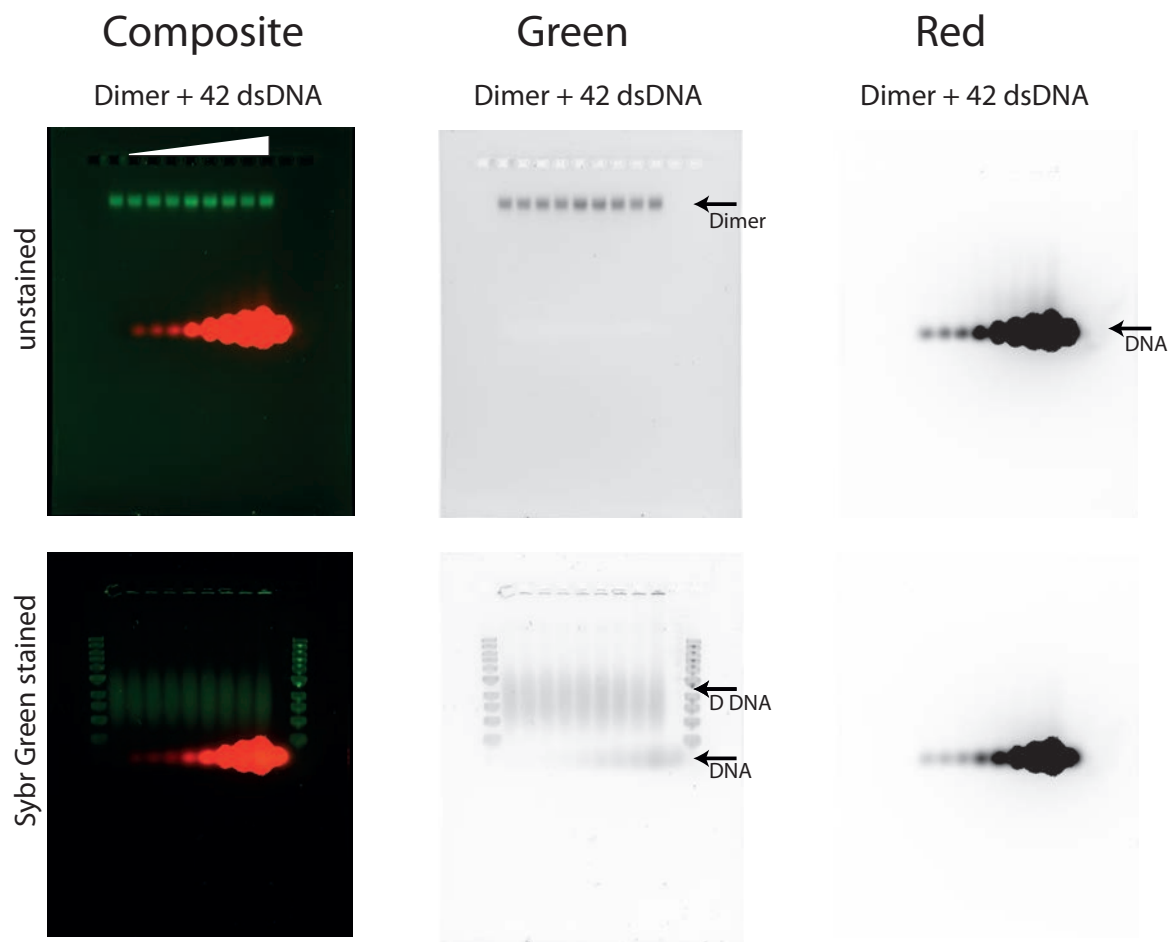


Fig. A.2.: EMSA for full-length Dimer ($c = 0.47 \text{ mg ml}^{-1}$) binding to a concentration series of ARC1172 42 bp dsDNA from $5 \mu\text{M}$ to 20 nM . Ctrl dsDNA only contains 500 nM Cy5 labelled DNA. No DNA signal in the red channel is observable at the Dimer band.

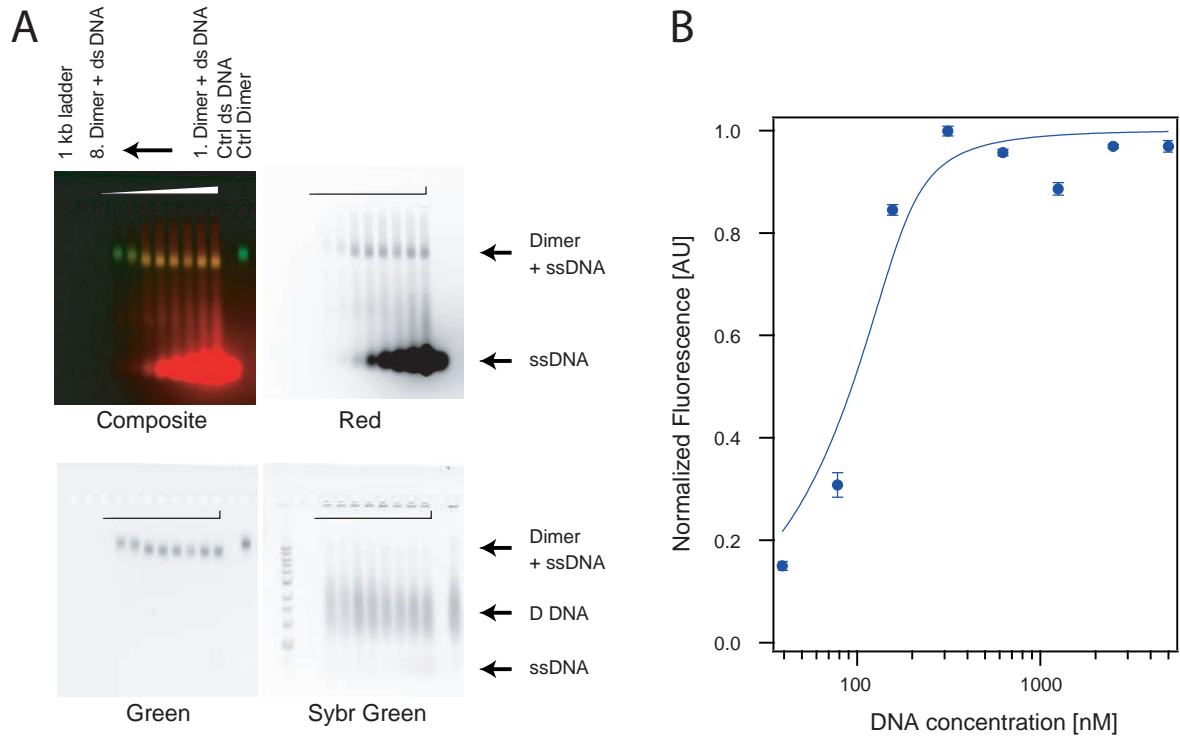


Fig. A.3.: Binding of ssDNA to VWF Dimer analyzed by EMSA. (A) EMSA for full-length Dimer ($c = 0.47 \text{ mg ml}^{-1}$) binding to a concentration series of ARC1172 42 bp ssDNA from $5 \mu\text{M}$ to 20 nM . Ctrl dsDNA contains 500 nM Cy5 labelled DNA only. Composite images show an overlay of green channel (eGFP-Dimer or Sybr Green) and red channel (Cy5 DNA). (B) Normalized ssDNA fluorescence analyzed at Dimer band and fitted with general binding isotherm with $K_D = (1 \pm 6) \text{ nM}$

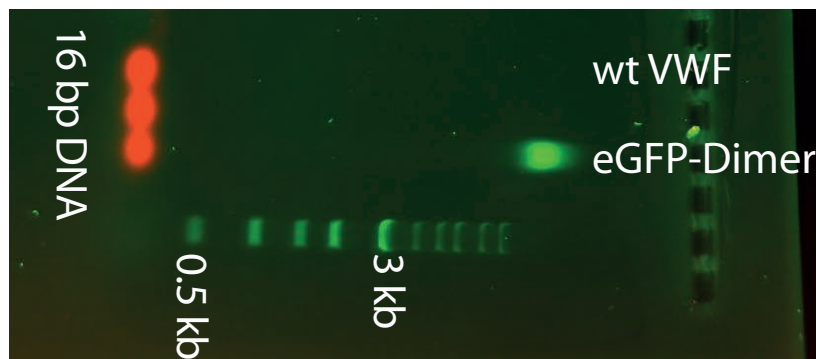


Fig. A.4.: No Binding of 16 bp short DNA to VWF analyzed by EMSA. Composite image of green channel (eGFP-VWF Dimer, $c = 0.47 \text{ mg ml}^{-1}$) and red channel (16 bp DNA, 500 nM). No DNA band at VWF Multimer or VWF Dimer band observable.

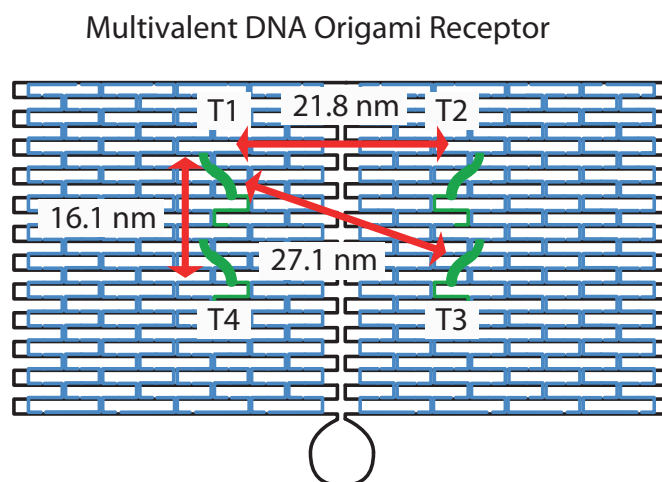


Fig. A.5.: Multivalent DNA origami receptor with distances between binding sites as specified in the image.

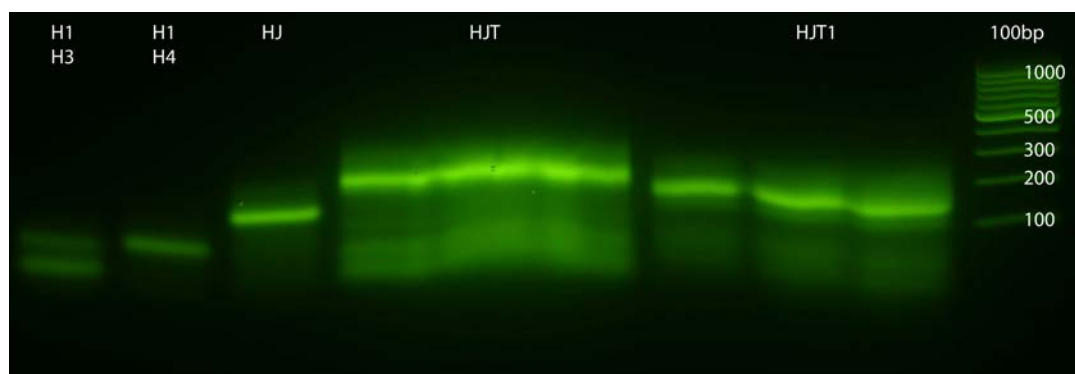


Fig. A.6.: Agarose purification of Holliday Junction. Green channel (Sybr Green staining) of an EMSA image depicting folding of the tetravalent Holliday Junction (HJ). Bands show result after annealing of different components: HJ body strand H1-H4, where H1 is complementary to parts of H2 and H4, but not to H3; target strands T1-T4 complementary to only one HJ body strand indicated by the number. HJ denotes the hybridized body strands, HJT1 body strands with target strand T1 and HJT is the fully folded structure. The upper band in HJT was extracted from the gel.

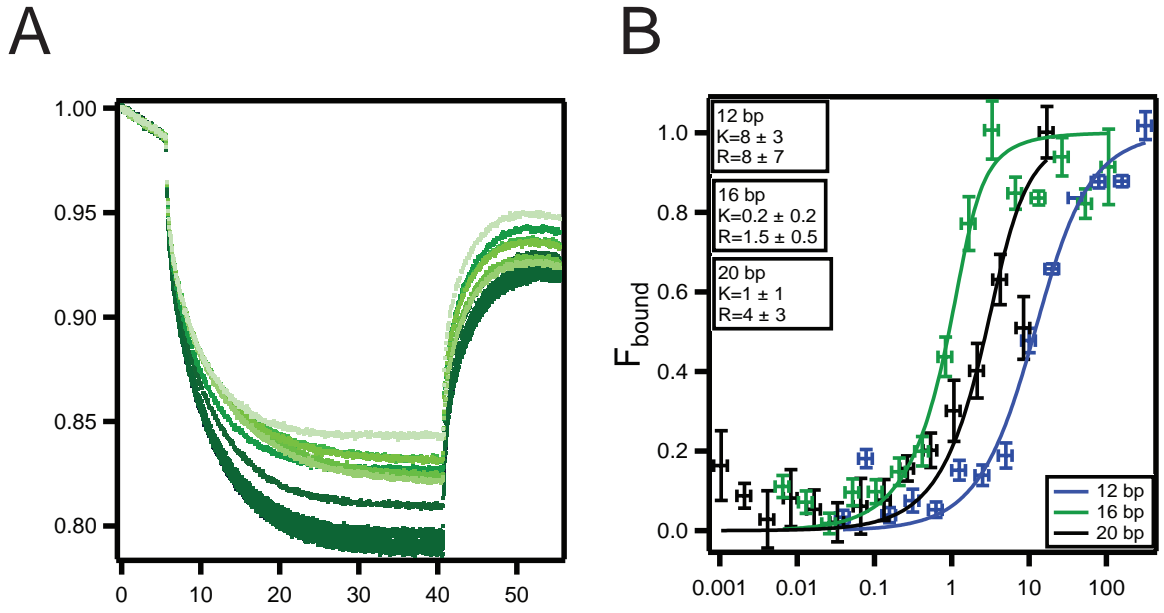


Fig. A.7.: Binding measurements with MST. (A) Raw data and (B) normalized binding isotherms with fitted values given in legend in nanomolar for 12 bp, 16 bp and 20 bp hybridization (R and K_D).

B | Protocols

B.1 | Proteins and DNA

DNA was either purchased by Eurofins Genomics Germany GmbH (Martinsried, Germany), Integrated DNA Technologies, Inc (Iowa, USA) or biomers.net GmbH (Ulm, Germany) and stored aliquoted in water at -20°C until further usage.

Full length VWF, A1 domain (both from Department of Pediatric Hematology and Oncology, University Medical Center Hamburg-Eppendorf) and FasL (Apogenix AG, Heidelberg, Germany) were stored aliquoted at -80°C and were defrosted briefly before measurement. The A1 domains were purified three times with 10 K Amicon Ultra Centrifugal Filters (Merck KGaA, Darmstadt, Germany) with PBS. Wildtype Streptavidin (Merck KGaA, Darmstadt, Germany) was stored in -20°C and monovalent Streptavidin (LS Gaub, Physics Department, LMU) was stored in PBS in fridge. The CD33 antibody, purchased from Novus Biologicals (Colorado, USA), was stored according to manufacturer instructions. Protein and DNA concentration were measured with a NanoDrop TM 1000 Spectrophotometer prior to measurements.

B.2 | DNA Origami Preparation

To design binding sites for the hybridization studies or protein attachment on the DNA origami one layer rectangular sheet, either the caDNAno 2.0 or Picasso software was used [58, 59]. The p7249 scaffold was bought from tilibit nanosystems GmbH (Garching, Germany). The folding mixture consisted of 10 nM scaffold with 10x excess of staple strands, 30x excess of fluorescent oligos, 80x excess for biotinylated oligos and 8 nM Cholesterol-TEG modified DNA in a 1x TAE buffer with 12.5 mM MgCl₂. The DNA origamis were annealed in a 16 h temperature ramp from 65 °C to 20 °C. Correct folding was evaluated with EMSA or AFM. Folded DNA origamis were stored at 4 °C unpurified until further usage.

B.3 | DNA Origami Surface Preparation

Lipid membrane preparation was done according to Kemper et al. in chambers prepared with Ibidi sticky-Slide VI 0.4 (Martinsried, Germany) and precision cover glasses No. 1.5H (Paul Marienfeld GmbH & Co. KG, Lauda-Königshofen, Germany) [115]. To functionalize DNA origami on the supported lipid bilayer, 100 nM Cholesterol DNA was added in PBS buffer to the channel and incubated for 15 min. Next, the channels were washed twice with both PBS and 1x TAE 11 mM MgCl₂ buffer (O-Buffer). Afterwards, unpurified DNA origamis were added and incubated for 30 min, before washing twice with O-Buffer and twice with A-Buffer (10 mM Tris-HCl, 100 mM NaCl, pH 8.0). Next, 2.8 μ M Streptavidin was incubated for 10 min and rinsed before FasL was added at a concentration of 0.2 μ M for 10 min. Then, channels were washed with A-Buffer and with L15 (ThermoFisherScientific, Waltham MA, USA) supplemented with 10 % fetal bovine serum (FBS).

B.4 | Cell Measurements

For FasL studies HeLa cells transfected with pIRESpuro2 from Clontech at AG Monzel (Experimental Medical Physics, Heinrich-Heine University, Düsseldorf, Germany) to stable express human CD95-mGFP were used. Cells were cultivated in DMEM Glutamax bought from ThermoFisherScientific (Waltham MA, USA), which was supplemented with 10% FBS. For timelapse measurements cells were detached with Accutase and 2000 cells were seeded into each functionalized chamber in L15 with 10 % FBS. To prevent evaporation Anti-Evaporation Oil from Ibidi (Martinsried, Germany) was added into each well. The prepared slides were immediately transferred to the preheated microscope chamber and every 10 min alternatingly brightfield and fluorescent images were recorded for 20-30 h. Antibody binding studies were measured with HEK 293 Flp-In TREX cells from Invitrogen, which had been transfected with the pcDNAFRT-TO vector carrying the insert huCD33 VL at the LS Hopfner Genecenter, LMU. The expression of huCD33 was induced one day prior to experiments by supplementing culture medium (DMEM, 10% FBS, 15 μ g ml⁻¹ Blasticidin, 100 μ g ml⁻¹ Hygromycin) with 1 μ g ml⁻¹ Tetracycline. To transfer cells from culturing flask to sample carrier cells were gently washed with PDMS until they detached.

B.5 | MST Experiments

Prior to MST experiments the proteins or DNA were titrated in a 1:1, 1:10 or 3:1 dilution with PBS or O-Buffer. Subsequently, Cy5 labelled DNA was added to a final concentration of 5 - 10 nM. After a 10 min - 1 h incubation, samples were filled into NT.115 MST standard capillaries and investigated on a Monolith NT.115 Pico instrument (NanoTemper Technologies, Munich, Germany) at 22 °C with 2 - 10 % excitation laser power and 40 % infrared laser power with off and on times of 5 and 25 seconds, respectively. After four measurements per condition and normalization, the change in normalized fluorescence ΔF was batch fitted with the general binding isotherm Eq. 2.9.

B.6 | FCS Experiments

FCS binding experiments were investigated on an Axiovert 200 microscope equipped with a high NA 40x water-immersion Apochromat objective and a ConfoCor 2 unit (Carl Zeiss, Germany). For excitation a Helium-Neon or Argon Laser was used and the confocal volume calibrated with a Cy5, Alexa 633 or Alexa 488 dye in the measurement buffer, depending on fluorophore of the sample, was used, respectively. Sample chambers were passivated either with 5 mg ml⁻¹ BSA or milk to prevent binding to chamber walls. For share experiments a home-built sample holder and motorized cylindrical rotation device was used to ensure constant flow of 2000 s⁻¹ to 4000 s⁻¹ directly prior to measurement [69]. DNA-DNA origami hybridization studies were carried out in a 384-Well Polypropylene Microplate bought from Greiner Bio-One GmbH, Germany. Antibody binding to living cells was either measured in NUNC Lab-Tek 8-Well plates with a borosilicate cover glass bottom and polystyrene side parts (Thermo Scientific, Rochester, USA) for the insert studies or in Ibidi VI 0.4 slides for the hydrogel studies (Martinsried, Germany). Millicell Cell Culture Inserts were bought from Merck KGaA, Darmstadt. Polydimethylsiloxane (PDMS) wells and hydrogels were prepared one day prior to experiments. PDMS prepolymer solution was diluted with 10:1 ratio with cross-linker (Sylgrad 184, Dow Corning, USA). Afterwards, it was degassed under vacuum and poured around an insert holder in a NUNC chamber. Next, it was degassed again and baked at 50 °C. On the next day, the insert was removed and the measurement cavity was manually drilled into the PDMS. The hydrogel preparation protocol can be found in [135]. Each sample was measured 10 times for 30 seconds. Afterwards, curves were analyzed and curves with large spikes in countrate were rejected from further analysis. To determine the particle number N and

the diffusion time τ_D , the remaining curves were averaged and fitted with Eq. 3.16.

B.7 | EMSA Experiments

Agarose gels were prepared freshly with TA or TAE buffer and heated for 2 min, then poured into a casting box and cooled for 30 min. Usually, prior to measurements, samples were prepared in TA or TAE buffer, occasionally supplemented with salt such as MgCl or NaCl as stated in results section. The dried gel was transferred into an electrophoresis box, buffer was added and run cooled at a constant volt of 70 V for 2 h. Afterwards, the gel was imaged on a Chemidoc MP (Bio-Rad Laboratories GmbH, Feldkirchen, Germany) with 530/28 and 695/55 filter sets to evaluate the blue or red Epi illumination. Next, gels were stained with Sybr Green or Sybr Gold from Thermo Fisher Scientific (Waltham, USA) to label DNA and imaged again. For protein binding studies, gel was afterwards stained with PageBlue Protein Staining Solution also from Thermo Fisher Scientific and imaged again. PAGE gels were bought from Bio-Rad Laboratories GmbH (Feldkirchen, Germany) and run cooled in TA buffer for 30 min at 150 V. Imaging procedures were equivalent to agarose gels.

B.8 | AFM

Prior to AFM measurements, DNA origamis were purified 5x with Amicon Ultra-0.5 Centrifugal Filters bought from Merck (Darmstadt, Germany). Afterwards, DNA origamis were incubated at a concentration of 1.5 nM on a mica for 10 min. For dry imaging, mica were rinsed afterwards 3x with filtered water and dried with Nitrogen. Here, the OMCL-AC160TS tip from Olympus Corporation (Shinjuko, Japan) was utilized. For liquid imaging, 1.5 ml TAE buffer with 11 mM MgCl₂ was added before measuring with either a BL-AC40 TS tip from Oxford Instruments Asylum Research (Goleta, CA, USA) or a FASTSCAN-B tip from Bruker Nano GmbH (Berlin, Germany). For AFM measurements a Nanowizard Ultra Speed2 from Bruker Nano GmbH (Berlin, Germany) was used. Images were analyzed with Gwyddion [179].

List of Publications and Manuscripts

[P1]: Nanoscale Organization of FasL on DNA Origami as Versatile Platform to Tune Apoptosis Signaling in Cells

Ricarda M. L. Berger, Johann M. Weck, Simon Kempe, Tim Liedl, Joachim O. Rädler, Cornelia Monzel*, and Amelie Heuer-Jungemann*

Advanced Materials, 2020, tbs

[P2]: DNA Binds to a Specific Site of the Adhesive Blood-Protein von Willebrand Factor Guided by Electrostatic Interactions

Angelica Sandoval-Perez, Ricarda M. L. Berger, Maria A. Brehm, Gesa König, Stefan W. Schneider, Volker Huck, Joachim O. Rädler, Camilo Aponte-Santamaria *Nucleic Acids Research*, 2020, in revision

[P3]: DNA Origami Nano-Sheets and Nano-Rods Alter the Orientational Order in a Lyotropic Chromonic Liquid Crystal

Bingru Zhang, Kevin Martens, Luisa Kneer, Timon Funck, Linh Nguyen, Ricarda Berger, Mihir Dass, Susanne Kempter, Jürgen Schmidtke, Tim Liedl, Heinz-Siegfried Kitzerow *The Journal of Physical Chemistry*, 2020, submitted

[M1]: Validation of Fluorescence Correlation Spectroscopy as a Binding Assay for the Evaluation of Ligand Binding Kinetics to Living Cells and its Potential for Drug Discovery

Ricarda M. L. Berger, Monika Herrmann, Karl-Peter Hopfner, Joachim O. Rädler

[M2]: Avidity of Multivalent DNA Binding to DNA Origami

Ricarda M. L. Berger, Maximilian Voggenthaler, Eugene Petrov, Tim Liedl, Joachim O. Rädler

List of Figures

2.1. Schematic illustration of a multivalency interaction	8
2.2. Schematic illustration of DNA and DNA origami	15
2.3. Multidomain VWF structure with A1 domain	17
2.4. Schematic illustration FasL-FasR interaction	18
3.1. Overview of Binding Methods	28
4.1. DNA origami functionalized with FasL	35
4.2. FasL apoptosis induction	37
4.3. Distance dependency of FasL apoptosis induction	39
4.4. High apoptotic potency for low FasL nanoagent concentrations	41
5.1. Ligand depletion illustration and estimation	47
5.2. Flow cytometry characterization of Alexa 488 antibody binding to induced HEK-293 cells	48
5.3. Characterization of Alexa 488 antibody in different buffers	49
5.4. FCS set-ups for depletion measurements	50
5.5. Membrane insert FCS cell measurements	52
5.6. Hydrogel FCS cell measurements	53
6.1. Schematic illustration of the multivalency model system	58
6.2. Characterization of bivalent model system	60
6.3. Characterization of the tetravalent model system	63
6.4. Avidity as a function of basepairing	65
6.5. Theoretical estimation of bivalent hybridization	67
7.1. Electrostatics influence the A1 domain DNA interaction	72
7.2. VWF multimer binding to dsDNA is shear-stress sensitive and sequence independent.	74

7.3. Binding of dsDNA to VWF Dimer analyzed by EMSA at various salt concentrations	76
A.1. Evaluation of FasL arrangement on DNA origami with AFM	93
A.2. At ionic strength of 80 mM binding of DNA and Dimer is inhibited . . .	94
A.3. Binding of ssDNA to VWF Dimer analyzed by EMSA	95
A.4. No Binding of 16 bp short DNA to VWF analyzed by EMSA	95
A.5. Multivalent DNA origami receptor	96
A.6. Agarose purification of Holliday Junction	96
A.7. Binding measurements with MST	97

List of Abbreviations

A adenine

AB antibody

AC autocorrelation curve

AFM Atomic Force Microscopy

APD avalanche photodiode

BD Brownian Dynamics simulations

C cytosine

CD Cluster of Differentiation

COVID-19 coronavirus disease 2019

CRD cysteine rich domain

DBCO dibenzocyclooctyne, also DIBO

DD death domain

DISC death inducing signaling complex

DNA deoxyribonucleic acid

dsDNA double stranded DNA

ELISA enzyme-linked immunosorbent assay

EMA European Medicines Agency

EMSA electrophoretic mobility shift assay

FADD Fas-associated death domain

FasL Fas ligand, also CD95 ligand

FasR Fas receptor, also CD95 and APO-1

FCS Fluorescence Correlation Spectroscopy

FJC freely jointed chain

FRET Fluorescence Resonance Energy Transfer

G guanine

HEK human embryonic kidney cells

HeLa name for a type of human cervical cancer cells

HIV human immunodeficiency virus

HJ Holliday Junction

Holli tetravalent Holliday Junction

hu humanized

ITC Isothermal Titration Calorimetry

Ig immunoglobulin

MD Molecular Dynamics simulations

MST Microscale Thermophoresis

mv monovalent

NaCl sodium chloride

NET neutrophil extracellular traps

NN nearest neighbor

PAINT point accumulation for imaging in nanoscale topography

PBS Phosphate Buffered Saline

SARS severe acute respiratory syndrome

SARS-CoV-2 Severe acute respiratory syndrome coronavirus 2, virus strain that caused pandemic in 2020

SPR Surface Plasmon Resonance

ssDNA single stranded DNA

T thymine

TA buffer with Tris base and acetic acid

TAE buffer with Tris base, acetic acid and EDTA

TIRF Total Internal Reflection Fluorescence Microscopy

TNF tumor necrosis factor

TRAIL TNF-related apoptosis-inducing ligand

VWF von Willebrand factor

WHO World Health Organization

WLC worm like chain

wt wildtype

Bibliography

1. Lupia, T., S. Scabini, S. Mornese Pinna, G. Di Perri, F. G. De Rosa, and S. Corcione, 2020. 2019 novel coronavirus (2019-nCoV) outbreak: A new challenge. *J Glob Antimicrob Resist* 21:22–27. <https://www.ncbi.nlm.nih.gov/pubmed/32156648>.
2. Chang, L., Y. Yan, and L. Wang, 2020. Coronavirus Disease 2019: Coronaviruses and Blood Safety. *Transfus Med Rev* <https://www.ncbi.nlm.nih.gov/pubmed/32107119>.
3. Ibrahim, I. M., D. H. Abdelmalek, M. E. Elshahat, and A. A. Elfiky, 2020. COVID-19 spike-host cell receptor GRP78 binding site prediction. *J Infect* <https://www.ncbi.nlm.nih.gov/pubmed/32169481>.
4. Belouzard, S., J. K. Millet, B. N. Licitra, and G. R. Whittaker, 2012. Mechanisms of coronavirus cell entry mediated by the viral spike protein. *Viruses* 4:1011–33. <https://www.ncbi.nlm.nih.gov/pubmed/22816037>.
5. Marsh, M., and A. Helenius, 2006. Virus Entry: Open Sesame. *Cell* 124:729–740.
6. Mammen, M., S.-K. Choi, and G. M. Whitesides, 1998. Polyvalent Interactions in Biological Systems: Implications for Design and Use of Multivalent Ligands and Inhibitors. *Angewandte Chemie International Edition* 37:2754–2794. [http://dx.doi.org/10.1002/\(SICI\)1521-3773\(19981102\)37:20<2754::AID-ANIE2754>3.0.CO;2-3](http://dx.doi.org/10.1002/(SICI)1521-3773(19981102)37:20<2754::AID-ANIE2754>3.0.CO;2-3).
7. Delguste, M., C. Zeippen, B. Machiels, J. Mast, L. Gillet, and D. Alsteens, 2018. Multivalent binding of herpesvirus to living cells is tightly regulated during infection. *Science Advances* 4:eaat1273. <https://advances.sciencemag.org/content/advances/4/8/eaat1273.full.pdf>.
8. .

9. Eisen, H. N., and F. Karush, 1949. The Interaction of Purified Antibody with Homologous Hapten. Antibody Valence and Binding Constant. *Journal of the American Chemical Society* 71:363–364. <https://doi.org/10.1021/ja01169a505>.
10. Hornick, C. L., and F. Karush, 1972. Antibody affinity III the role of multivalence. *Immunochemistry* 9:325–340. <http://www.sciencedirect.com/science/article/pii/0019279172900961>.
11. Ehrlich, P. H., 1979. The effect of multivalency on the specificity of protein and cell interactions. *Journal of Theoretical Biology* 81:123–127. <http://www.sciencedirect.com/science/article/pii/0022519379900857>.
12. Tjandra, K. C., and P. Thordarson, 2019. Multivalency in Drug Delivery-When Is It Too Much of a Good Thing? *Bioconjug Chem* 30:503–514. <https://www.ncbi.nlm.nih.gov/pubmed/30742420>.
13. Karush, F., 1978. The Affinity of Antibody: Range, Variability, and the Role of Multivalence, Springer US, Boston, MA, 85–116. https://doi.org/10.1007/978-1-4684-0805-8_3.
14. Carlson, C. B., P. Mowery, R. M. Owen, E. C. Dykhuizen, and L. L. Kiessling, 2007. Selective Tumor Cell Targeting Using Low-Affinity, Multivalent Interactions. *ACS Chemical Biology* 2:119–127. <https://doi.org/10.1021/cb6003788>.
15. Weiner, L. M., J. C. Murray, and C. W. Shuptrine, 2012. Antibody-based immunotherapy of cancer. *Cell* 148:1081–4. <http://www.ncbi.nlm.nih.gov/pubmed/22424219>.
16. Smith, D., V. Schueller, C. Engst, J. Radler, and T. Liedl, 2013. Nucleic acid nanostructures for biomedical applications. *Nanomedicine (Lond)* 8:105–21.
17. Surana, S., A. R. Shenoy, and Y. Krishnan, 2015. Designing DNA nanodevices for compatibility with the immune system of higher organisms. *Nat Nanotechnol* 10:741–7. <https://www.ncbi.nlm.nih.gov/pubmed/26329110>.
18. Yin, F., M. Li, X. Mao, F. Li, X. Xiang, Q. Li, L. Wang, X. Zuo, C. Fan, and Y. Zhu, 2020. DNA framework-based topological cell sorters. *Angewandte Chemie International Edition* .
19. Veneziano, R., T. J. Moyer, M. B. Stone, T. R. Shepherd, W. R. Schief, D. J. Irvine, and M. Bathe, 2020. Role of nanoscale antigen organization on B-cell activation

- probed using DNA origami. *bioRxiv* 2020.02.16.951475. <https://www.biorxiv.org/content/biorxiv/early/2020/02/17/2020.02.16.951475.full.pdf>.
20. Gulculer Balta, G. S., C. Monzel, S. Kleber, J. Beaudouin, E. Balta, T. Kaindl, S. Chen, L. Gao, M. Thiemann, C. R. Wirtz, Y. Samstag, M. Tanaka, and A. Martin-Villalba, 2019. 3D Cellular Architecture Modulates Tyrosine Kinase Activity, Thereby Switching CD95-Mediated Apoptosis to Survival. *Cell Rep* 29:2295–2306 e6. <https://www.ncbi.nlm.nih.gov/pubmed/31747602>.
 21. Brinkmann, V., U. Reichard, C. Goosmann, B. Fauler, Y. Uhlemann, D. S. Weiss, Y. Weinrauch, and A. Zychlinsky, 2004. Neutrophil Extracellular Traps Kill Bacteria. *Science* 303:1532–1535. <https://science.sciencemag.org/content/sci/303/5663/1532.full.pdf>.
 22. Bevilacqua, M. P., S. Stengelin, M. A. Gimbrone, and B. Seed, 1989. Endothelial Leukocyte Adhesion Molecule 1: An Inducible Receptor for Neutrophils Related to Complement Regulatory Proteins and Lectins. *Science* 243:1160–1165. www.jstor.org/stable/1702833.
 23. Grassle, S., V. Huck, K. I. Pappelbaum, C. Gorzelanny, C. Aponte-Santamaria, C. Baldauf, F. Grater, R. Schneppenheim, T. Obser, and S. W. Schneider, 2014. von Willebrand factor directly interacts with DNA from neutrophil extracellular traps. *Arterioscler Thromb Vasc Biol* 34:1382–9. <https://www.ncbi.nlm.nih.gov/pubmed/24790143>.
 24. Bianconi, E., A. Piovesan, F. Facchin, A. Beraudi, R. Casadei, F. Frabetti, L. Vitale, M. C. Pelleri, S. Tassani, F. Piva, S. Perez-Amodio, P. Strippoli, and S. Canaider, 2013. An estimation of the number of cells in the human body. *Annals of Human Biology* 40:463–471. <https://doi.org/10.3109/03014460.2013.807878>.
 25. Nelson, P., 2004. Biological physics. WH Freeman New York.
 26. Vauquelin, G., and S. J. Charlton, 2013. Exploring avidity: understanding the potential gains in functional affinity and target residence time of bivalent and heterobivalent ligands. *Br J Pharmacol* 168:1771–85. <https://www.ncbi.nlm.nih.gov/pubmed/23330947>.
 27. Sulzer, B., and A. S. Perelson, 1996. Equilibrium binding of multivalent ligands to cells: effects of cell and receptor density. *Math Biosci* 135:147–85.

28. Kitov, P. I., and D. R. Bundle, 2003. On the nature of the multivalency effect: a thermodynamic model. *J Am Chem Soc* 125:16271–84.
29. Phillips, R., J. Kondev, J. Theriot, N. Orme, and H. Garcia, 2009. Physical biology of the cell. Garland Science New York.
30. Jacobson, H., and W. H. Stockmayer, 1950. Intramolecular Reaction in Polycondensations. I. The Theory of Linear Systems. *The Journal of Chemical Physics* 18:1600–1606. <https://aip.scitation.org/doi/abs/10.1063/1.1747547>.
31. Crothers, D. M., and H. Metzger, 1972. The influence of polyvalency on the binding properties of antibodies. *Immunochemistry* 9:341–357. <http://www.sciencedirect.com/science/article/pii/0019279172900973>.
32. Kaufman, E. N., and R. K. Jain, 1992. Effect of bivalent interaction upon apparent antibody affinity: experimental confirmation of theory using fluorescence photobleaching and implications for antibody binding assays. *Cancer Res* 52:4157–67.
33. Plueckthun, A., and P. Pack, 1997. New protein engineering approaches to multivalent and bispecific antibody fragments. *Immunotechnology* 3:83–105. <http://www.sciencedirect.com/science/article/pii/S1380293397000675>.
34. Diestler, D. J., and E. W. Knapp, 2010. Statistical Mechanics of the Stability of Multivalent Ligand–Receptor Complexes. *The Journal of Physical Chemistry C* 114:5287–5304. <https://doi.org/10.1021/jp904258c>.
35. Liese, S., and R. R. Netz, 2015. Influence of length and flexibility of spacers on the binding affinity of divalent ligands. *Beilstein J Org Chem* 11:804–16. <https://www.ncbi.nlm.nih.gov/pubmed/26124882>.
36. Bandlow, V., S. Liese, D. Lauster, K. Ludwig, R. R. Netz, A. Herrmann, and O. Seitz, 2017. Spatial Screening of Hemagglutinin on Influenza A Virus Particles: Sialyl-LacNAc Displays on DNA and PEG Scaffolds Reveal the Requirements for Bivalency Enhanced Interactions with Weak Monovalent Binders. *J Am Chem Soc* 139:16389–16397. <https://www.ncbi.nlm.nih.gov/pubmed/29052990>.
37. Mattes, M. J., 2005. Binding parameters of antibodies: pseudo-affinity and other misconceptions. *Cancer Immunol Immunother* 54:513–6.

38. Martinez-Veracoechea, F. J., and D. Frenkel, 2011. Designing super selectivity in multivalent nano-particle binding. *Proc Natl Acad Sci U S A* 108:10963–8. <https://www.ncbi.nlm.nih.gov/pubmed/21690358>.
39. Huskens, J., L. Prins, R. Haag, and J. Ravoo, 2018. Multivalency: Concepts, Research and Applications. Wiley. <https://books.google.de/books?id=hKJFDwAAQBAJ>.
40. Dahm, R., 2005. Friedrich Miescher and the discovery of DNA. *Developmental Biology* 278:274–288. <http://www.sciencedirect.com/science/article/pii/S0012160604008231>.
41. Frixione, E., and L. Ruiz-Zamarripa, 2019. The "scientific catastrophe" in nucleic acids research that boosted molecular biology. *The Journal of biological chemistry* 294:2249–2255. <https://www.ncbi.nlm.nih.gov/pubmed/30765511><https://www.ncbi.nlm.nih.gov/pmc/articles/PMC6378961/>.
42. Watson, J. D., and F. H. C. Crick, 1953. Molecular Structure of Nucleic Acids: A Structure for Deoxyribose Nucleic Acid. *Nature* 171:737–738. <https://doi.org/10.1038/171737a0>.
43. SantaLucia, J., 1998. A unified view of polymer, dumbbell, and oligonucleotide DNA nearest-neighbor thermodynamics. *Proceedings of the National Academy of Sciences* 95:1460–1465. <https://www.pnas.org/content/pnas/95/4/1460.full.pdf>.
44. John SantaLucia, J., and D. Hicks, 2004. The Thermodynamics of DNA Structural Motifs. *Annual Review of Biophysics and Biomolecular Structure* 33:415–440. <https://www.annualreviews.org/doi/abs/10.1146/annurev.biophys.32.110601.141800>.
45. Zuker, M., 2003. Mfold web server for nucleic acid folding and hybridization prediction. *Nucleic Acids Res* 31:3406–15. <https://www.ncbi.nlm.nih.gov/pubmed/12824337>.
46. Cantor, C., and P. Schimmel, 1980. Biophysical Chemistry: Part III: The Behavior of Biological Macromolecules. W. H. Freeman. <https://books.google.de/books?id=fwMSmJlhUfsC>.
47. Brinkers, S., H. R. Dietrich, F. H. de Groote, I. T. Young, and B. Rieger, 2009. The persistence length of double stranded DNA determined using dark field tethered particle motion. *J Chem Phys* 130:215105. <http://www.ncbi.nlm.nih.gov/pubmed/19508104>.

48. Hagerman, P. J., 1988. Flexibility of DNA. *Annual Review of Biophysics and Biophysical Chemistry* 17:265–286. <http://www.annualreviews.org/doi/abs/10.1146/annurev.bb.17.060188.001405>.
49. Porschke, D., 1991. Persistence length and bending dynamics of DNA from electrooptical measurements at high salt concentrations. *Biophysical Chemistry* 40:169–179. <http://www.sciencedirect.com/science/article/pii/030146229187006Q>.
50. Wang, M. D., H. Yin, R. Landick, J. Gelles, and S. M. Block. Stretching DNA with optical tweezers. *Biophysical Journal* 72:1335–1346. [http://dx.doi.org/10.1016/S0006-3495\(97\)78780-0](http://dx.doi.org/10.1016/S0006-3495(97)78780-0).
51. Valle, F., M. Favre, P. De Los Rios, A. Rosa, and G. Dietler, 2005. Scaling Exponents and Probability Distributions of DNA End-to-End Distance. *Physical Review Letters* 95:158105. <http://link.aps.org/doi/10.1103/PhysRevLett.95.158105>.
52. Valle, F., M. Favre, P. De Los Rios, A. Rosa, and G. Dietler, 2005. Scaling exponents and probability distributions of DNA end-to-end distance. *Phys Rev Lett* 95:158105. <http://www.ncbi.nlm.nih.gov/pubmed/16241768>.
53. Tinland, B., A. Pluen, J. Sturm, and G. Weill, 1997. Persistence Length of Single-Stranded DNA. *Macromolecules* 30:5763–5765. <http://dx.doi.org/10.1021/ma970381+>.
54. Roth, E., A. Glick Azaria, O. Girshevitz, A. Bitler, and Y. Garini, 2018. Measuring the Conformation and Persistence Length of Single-Stranded DNA Using a DNA Origami Structure. *Nano Letters* 18:6703–6709. <https://doi.org/10.1021/acs.nanolett.8b02093>.
55. Rubinstein, M., and R. Colby, 2003. Polymer Physics. OUP Oxford. <https://books.google.de/books?id=RHksknEQYsYC>.
56. Seeman, N. C., 1982. Nucleic acid junctions and lattices. *J Theor Biol* 99:237–47.
57. Rothmund, P. W. K., 2006. Folding DNA to create nanoscale shapes and patterns. *Nature* 440:297–302. <https://doi.org/10.1038/nature04586>.
58. Douglas, S. M., H. Dietz, T. Liedl, B. Hogberg, F. Graf, and W. M. Shih, 2009. Self-assembly of DNA into nanoscale three-dimensional shapes. *Nature* 459:414–8. <https://www.ncbi.nlm.nih.gov/pubmed/19458720>.

59. Schnitzbauer, J., M. T. Strauss, T. Schlichthaerle, F. Schueder, and R. Jungmann, 2017. Super-resolution microscopy with DNA-PAINT. *Nat Protoc* 12:1198–1228. <https://www.ncbi.nlm.nih.gov/pubmed/28518172>.
60. Hariadi, R. F., M. Cale, and S. Sivaramakrishnan, 2014. Myosin lever arm directs collective motion on cellular actin network. *Proc Natl Acad Sci U S A* 111:4091–6. <http://www.ncbi.nlm.nih.gov/pubmed/24591646>.
61. Schueller, V. J., S. Heidegger, N. Sandholzer, P. C. Nickels, N. A. Suhartha, S. Endres, C. Bourquin, and T. Liedl, 2011. Cellular Immunostimulation by CpG-Sequence-Coated DNA Origami Structures. *ACS Nano* 5:9696–9702. <http://dx.doi.org/10.1021/nn203161y>.
62. Sellner, S., S. Kocabey, K. Nekolla, F. Krombach, T. Liedl, and M. Rehberg, 2015. DNA nanotubes as intracellular delivery vehicles in vivo. *Biomaterials* 53:453–63. <http://www.ncbi.nlm.nih.gov/pubmed/25890742>.
63. Douglas, S. M., I. Bachelet, and G. M. Church, 2012. A logic-gated nanorobot for targeted transport of molecular payloads. *Science* 335:831–4. <http://www.ncbi.nlm.nih.gov/pubmed/22344439>.
64. Denis, C., D. Baruch, C. M. Kielty, N. Ajzenberg, O. Christophe, and D. Meyer, 1993. Localization of von Willebrand factor binding domains to endothelial extracellular matrix and to type VI collagen. *Arterioscler Thromb* 13:398–406.
65. Rack, K., V. Huck, M. Hoore, D. A. Fedosov, S. W. Schneider, and G. Gompper, 2017. Margination and stretching of von Willebrand factor in the blood stream enable adhesion. *Sci Rep* 7:14278. <https://www.ncbi.nlm.nih.gov/pubmed/29079767>.
66. Lenting, P. J., C. Casari, O. D. Christophe, and C. V. Denis, 2012. von Willebrand factor: the old, the new and the unknown. *J Thromb Haemost* 10:2428–37. <https://www.ncbi.nlm.nih.gov/pubmed/23020315>.
67. Kolaczkowska, E., C. N. Jenne, B. G. Surewaard, A. Thanabalasuriar, W. Y. Lee, M. J. Sanz, K. Mowen, G. Opdenakker, and P. Kubes, 2015. Molecular mechanisms of NET formation and degradation revealed by intravital imaging in the liver vasculature. *Nat Commun* 6:6673. <https://www.ncbi.nlm.nih.gov/pubmed/25809117>.

68. Emsley, J., M. Cruz, R. Handin, and R. Liddington, 1998. Crystal structure of the von Willebrand Factor A1 domain and implications for the binding of platelet glycoprotein Ib. *J Biol Chem* 273:10396–401.
69. Lippok, S., T. Obser, J. P. Muller, V. K. Stierle, M. Benoit, U. Budde, R. Schneppenheim, and J. O. Radler, 2013. Exponential size distribution of von Willebrand factor. *Biophys J* 105:1208–16. <https://www.ncbi.nlm.nih.gov/pubmed/24010664>.
70. Springer, T. A., 2011. Biology and physics of von Willebrand factor concatamers. *J Thromb Haemost* 9 Suppl 1:130–43. <https://www.ncbi.nlm.nih.gov/pubmed/21781248>.
71. Schneider, S. W., S. Nuschele, A. Wixforth, C. Gorzelanny, A. Alexander-Katz, R. R. Netz, and M. F. Schneider, 2007. Shear-induced unfolding triggers adhesion of von Willebrand factor fibers. *Proc Natl Acad Sci U S A* 104:7899–903. <https://www.ncbi.nlm.nih.gov/pubmed/17470810>.
72. Fu, H., Y. Jiang, D. Yang, F. Scheiflinger, W. P. Wong, and T. A. Springer, 2017. Flow-induced elongation of von Willebrand factor precedes tension-dependent activation. *Nat Commun* 8:324. <https://www.ncbi.nlm.nih.gov/pubmed/28831047>.
73. Gogia, S., and S. Neelamegham, 2015. Role of fluid shear stress in regulating VWF structure, function and related blood disorders. *Biorheology* 52:319–335. <https://pubmed.ncbi.nlm.nih.gov/26600266><https://www.ncbi.nlm.nih.gov/pmc/articles/PMC4927820/>.
74. Dong, J., P. Ye, A. J. Schade, S. Gao, G. M. Romo, N. T. Turner, L. V. McIntire, and J. A. Lopez, 2001. Tyrosine sulfation of glycoprotein I(b)alpha. Role of electrostatic interactions in von Willebrand factor binding. *J Biol Chem* 276:16690–4. <https://www.ncbi.nlm.nih.gov/pubmed/11279169>.
75. Jiang, Y., H. Fu, T. A. Springer, and W. P. Wong, 2019. Electrostatic Steering Enables Flow-Activated Von Willebrand Factor to Bind Platelet Glycoprotein, Revealed by Single-Molecule Stretching and Imaging. *J Mol Biol* 431:1380–1396. <https://www.ncbi.nlm.nih.gov/pubmed/30797858>.
76. Ward, C. M., T. J. Tetaz, R. K. Andrews, and M. C. Berndt, 1997. BINDING OF THE VON WILLEBRAND FACTOR A1 DOMAIN TO HISTONE. *Thrombosis Research* 86:469–477. <http://www.sciencedirect.com/science/article/pii/S0049384897000960>.

77. Bodmer, J.-L., P. Schneider, and J. Tschopp, 2002. The molecular architecture of the TNF superfamily. *Trends in Biochemical Sciences* 27:19–26. <http://www.sciencedirect.com/science/article/pii/S0968000401019958>.
78. Aggarwal, B. B., 2003. Signalling pathways of the TNF superfamily: a double-edged sword. *Nat Rev Immunol* 3:745–56. <https://www.ncbi.nlm.nih.gov/pubmed/12949498>.
79. Vanamee, E. S., and D. L. Faustman, 2018. Structural principles of tumor necrosis factor superfamily signaling. *Sci Signal* 11.
80. Scott, F. L., B. Stec, C. Pop, M. K. Dobaczewska, J. J. Lee, E. Monosov, H. Robinson, G. S. Salvesen, R. Schwarzenbacher, and S. J. Riedl, 2009. The Fas-FADD death domain complex structure unravels signalling by receptor clustering. *Nature* 457:1019–22. <https://www.ncbi.nlm.nih.gov/pubmed/19118384>.
81. Schneider, P., N. Holler, J. L. Bodmer, M. Hahne, K. Frei, A. Fontana, and J. Tschopp, 1998. Conversion of membrane-bound Fas(CD95) ligand to its soluble form is associated with downregulation of its proapoptotic activity and loss of liver toxicity. *The Journal of experimental medicine* 187:1205–1213. <https://www.ncbi.nlm.nih.gov/pubmed/9547332><https://www.ncbi.nlm.nih.gov/pmc/articles/PMC2212219/>.
82. Holler, N., A. Tardivel, M. Kovacsovics-Bankowski, S. Hertig, O. Gaide, F. Martinon, A. Tinel, D. Deperthes, S. Calderara, T. Schulthess, J. Engel, P. Schneider, and J. Tschopp, 2003. Two Adjacent Trimeric Fas Ligands Are Required for Fas Signaling and Formation of a Death-Inducing Signaling Complex. *Molecular and Cellular Biology* 23:1428–1440.
83. Zhang, N., Y. Yang, Z. Wang, J. Yang, X. Chu, J. Liu, and Y. Zhao, 2019. Polypeptide-engineered DNA tetrahedrons for targeting treatment of colorectal cancer via apoptosis and autophagy. *J Control Release* 309:48–58. <https://www.ncbi.nlm.nih.gov/pubmed/31301339>.
84. Peter, M. E., and P. H. Krammer, 2003. The CD95(APO-1/Fas) DISC and beyond. *Cell Death Differ* 10:26–35.
85. Peter, M. E., A. Hadji, A. E. Murmann, S. Brockway, W. Putzbach, A. Pattanayak, and P. Ceppi, 2015. The role of CD95 and CD95 ligand in cancer. *Cell Death Differ* 22:549–59. <https://www.ncbi.nlm.nih.gov/pubmed/25656654>.

86. Algeciras-Schimmich, A., L. Shen, B. C. Barnhart, A. E. Murmann, J. K. Burkhardt, and M. E. Peter, 2002. Molecular ordering of the initial signaling events of CD95. *Mol Cell Biol* 22:207–20. <https://www.ncbi.nlm.nih.gov/pubmed/11739735>.
87. Pan, L., T. M. Fu, W. Zhao, L. Zhao, W. Chen, C. Qiu, W. Liu, Z. Liu, A. Piai, Q. Fu, S. Chen, H. Wu, and J. J. Chou, 2019. Higher-Order Clustering of the Transmembrane Anchor of DR5 Drives Signaling. *Cell* 176:1477–1489 e14. <https://www.ncbi.nlm.nih.gov/pubmed/30827683>.
88. Fitzpatrick, J. A., and B. F. Lillemeier, 2011. Fluorescence correlation spectroscopy: linking molecular dynamics to biological function in vitro and in situ. *Curr Opin Struct Biol* 21:650–60. <http://www.ncbi.nlm.nih.gov/pubmed/21767945>.
89. Dietz, M. S., F. Fricke, C. L. Krueger, H. H. Niemann, and M. Heilemann, 2014. Receptor-Ligand Interactions: Binding Affinities Studied by Single-Molecule and Super-Resolution Microscopy on Intact Cells. *ChemPhysChem* 15:671–676.
90. Tiwari, M., S. Mikuni, H. Muto, and M. Kinjo, 2013. Determination of dissociation constant of the NFkappaB p50/p65 heterodimer using fluorescence cross-correlation spectroscopy in the living cell. *Biochem Biophys Res Commun* 436:430–5. <http://www.ncbi.nlm.nih.gov/pubmed/23751347>.
91. Woell, D., 2014. Fluorescence correlation spectroscopy in polymer science. *RSC Adv.* 4:2447–2465.
92. Schwille, P., and E. Haustein, 2001. Fluorescence Correlation Spectroscopy - An Introduction to its Concepts and Applications. *Spectroscopy* 94(22).
93. Lakowicz, J. R., 2006. Principles of fluorescence spectroscopy,. Springer-Verlag, 3rd edition edition. <http://dx.doi.org/10.1007/s00216-007-1822-x>.
94. Schwille, P., and E. Haustein, 2006. Fluorescence Correlation Spectroscopy - An Introduction to its Concepts and Applications. Report. <http://dx.doi.org/10.1002/lpor.200910041>.
95. Einstein, A., 1905. Ueber die von der molekularkinetischen Theorie der Waerme geforderte Bewegung von in ruhenden Fluessigkeiten suspendierten Teilchen. *Annalen der Physik* 322:549–560. <https://onlinelibrary.wiley.com/doi/abs/10.1002/andp.19053220806>.

96. von Smoluchowski, M., 1906. Zur kinetischen Theorie der Brownschen Molekularbewegung und der Suspensionen. *Annalen der Physik* 326:756–780. <https://onlinelibrary.wiley.com/doi/abs/10.1002/andp.19063261405>.
97. Stokes, G. G., 2009. On the Effect of the Internal Friction of Fluids on the Motion of Pendulums, Cambridge University Press, Cambridge, volume 3 of *Cambridge Library Collection - Mathematics*, 1–10. <https://www.cambridge.org/core/books/mathematical-and-physical-papers/on-the-effect-of-the-internal-friction-of-fluids-on-the-motion-of-pendulums/11038EBC1E2D897D9E5B1297C9AE5D99>.
98. Berg, H., 1993. Random Walks in Biology. Princeton University Press. <https://books.google.de/books?id=DjdgXGLoJY8C>.
99. Tirado, M. M., C. L. Martinez, and J. G. d. l. Torre, 1984. Comparison of theories for the translational and rotational diffusion coefficients of rodlike macromolecules. Application to short DNA fragments. *The Journal of Chemical Physics* 81:2047–2052. <https://aip.scitation.org/doi/abs/10.1063/1.447827>.
100. Widengren, J., R. Rigler, and Å. Mets, 1994. Triplet-state monitoring by fluorescence correlation spectroscopy. *Journal of Fluorescence* 4:255–258. <https://doi.org/10.1007/BF01878460>.
101. Bernard, J., L. Fleury, H. Talon, and M. Orrit, 1993. Photon bunching in the fluorescence from single molecules: A probe for intersystem crossing. *The Journal of Chemical Physics* 98:850.
102. Ludwig, C., K. H.-u. Staatsdruckerei, K. A. d. W. i. Wien, and Braumueller, 1856. Diffusion zwischen ungleich erwaermten Orten gleich zusammengesetzter Loesung. Aus der K.K. Hof- und Staatsdruckerei, in Commission bei W. Braumueller, Buchhaendler des K.K. Hofes und der K. Akademie der Wissenschaften. <https://books.google.de/books?id=iykXSQAACAAJ>.
103. Goldhirsch, I., and D. Ronis, 1983. Theory of thermophoresis. I. General considerations and mode-coupling analysis. *Phys. Rev. A* 27.
104. Fick, A., 1855. Ueber Diffusion. *Annalen der Physik* 170:59–86. <https://onlinelibrary.wiley.com/doi/abs/10.1002/andp.18551700105>.

105. Duhr, S., and D. Braun, 2006. Why molecules move along a temperature gradient. *Proc Natl Acad Sci U S A* 103:19678–82. <https://www.ncbi.nlm.nih.gov/pubmed/17164337>.
106. Seidel, S. A., P. M. Dijkman, W. A. Lea, G. van den Bogaart, M. Jerabek-Willemsen, A. Lazic, J. S. Joseph, P. Srinivasan, P. Baaske, A. Simeonov, I. Katritch, F. A. Melo, J. E. Ladbury, G. Schreiber, A. Watts, D. Braun, and S. Duhr, 2013. Microscale thermophoresis quantifies biomolecular interactions under previously challenging conditions. *Methods* 59:301–15. <https://www.ncbi.nlm.nih.gov/pubmed/23270813>.
107. Jerabek-Willemsen, M., T. Andr  , R. Wanner, H. M. Roth, S. Duhr, P. Baaske, and D. Breitsprecher, 2014. MicroScale Thermophoresis: Interaction analysis and beyond. *Journal of Molecular Structure* 1077:101–113.
108. Hellman, L. M., and M. G. Fried, 2007. Electrophoretic mobility shift assay (EMSA) for detecting protein-nucleic acid interactions. *Nat Protoc* 2:1849–61. <https://www.ncbi.nlm.nih.gov/pubmed/17703195>.
109. Lumpkin, O. J., P. Dejardin, and B. H. Zimm, 1985. Theory of gel electrophoresis of DNA. *Biopolymers* 24:1573–93.
110. Viovy, J.-L., 1996. Reptation theories of electrophoresis. *Molecular Biotechnology* 6:31–46. <https://doi.org/10.1007/BF02762321>.
111. Slater, G. W., 2009. DNA gel electrophoresis: the reptation model(s). *Electrophoresis* 30 Suppl 1:S181–7. <https://www.ncbi.nlm.nih.gov/pubmed/19517509>.
112. Fried, M., and D. M. Crothers, 1981. Equilibria and kinetics of lac repressor-operator interactions by polyacrylamide gel electrophoresis. *Nucleic acids research* 9:6505–6525. <https://pubmed.ncbi.nlm.nih.gov/6275366><https://www.ncbi.nlm.nih.gov/pmc/articles/PMC327619/>.
113. Kessler, C., 1991. The digoxigenin:anti-digoxigenin (DIG) technology - a survey on the concept and realization of a novel bioanalytical indicator system. *Molecular and Cellular Probes* 5:161–205. <http://www.sciencedirect.com/science/article/pii/089085089190041H>.
114. Kocabey, S., S. Kempter, J. List, Y. Xing, W. Bae, D. Schiffels, W. M. Shih, F. C. Simmel, and T. Liedl, 2015. Membrane-Assisted Growth of DNA Origami Nanostructure Arrays. *ACS Nano* 9:3530–3539. <https://doi.org/10.1021/acsnano.5b00161>.

115. Kempter, S., A. Khmelinskaia, M. T. Strauss, P. Schwille, R. Jungmann, T. Liedl, and W. Bae, 2019. Single Particle Tracking and Super-Resolution Imaging of Membrane-Assisted Stop-and-Go Diffusion and Lattice Assembly of DNA Origami. *ACS Nano* 13:996–1002. <https://www.ncbi.nlm.nih.gov/pubmed/30588792>.
116. Puck, T. T., P. I. Marcus, and S. J. Cieciura, 1956. Clonal growth of mammalian cells in vitro; growth characteristics of colonies from single HeLa cells with and without a feeder layer. *J Exp Med* 103:273–83.
117. Liu, W., U. Ramagopal, H. Cheng, J. B. Bonanno, R. Toro, R. Bhosle, C. Zhan, and S. C. Almo, 2016. Crystal Structure of the Complex of Human FasL and Its Decoy Receptor DcR3. *Structure* 24:2016–2023. <https://www.ncbi.nlm.nih.gov/pubmed/27806260>.
118. Xie, J., and P. G. Schultz, 2006. A chemical toolkit for proteins—an expanded genetic code. *Nat Rev Mol Cell Biol* 7:775–82.
119. Liu, X., Y. Xu, T. Yu, C. Clifford, Y. Liu, H. Yan, and Y. Chang, 2012. A DNA nanostructure platform for directed assembly of synthetic vaccines. *Nano Lett* 12:4254–9. <https://www.ncbi.nlm.nih.gov/pubmed/22746330>.
120. Zimmerman, E. S., T. H. Heibeck, A. Gill, X. Li, C. J. Murray, M. R. Madlansacay, C. Tran, N. T. Uter, G. Yin, P. J. Rivers, A. Y. Yam, W. D. Wang, A. R. Steiner, S. U. Bajad, K. Penta, W. Yang, T. J. Hallam, C. D. Thanos, and A. K. Sato, 2014. Production of site-specific antibody-drug conjugates using optimized non-natural amino acids in a cell-free expression system. *Bioconjug Chem* 25:351–61. <https://www.ncbi.nlm.nih.gov/pubmed/24437342>.
121. Marks, I. S., J. S. Kang, B. T. Jones, K. J. Landmark, A. J. Cleland, and T. A. Taton, 2011. Strain-promoted "click" chemistry for terminal labeling of DNA. *Bioconjug Chem* 22:1259–63. <https://www.ncbi.nlm.nih.gov/pubmed/21539391>.
122. Orski, S. V., G. R. Sheppard, S. Arumugam, R. M. Arnold, V. V. Popik, and J. Locklin, 2012. Rate determination of azide click reactions onto alkyne polymer brush scaffolds: a comparison of conventional and catalyst-free cycloadditions for tunable surface modification. *Langmuir* 28:14693–702. <http://www.ncbi.nlm.nih.gov/pubmed/23009188>.
123. Vauquelin, G., 2016. Effects of target binding kinetics on in vivo drug efficacy: koff

- , kon and rebinding. *Br J Pharmacol* 173:2319–34. <https://www.ncbi.nlm.nih.gov/pubmed/27129075>.
124. Saunders, G. C., J. C. Martin, J. H. Jett, and A. Perkins, 1990. Flow cytometric competitive binding assay for determination of actinomycin-D concentrations. *Cytometry* 11:311–313. <http://dx.doi.org/10.1002/cyto.990110213>.
125. Forster, M. D., M. G. Ormerod, R. Agarwal, S. B. Kaye, and A. L. Jackman, 2007. Flow cytometric method for determining folate receptor expression on ovarian carcinoma cells. *Cytometry A* 71:945–50. <https://www.ncbi.nlm.nih.gov/pubmed/17712798>.
126. Black, C. B., T. D. Duensing, L. S. Trinkle, and R. T. Dunlay, 2011. Cell-based screening using high-throughput flow cytometry. *Assay Drug Dev Technol* 9:13–20. <https://www.ncbi.nlm.nih.gov/pubmed/21050072>.
127. Cedeno-Arias, M., J. Sanchez-Ramirez, R. Blanco-Santana, and E. Rengifo-Calzado, 2011. Validation of a flow cytometry based binding assay for evaluation of monoclonal antibody recognizing EGF receptor. *Sci Pharm* 79:569–81. <https://www.ncbi.nlm.nih.gov/pubmed/21886904>.
128. Patching, S. G., 2014. Surface plasmon resonance spectroscopy for characterisation of membrane protein-ligand interactions and its potential for drug discovery. *Biochim Biophys Acta* 1838:43–55. <https://www.ncbi.nlm.nih.gov/pubmed/23665295>.
129. Adam, G., P. Laeuger, and G. Stark, 2009. Physikalische Chemie und Biophysik. Springer Berlin Heidelberg. <https://books.google.de/books?id=iVAoBAAAQBAJ>.
130. Weidemann, T., R. Worch, K. Kurgonaite, M. Hintersteiner, C. Bokel, and P. Schwill, 2011. Single cell analysis of ligand binding and complex formation of interleukin-4 receptor subunits. *Biophys J* 101:2360–9. <https://www.ncbi.nlm.nih.gov/pubmed/22098734>.
131. Shi, X., Y. H. Foo, T. Sudhaharan, S. W. Chong, V. Korzh, S. Ahmed, and T. Wohland, 2009. Determination of dissociation constants in living zebrafish embryos with single wavelength fluorescence cross-correlation spectroscopy. *Biophys J* 97:678–86. <https://www.ncbi.nlm.nih.gov/pubmed/19619483>.
132. Sudhaharan, T., P. Liu, Y. H. Foo, W. Bu, K. B. Lim, T. Wohland, and S. Ahmed, 2009. Determination of in vivo dissociation constant, KD, of Cdc42-effector complexes in live mammalian cells using single wavelength fluorescence cross-correlation

- spectroscopy. *J Biol Chem* 284:13602–9. <https://www.ncbi.nlm.nih.gov/pubmed/19293156>.
133. Tiwari, M., S. Mikuni, H. Muto, and M. Kinjo, 2013. Determination of dissociation constant of the NFkappaB p50/p65 heterodimer using fluorescence cross-correlation spectroscopy in the living cell. *Biochem Biophys Res Commun* 436:430–5. <https://www.ncbi.nlm.nih.gov/pubmed/23751347>.
134. Ruttinger, S., V. Buschmann, B. Kramer, R. Erdmann, R. Macdonald, and F. Koberling, 2008. Comparison and accuracy of methods to determine the confocal volume for quantitative fluorescence correlation spectroscopy. *J Microsc* 232:343–52.
135. Dietrich, M., H. Le Roy, D. B. Bruckner, H. Engelke, R. Zantl, J. O. Radler, and C. P. Broedersz, 2018. Guiding 3D cell migration in deformed synthetic hydrogel microstructures. *Soft Matter* 14:2816–2826. <https://www.ncbi.nlm.nih.gov/pubmed/29595213>.
136. Bouchaud, J.-P., and A. Georges, 1990. Anomalous diffusion in disordered media: Statistical mechanisms, models and physical applications. *Physics Reports* 195:127–293. <http://www.sciencedirect.com/science/article/pii/037015739090099N>.
137. Banks, D. S., C. Tressler, R. D. Peters, F. Hofling, and C. Fradin, 2016. Characterizing anomalous diffusion in crowded polymer solutions and gels over five decades in time with variable-lengthscale fluorescence correlation spectroscopy. *Soft Matter* 12:4190–203. <https://www.ncbi.nlm.nih.gov/pubmed/27050290>.
138. Golden, A. P., and J. Tien, 2007. Fabrication of microfluidic hydrogels using molded gelatin as a sacrificial element. *Lab on a Chip* 7:720–725. <http://dx.doi.org/10.1039/B618409J>.
139. Comps-Agrar, L., D. Maurel, P. Rondard, J. P. Pin, E. Trinquet, and L. Prezeau, 2011. Cell-surface protein-protein interaction analysis with time-resolved FRET and snap-tag technologies: application to G protein-coupled receptor oligomerization. *Methods Mol Biol* 756:201–14.
140. Lentschat, A., V. T. El-Samalouti, J. Schletter, S. Kusumoto, L. Brade, E. T. Rietschel, J. Gerdes, M. Ernst, H. Flad, and A. J. Ulmer, 1999. The internalization time course of a given lipopolysaccharide chemotype does not correspond to its activation kinetics in monocytes. *Infection and immunity*

- 67:2515–2521. <https://pubmed.ncbi.nlm.nih.gov/10225915><https://www.ncbi.nlm.nih.gov/pmc/articles/PMC115998/>.
141. Wang, X., and J. C. Marvizon, 2002. Time-course of the internalization and recycling of neurokinin 1 receptors in rat dorsal horn neurons. *Brain Res* 944:239–47.
142. Ju, Y., Y. Liao, L. Zhang, Y. Sheng, Q. Zhang, D. Chen, Y. Cheng, Z. Xu, K. Sugioka, and K. Midorikawa, 2011. Fabrication of large-volume microfluidic chamber embedded in glass using three-dimensional femtosecond laser micromachining. *Microfluidics and Nanofluidics* 11:111–117. <https://doi.org/10.1007/s10404-011-0790-9>.
143. Sugioka, K., Y. Cheng, and K. Midorikawa, 2005. Three-dimensional micromachining of glass using femtosecond laser for lab-on-a-chip device manufacture. *Applied Physics A* 81:1–10. <https://doi.org/10.1007/s00339-005-3225-1>.
144. Zhang, J., K. Sugioka, and K. Midorikawa, 1998. High-speed machining of glass materials by laser-induced plasma-assisted ablation using a 532-nm laser. *Applied Physics A* 67:499–501. <https://doi.org/10.1007/s003390050810>.
145. Zhao, Z., Y. Liu, and H. Yan, 2011. Organizing DNA origami tiles into larger structures using preformed scaffold frames. *Nano Lett* 11:2997–3002. <https://www.ncbi.nlm.nih.gov/pubmed/21682348>.
146. Ong, L. L., N. Hanikel, O. K. Yaghi, C. Grun, M. T. Strauss, P. Bron, J. Lai-Kee-Him, F. Schueder, B. Wang, P. Wang, J. Y. Kishi, C. Myhrvold, A. Zhu, R. Jungmann, G. Bellot, Y. Ke, and P. Yin, 2017. Programmable self-assembly of three-dimensional nanostructures from 10,000 unique components. *Nature* 552:72–77. <https://www.ncbi.nlm.nih.gov/pubmed/29219968>.
147. Wagenbauer, K. F., C. Sigl, and H. Dietz, 2017. Gigadalton-scale shape-programmable DNA assemblies. *Nature* 552:78–83. <https://www.ncbi.nlm.nih.gov/pubmed/29219966>.
148. Morrison, L. E., and L. M. Stols, 1993. Sensitive fluorescence-based thermodynamic and kinetic measurements of DNA hybridization in solution. *Biochemistry* 32:3095–104.
149. Strauss, M. T., F. Schueder, D. Haas, P. C. Nickels, and R. Jungmann, 2018. Quantifying absolute addressability in DNA origami with molecular resolution. *Nat Commun* 9:1600. <https://www.ncbi.nlm.nih.gov/pubmed/29686288>.

150. Rinker, S., Y. Ke, Y. Liu, R. Chhabra, and H. Yan, 2008. Self-assembled DNA nanostructures for distance-dependent multivalent ligand-protein binding. *Nat Nanotechnol* 3:418–22. <http://www.ncbi.nlm.nih.gov/pubmed/18654566>.
151. Shaw, A., V. Lundin, E. Petrova, F. Fordos, E. Benson, A. Al-Amin, A. Herland, A. Blokzijl, B. Hogberg, and A. I. Teixeira, 2014. Spatial control of membrane receptor function using ligand nanocalipers. *Nat Methods* 11:841–6. <http://www.ncbi.nlm.nih.gov/pubmed/24997862>.
152. Moser, C., J. S. Lorenz, M. Sajfutdinow, and D. M. Smith, 2018. Pinpointed Stimulation of EphA2 Receptors via DNA-Templated Oligovalence. *Int J Mol Sci* 19. <https://www.ncbi.nlm.nih.gov/pubmed/30404153>.
153. Lorenz, J. S., J. Schnauss, M. Glaser, M. Sajfutdinow, C. Schuldt, J. A. Kaes, and D. M. Smith, 2018. Synthetic Transient Crosslinks Program the Mechanics of Soft, Biopolymer-Based Materials. *Advanced Materials* 30:1706092.
154. Wagenbauer, K. F., F. A. S. Engelhardt, E. Stahl, V. K. Hecht, P. Stommer, F. Seebacher, L. Meregalli, P. Ketterer, T. Gerling, and H. Dietz, 2017. How We Make DNA Origami. *Chembiochem* 18:1873–1885.
155. Jungmann, R., C. Steinhauer, M. Scheible, A. Kuzyk, P. Tinnefeld, and F. C. Simmel, 2010. Single-molecule kinetics and super-resolution microscopy by fluorescence imaging of transient binding on DNA origami. *Nano Lett* 10:4756–61. <https://www.ncbi.nlm.nih.gov/pubmed/20957983>.
156. Jerabek-Willemsen, M., T. Andr  , R. Wanner, H. M. Roth, S. Duhr, P. Baaske, and D. Breitsprecher, 2014. MicroScale Thermophoresis: Interaction analysis and beyond. *Journal of Molecular Structure* 1077:101–113.
157. Xu, S., J. Zhan, B. Man, S. Jiang, W. Yue, S. Gao, C. Guo, H. Liu, Z. Li, J. Wang, and Y. Zhou, 2017. Real-time reliable determination of binding kinetics of DNA hybridization using a multi-channel graphene biosensor. *Nat Commun* 8:14902. <https://www.ncbi.nlm.nih.gov/pubmed/28322227>.
158. Netz, R. R., and J.-F. Joanny, 1999. Adsorption of Semiflexible Polyelectrolytes on Charged Planar Surfaces. Charge Compensation, Charge Reversal, and Multilayer Formation. *Macromolecules* 32:9013–9025. <https://doi.org/10.1021/ma990263h>.

159. Woo, S., and P. W. Rothmund, 2014. Self-assembly of two-dimensional DNA origami lattices using cation-controlled surface diffusion. *Nat Commun* 5:4889. <https://www.ncbi.nlm.nih.gov/pubmed/25205175>.
160. Bellot, G., M. A. McClintock, J. J. Chou, and W. M. Shih, 2013. DNA nanotubes for NMR structure determination of membrane proteins. *Nat Protoc* 8:755–70. <https://www.ncbi.nlm.nih.gov/pubmed/23518667>.
161. Lipfert, J., S. Doniach, R. Das, and D. Herschlag, 2014. Understanding nucleic acid-ion interactions. *Annu Rev Biochem* 83:813–41. <https://www.ncbi.nlm.nih.gov/pubmed/24606136>.
162. Mack, E. T., P. W. Snyder, R. Perez-Castillejos, B. Bilgicer, D. T. Moustakas, M. J. Butte, and G. M. Whitesides, 2012. Dependence of avidity on linker length for a bivalent ligand-bivalent receptor model system. *J Am Chem Soc* 134:333–45. <https://www.ncbi.nlm.nih.gov/pubmed/22088143>.
163. Krishnamoorthy, G. K., P. Alluvada, S. Hameed Mohammed Sherieff, T. Kwa, and J. Krishnamoorthy, 2020. Isothermal titration calorimetry and surface plasmon resonance analysis using the dynamic approach. *Biochem Biophys Rep* 21:100712.
164. Lippok, S., M. Radtke, T. Obser, L. Kleemeier, R. Schneppenheim, U. Budde, R. R. Netz, and J. O. Radler, 2016. Shear-Induced Unfolding and Enzymatic Cleavage of Full-Length VWF Multimers. *Biophys J* 110:545–554. <https://www.ncbi.nlm.nih.gov/pubmed/26840720>.
165. Huang, R. H., D. H. Fremont, J. L. Diener, R. G. Schaub, and J. E. Sadler, 2009. A structural explanation for the antithrombotic activity of ARC1172, a DNA aptamer that binds von Willebrand factor domain A1. *Structure* 17:1476–84. <https://www.ncbi.nlm.nih.gov/pubmed/19913482>.
166. Schneider, S., H. Oberleithner, H. Schillers, T. Goerge, R. Ossig, A. Barg, and M. Schneider, 2017. Soluble plasma-derived von Willebrand factor assembles to a haemostatically active filamentous network. *Thrombosis and Haemostasis* 97:514–526.
167. Ruggeri, Z. M., 1997. Mechanisms initiating platelet thrombus formation. *Thromb Haemost* 78:611–6.
168. Cruz, M. A., R. I. Handin, and R. J. Wise, 1993. The interaction of the von Willebrand factor-A1 domain with platelet glycoprotein Ib/IX. The role of glycosylation

- and disulfide bonding in a monomeric recombinant A1 domain protein. *J Biol Chem* 268:21238–45.
169. Cruz, M. A., H. Yuan, J. R. Lee, R. J. Wise, and R. I. Handin, 1995. Interaction of the von Willebrand factor (vWF) with collagen. Localization of the primary collagen-binding site by analysis of recombinant vWF a domain polypeptides. *J Biol Chem* 270:10822–7.
170. Federici, A. B., R. Bader, S. Pagani, M. L. Colibretti, L. De Marco, and P. M. Mannucci, 1989. Binding of von Willebrand factor to glycoproteins Ib and IIb/IIIa complex: affinity is related to multimeric size. *Br J Haematol* 73:93–9.
171. Morisato, D. K., and H. R. Gralnick, 1980. Selective binding of the factor VIII/von Willebrand factor protein to human platelets. *Blood* 55:9–15.
172. Kalafatis, M., Y. Takahashi, J. P. Girma, and D. Meyer, 1987. Localization of a collagen-interactive domain of human von Willebrand factor between amino acid residues Gly 911 and Glu 1,365. *Blood* 70:1577–83.
173. Pareti, F. I., K. Niiya, J. M. McPherson, and Z. M. Ruggeri, 1987. Isolation and characterization of two domains of human von Willebrand factor that interact with fibrillar collagen types I and III. *J Biol Chem* 262:13835–41.
174. Furlan, M., 1996. Von Willebrand factor: molecular size and functional activity. *Annals of Hematology* 72:341–348. <https://doi.org/10.1007/s002770050184>.
175. Fischer, R., J. Marsal, C. Gutta, S. A. Eisler, N. Peters, J. R. Bethea, K. Pfizenmaier, and R. E. Kontermann, 2017. Novel strategies to mimic transmembrane tumor necrosis factor-dependent activation of tumor necrosis factor receptor 2. *Sci Rep* 7:6607. <https://www.ncbi.nlm.nih.gov/pubmed/28747780>.
176. Schlichthaerle, T., M. T. Strauss, F. Schueder, A. Auer, B. Nijmeijer, M. Kueblbeck, V. Jimenez Sabinina, J. V. Thevathasan, J. Ries, J. Ellenberg, and R. Jungmann, 2019. Direct Visualization of Single Nuclear Pore Complex Proteins Using Genetically-Encoded Probes for DNA-PAINT. *Angewandte Chemie International Edition* 58:13004–13008. <https://onlinelibrary.wiley.com/doi/abs/10.1002/anie.201905685>.
177. Ma, Y., E. Pandzic, P. R. Nicovich, Y. Yamamoto, J. Kwiatek, S. V. Pagoon, A. Benda, J. Rossy, and K. Gaus, 2017. An intermolecular FRET sensor detects

- the dynamics of T cell receptor clustering. *Nature Communications* 8:15100. <https://doi.org/10.1038/ncomms15100>.
178. Marquez-Jurado, S., J. Diaz-Colunga, R. P. das Neves, A. Martinez-Lorente, F. Almazan, R. Guantes, and F. J. Iborra, 2018. Mitochondrial levels determine variability in cell death by modulating apoptotic gene expression. *Nature Communications* 9:389. <https://doi.org/10.1038/s41467-017-02787-4>.
179. Necas, D., and P. Klapetek, 2012. Gwyddion: an open-source software for SPM data analysis. *Central European Journal of Physics* 10:181–188.

Danksagung

Meine Doktorarbeit ist fertig, und das habe ich den vielen lieben Menschen zu verdanken, die mich in diesen vier Jahren begleitet und mir Kraft gegeben haben. Insbesondere danke ich meiner Familie, meinen Mädels und vor allem Christoph - ohne euch wäre ich nicht da, wo ich jetzt bin!

Mein besonderer Dank gilt Prof. Joachim Rädler! Danke, Joachim, dass du es mir ermöglicht hast, meine Doktorarbeit an deinem Lehrstuhl durchzuführen! Danke, für deine Unterstützung, deinen Weitblick und deine Inspiration!

Vielen Dank auch den Professoren Cornelia Monzel und Tim Liedl sowie Amelie Heuer-Jungemann! Die Meetings mit euch waren für mich von unschätzbarem Wert und haben mir stets Hilfestellungen gegeben. Außerdem möchte ich mich für die zusätzliche Unterstützung von Prof. Ralf Jungmann, Prof. Camilo Aponte-Santamaria und Angelica Sandoval-Perez bedanken!

Die Graduiertenschule, Quantitative Biosciences Munich, hat mir durch das Stipendium meine Forschungsarbeit erst ermöglicht, vielen Dank dafür und auch für die internationalen Konferenzen, die ich besuchen durfte!

Schließlich möchte ich auch dem gesamten Lehrstuhl, insbesondere meinen Bürokollegen, und Freunden für das freundliche und hilfsbereite Klima danken:

Alex	Ellie	Max	Simon
Alexandra	Fabi	Margarete	Sonja
Amelie	Flo	Margith	Sophia
Anita	Gerlinde	Matthias	Susi
Bene	Grega	Mauricio	Tamara
Benni	Judith	Miri	Thomas
Charlott	Jürgen	Moritz	Valentin
Christoph	Kevin	Peter	Veri
Daniel	Lena	Philip	Victor
David	Linh	Sarafina	und vielen mehr ...

